University of Alberta

Age, Geochemistry, and Fluid Characteristics of the MAX Porphyry Mo Deposit, Southeast British Columbia

by

Christopher J.M. Lawley

A thesis submitted to the Faculty of Graduate Studies and Research
in partial fulfillment of the requirements for the degree of

Master of Science

The Department of Earth and Atmospheric Science

Fall, 2009
Edmonton, Alberta

Examining Committee

Dr. Jeremy P. Richards, Earth and Atmospheric Sciences

Dr. Robert A. Creaser, Earth and Atmospheric Sciences

Dr. Hooman Askari, Mining Engineering, Civil & Electrical Engineering

Abstract

MAX is a porphyry Mo deposit located near Trout Lake village in southeastern British Columbia. Mo mineralization is hosted by variably-altered calc-alkaline granodiorite dikes. Quartz veins have been subdivided into a paragenetic sequence based on vein style and crosscutting relationships. Post-magmatic Pb-Zn-Ag-bearing veins crosscut Mo-bearing veins. Similarities in fluid chemistry from both vein types suggest a genetic link between porphyry Mo mineralization and base-metal veins.

Three molybdenite samples were collected from early and late Mo-bearing veins for Re-Os dating to constrain the timing of Mo-mineralizing events within the paragenetic sequence. All three dates overlap within analytical error, and yield a weighted average age of 80.3 ± 0.2 Ma. These dates are in excellent agreement with two $^{206}Pb/^{238}U$ weighted-average ages of the Trout Lake stock at 80.2 ± 1.0 Ma and 80.9 ± 1.6 Ma, indicating that the magmatic and hydrothermal ore-forming events were coeval and cogenetic.

Acknowledgements

I would like to thank my supervisor Jeremy Richards for his support advice throughout the project. Jeremy`s thoughtful and comprehensive reviews greatly improved the manuscript. Bob Anderson and the Geological Survey of Canada, under the auspices of the TGI3 initiative, financed all of the geochronology. John Mirko and Scott Broughton, from Roca Mines Inc., were incredibly supportive and provided complete access to the mine site and a roof over my head for two field seasons. Other financial contributors include Geoscience BC and the Society of Economic Geologists.

Re-Os geochronology was completed at the University of Alberta under the direction of Rob Creaser. Guangcheng Chen supervised the U-Pb geochronology portion of the project and Larry Heaman provided his valuable insight. All of the staff at the University of Alberta were instrumental and incredibly helpful.

Cliff Taylor at the Unites States Geologic Survey provided geochemical data for porphyry deposits in Idaho and Montana. Other unpublished geochemical data was provided by Dave Sinclair at the Geological Survey of Canada.

My favorite aspect of the project was the great cast of characters that I got to meet along the way. Most notably: Jack Denny, Paul Ransom, Frank O' Grady, John Baker, Terry Macaulay, Nick Carter, Bob Thompson, Don Davidson, Mike Middleton, Dave Melling, and Brian Meyer. I sincerely thank those mentioned above and the entire Roca team for making my summers so memorable.

My fellow graduate students also contributed a great deal to the project. Most notably: Jamie Kraft, Hilary Corlett, Suzie Byron, and Bronwen Wallace. Lucy—thank you for our cornish pasty eating, dinosaur finding, rollercoaster riding, coffee drinking, and road-tripping adventures. And for the great lunches—you are the best sandwich maker.

Table of Contents

Figure List

Table List

Symbol List

Symbol	Description	Symbol	Description
$K_{57.5}$	wt.% of K_2O at 57.5% SiO_2	Po	Pyrrhotite
˚C	Degrees Celsius	ppb	Parts per billion
Ap	Aplite	ppm	Parts per million
BGd	Biotite granodiorite	P-T-X	Pressure-temperaure-composition
Bhorn	Biotite hornfels	Py	Pyrite
Biot	Biotite	Qtz	Quartz
BQtzD	Biotite quartz diorite	REE	Rare earth element
BTon	Biotite tonalite	s	Seconds
Chl	Chlorite	Spha	Sphalerite
cm	Centimeter	Te	Eutectic temperature
Cp	Chalcopyrite	$Th_{CO2\ L\text{-}V(L)}$	Homogenization temperature of liquid and vapour CO_2 to the liquid phase
cps	Counts per second	$Th_{total(L)}$	Total homogenization temperature to liquid phase
equiv.	Equivalent	Ti	Titanite
Fsd	Feldspar	$Tm_{(clath)}$	Clathrate melting temperature
Fig.	Figure	$Tm_{(CO2)}$	Melting temperature of CO_2
fO_2	Oxygen fugacity	$Tm_{(ice)}$	Melting temperature of water
Gal	Galena	Tron	Trondhjemite
HREE	Heavy rare earth element	UST	Unidirectional solidification texture
ICP-MS	Inductively coupled mass spectrometry	wt.%	Weight percent
INAA	Instrumental neutron activation analysis	X_{CO2}	CO_2 composition
IUGS	International Union of Geological Sciences	XRD	X-ray diffraction
kbars	Kilobars	yr.	Year
km	Kilometer	µm	Micrometer
LREE	Light rare earth element	σ	Standard deviation
m	Meter	ρ	Density
Ma	Million years ago		
MC-ICPMS	Multi-collector inductively coupled mass spectrometry		
Musc	Muscovite		
n	Number		
Plag	Plagioclase		

1.0 Introduction

The MAX porphyry Mo deposit is located on the north slope of Trout Mountain, 5 km west of Trout Lake village, southeastern British Columbia (Fig. 1). Molybdenum mineralization is genetically associated with the Late Cretaceous Trout Lake stock (80.2 ± 1.0 Ma) and a well developed quartz vein stockwork. Intrusive phases range in composition from granodiorite–tonalite–quartz diorite and have intruded phyllite, schist, and marble of the Lardeau Group at the northern end of the Kootenay Arc. Previous studies focused on mapping alteration assemblages (Boyle and Leitch, 1983), identifying structural controls on Mo mineralization (Linnen and Williams-Jones, 1987), and determining the chemical evolution of mineralized fluids (Linnen and Williams-Jones, 1990). The current study builds on previous work by placing these observations within a geochronologic framework.

Porphyry deposits are defined by the presence of: a source intrusion, a network of quartz veins, distinct zones of hydrothermal alteration, and significant quantities of economic minerals (Titley and Hicks, 1966). Production in the Copper Mountain District (British Columbia) began in 1920 and marked the beginning of porphyry deposit exploitation in Canada. Since that time, Canadian porphyry deposits have become increasingly important sources of Cu, Au, and Mo. As a result of their economic importance, a large volume of scientific literature has been produced that has identified many of the key processes responsible for porphyry deposit formation. Complex crosscutting relationships between the source intrusion, ore mineralization, and alteration assemblages have been well documented. While the qualititative relationship between igneous and hydrothermal activity has been recognized, the exact timing of these features remains poorly understood. This is due in large part to the challenges associated with obtaining high-precision geochronology.

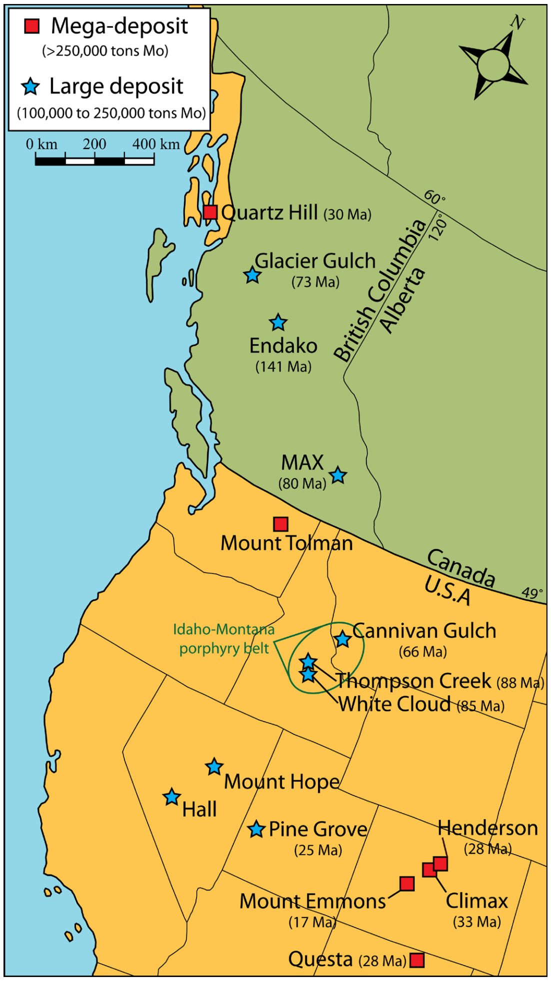

Figure 1. Map showing location of major porphyry Mo deposits in North America (modified from Westra and Keith, 1981). Cannivan Gulch, Thompson Creek, and White Cloud are deposits within the Idaho-Montana porphyry belt. Henderson, Mount Emmons, and Climax are some of the largest porphyry Mo deposits in the world and are located within the Colorado mineral belt. Approximate deposit ages are summarized from Soregaroli and Brown (1976), Hudson et al. (1979), White et al. (1981), Keith and Shanks (1988), Taylor et al. (2007), and Klemm et al. (2008).

Recent advances in geochronology are now allowing researchers to identify discrete mineralizing events that were previously unrecognized. Giant porphyry copper deposits in South America, such as El Teniente, Rio Blanco, and Escondida, are now known to possess magmatic–hydrothermal histories that span >1 million years (Richards et al., 1999; Maksaev et al., 2004; Padilla-Garza et al., 2004, Deckart et al., 2005). Similar time spans were also identified at large porphyry Mo deposits, such as Endako, British Columbia (Selby and Creaser, 2001). Suitable geochronometers must possess high closure temperatures to resist resetting during the multiple hydrothermal alteration episodes that are typical of these large deposits. The low closure temperature of the K–Ar system makes this geochronometer particularly vulnerable to resetting (Faure, 1986; McDougall and Harrison, 1988). Hedenquist and Richards (1998) proposed that smaller porphyry deposits, such as MAX, do not suffer from these overprinting effects and may be amenable to precise geochronologic study. The primary focus of the current study is to integrate U–Pb, Re–Os, and Ar–Ar geochronology in order to develop a temporal framework for the MAX deposit. U–Pb zircon dating is used constrain the time span of igneous activity; Ar–Ar dating of muscovite and biotite is used to determine the duration of hydrothermal activity; and Re–Os is used to directly date Mo mineralizing events. This framework is then used to aid interpretation of lithogeochemistry and fluid inclusion studies.

Many porphyry deposits are spatially and in some cases genetically related to epithermal, skarn, and Pb-Zn-Ag vein deposits (Ray et al., 1995; Hedenquist et al., 1998; Heinrich et al., 2004; Sidorov, 2006). Porphyry Mo districts such as the

Colorado Mineral Belt, Idaho–Montana Mineral Belt, and most British Columbia porphyry Mo deposits (Fig. 2) are spatially associated with late Pb-Zn-Ag veins (Soregaroli and Sutherland Brown, 1976; Seedorff, 1998; Worthington, 2007). These distal veins extend the hydrothermal footprint of porphyry deposits and are useful vectors towards porphyry mineralization. The MAX deposit is genetically related to W skarn lenses and spatially related to Pb-Zn-Ag-bearing veins. The second major focus of this current study is to test whether these peripheral base-

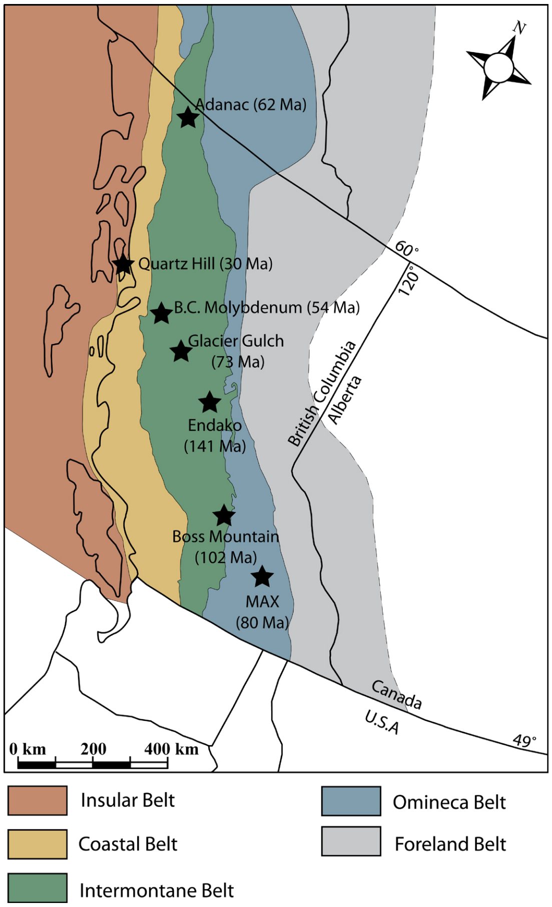

Figure 2. Map showing the location of MAX and other porphyry Mo deposits relative to British Columbia's major tectonic belts (modified from Wheeler and McFeely, 1991). Most porphyry Mo deposits in British Columbia are located in the Intermontane Belt. Deposit ages are summarized from Soregaroli and Brown (1976) and Hudson et al. (1979).

and precious-metal deposits are genetically related to MAX. Fluid chemistry from Mo- and Pb-Zn-Ag-bearing veins is evaluated and compared through petrography and fluid inclusion microthermometry.

Porphyry Mo deposits can be classified into two broad types: (1) high grade, rift related, fluorine-rich deposits associated with alkali-calcic intrusions, and (2) low grade, subduction related, fluorine-poor deposits associated with calc-alkaline intrusions (Carten et al., 1997). Scientific literature has traditionally focused on the first porphyry Mo deposit type as a result of their greater economic importance. The current study on the MAX will help fill the knowledge gap by developing a metallogenic model for the second porphyry Mo deposit type through integration of geochronology, lithogeochemistry, and fluid chemistry.

Significant differences between porphyry Cu (±Au) and porphyry Mo deposits warrants separate treatment of these two deposit types. Excellent research papers reviewing porphyry Mo deposits include: Soregaroli (1975), Soregaroli and Sutherland Brown (1976), Carter (1981), Westra and Keith (1981), White et al. (1981), Griffiths and Godwin (1983), Kirkham and Sinclair (1984), Steininger (1985), Stein (1988), Carten et al. (1988), Linnen and Williams-Jones (1990), Darling (1994), Wallace (1995), Seedorff et al. (2005), and Worthington (2007).

2.0 Age, Geochemistry, and Fluid Characteristics of the MAX Porphyry Mo Deposit, Southeast British Columbia

2.1 Historical Background

The following historical account of mineral exploration activities around Trout Lake is summarized from Brock (1904), Emmens (1914), Walker et al. (1929), Fyles and Eastwood (1962), and Parent (2001). Kootenay mineral exploration efforts occurred simultaneously with the construction of the trans-continental railway. Mining was initially limited to placer deposits but was soon followed by lode mining after establishment of the Bluebell mine in 1882. The completion of the railway and development of the Revelstoke smelter (1890) spurred mineral exploration in and around Trout Lake. Claims were staked as early as 1890, and included the now famous Silver Cup showing. Silver and gold were the minerals of economic interest, and Trout Lake village grew to become a major mining hub in the Kootenay area.

Successful mining operations at Silver Cup and the other Ag prospects on Silver Cup Ridge stimulated mineral exploration across the valley onto Trout Mountain. In 1897, the Lucky Boy Pb-Zn-Ag claim was staked. Mineralization at this deposit is hosted by quartz veins that crosscut marble, schist, and quartzite of the Lardeau Group. Mining at Lucky Boy began in the early 1900s and continued until 1917. Underground workings include a network of shafts and adits that extend 60 m below surface. Other Trout Mountain Ag producers at this time included Copper Chief and Horseshoe.

World War 2 increased the demand for base metals and revitalized the Kootenay mining industry. Tungsten, lead, and zinc became the principal minerals of economic interest. Abandoned operations, such as the Silver Cup and Lucky Boy mines, were re-opened. Lucky Boy became a tungsten producer with scheelite primarily hosted within pyrrhotite-garnet-clinopyroxene skarn and minor amounts hosted by quartz veins. After the war, mining operations became dormant and very little exploration activity occurred until the 1970s.

Molybdenite was first reported on Trout Mountain in 1917 but was not at that time considered a mineral of economic interest (Walker et al., 1929). Mineral claims, that now incorporate the MAX, changed ownership until the mid 1970s, at which point, Newmont Mining Corporation of Canada entered a joint venture with Esso Minerals Canada to gain control of the property. In 1977, the discovery hole indicated a sizeable molybdenum deposit at depth and prompted the development of an underground exploration program. The following year, a two kilometer adit was driven into the north side of Trout Mountain, which was supplemented by 22,000 m of underground diamond drilling and bulk sampling of underground workings. Exploration and development was halted at the Trout Lake property during the early 1980s due to the fall of molybdenum prices. In 2003, Roca Mines Incorporated acquired the Trout Lake property and renamed it the MAX deposit. The MAX contains 280,000 tonnes at 1.95% MoS_2 within a much larger and lower grade resource of 42,940,000 tonnes at 0.21% MoS_2 (Macauley, 2004). Production at the MAX began in the fall of 2007.

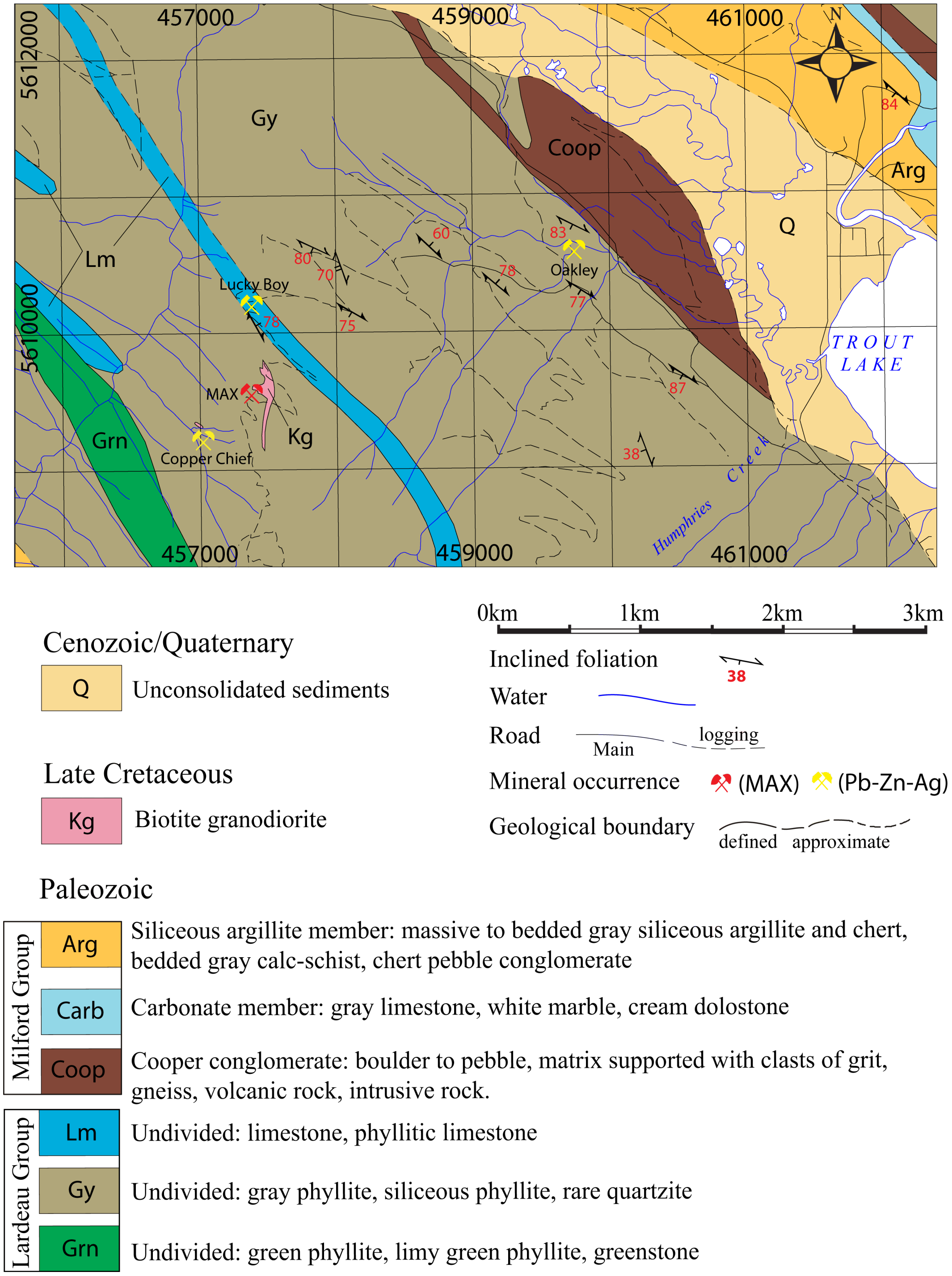

Figure 3. Local geology map west of Trout Lake (UTM grid NAD 27, zone 11). The Trout Lake stock has intruded phyllite-schist and marble of the Lardeau Group. Note the location of the MAX to nearby Pb-Zn-Ag deposits (modified from Read and Wheeler, 1975).

2.2 Regional Geology

MAX is situated at the northern end of the Kootenay Arc. This complicated structural belt has been studied by several authors (e.g., Archibald et al., 1983; 1984; Smith and Gehrels, 1992; Colpron and Price, 1995; Ghosh, 1995). Mo mineralization is hosted within the Trout Lake stock, which intruded phyllite, schist, and marble of the Paleozoic Lardeau Group (Fig. 3). From bottom to top, the Lardeau Group consists of the Index, Triune, Ajax, Sharon Creek, Jowett, and Broadview Formations. Each formation within the Lardeau Group is interpreted to be conformable and represents an upright stratigraphic sequence (Fyles and Eastwood, 1962). The Lardeau Group overlies the Early Cambrian Badshot Formation and is unconformably overlain by the Late Mississippian Milford Group (Read and Wheeler, 1975). These two bounding units constrain the age of the Lardeau Group to between post-Early Cambrian and pre-Late Mississippian. Broadview Formation schist, phyllite, and marble comprise the country rock surrounding the Trout Lake stock (Read and Wheeler, 1975). Paleozoic metamorphism is almost entirely overprinted by Jurassic deformation that has produced the dominant northwest fabric of the metasedimentary rocks. Further south, in the central Kootenay Arc, K–Ar dates have been reset by a Paleocene metamorphic event (Matthews, 1983). This late metamorphic event has not been recognized at Trout Lake.

Psutka et al. (1982) delineated several northwest- and north-trending faults that truncate the MAX deposit. The Z fault bounds the deposit on the eastern side and is of most significance because it appears to post-date and offset

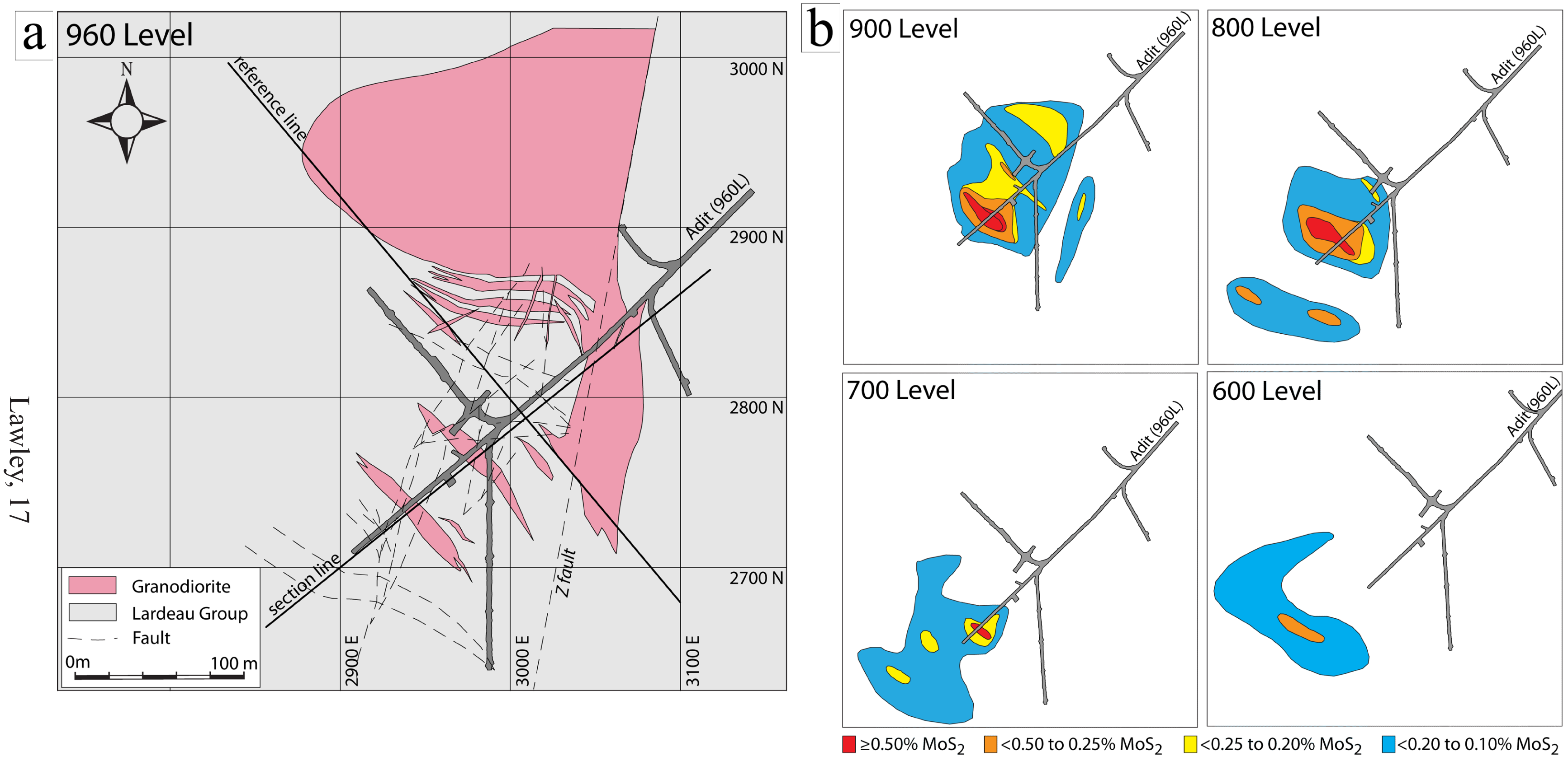

Figure 4. (a) Geology plan at adit level with mine grid. Section and reference lines correspond to Fig. 13; (b) Mo contoured at different levels in order to depict Mo distribution with depth. Note, adit is projected for levels other than 960L (modified from Boyle and Parliament, 1983).

mineralization. This fault is interpreted to be a normal, east-side down, sub-vertical fault with displacement on the order of 100s of meters based on diamond drilling intersections at depth. Map patterns at adit level suggest the Z fault may also have been active as a right-lateral strike-slip fault (Fig. 4). The Ethel fault bounds the deposit on the western side and is also interpreted to be a normal fault. Displacement estimates are uncertain because of the lack of a distinct marker horizon within the Broadview Formation. The Trout Lake stock itself is interpreted to be post-kinematic based on the lack of metamorphic textures within the stock and the undeformed shape of its thermal aureole.

The Trout Lake stock is one of a series of Jurassic to Cretaceous calc-alkaline intrusions within southeastern British Columbia (Fig. 5). Approximately 5 km south of the MAX deposit is the Jurassic (178 ± 5 Ma) quartz-monzonitic Kuskanax batholith (Parrish and Wheeler, 1983). A slightly younger Jurassic stock (161.6 ± 0.5 Ma) intruded the northern margin of the Kuskanax Batholith and marks the end of deformation within the Kootenay Arc (Parrish and Armstrong, 1987). Approximately 35 km north of Trout Lake is the Middle Cretaceous Battle Range batholith and a southeast-trending belt of similar aged batholiths that include the Bugaboo and Horsethief Creek (Brandon and Lambert, 1993). These intrusive bodies are also associated with molybdenite mineralization although there are currently no other molybdenum producers in the area.

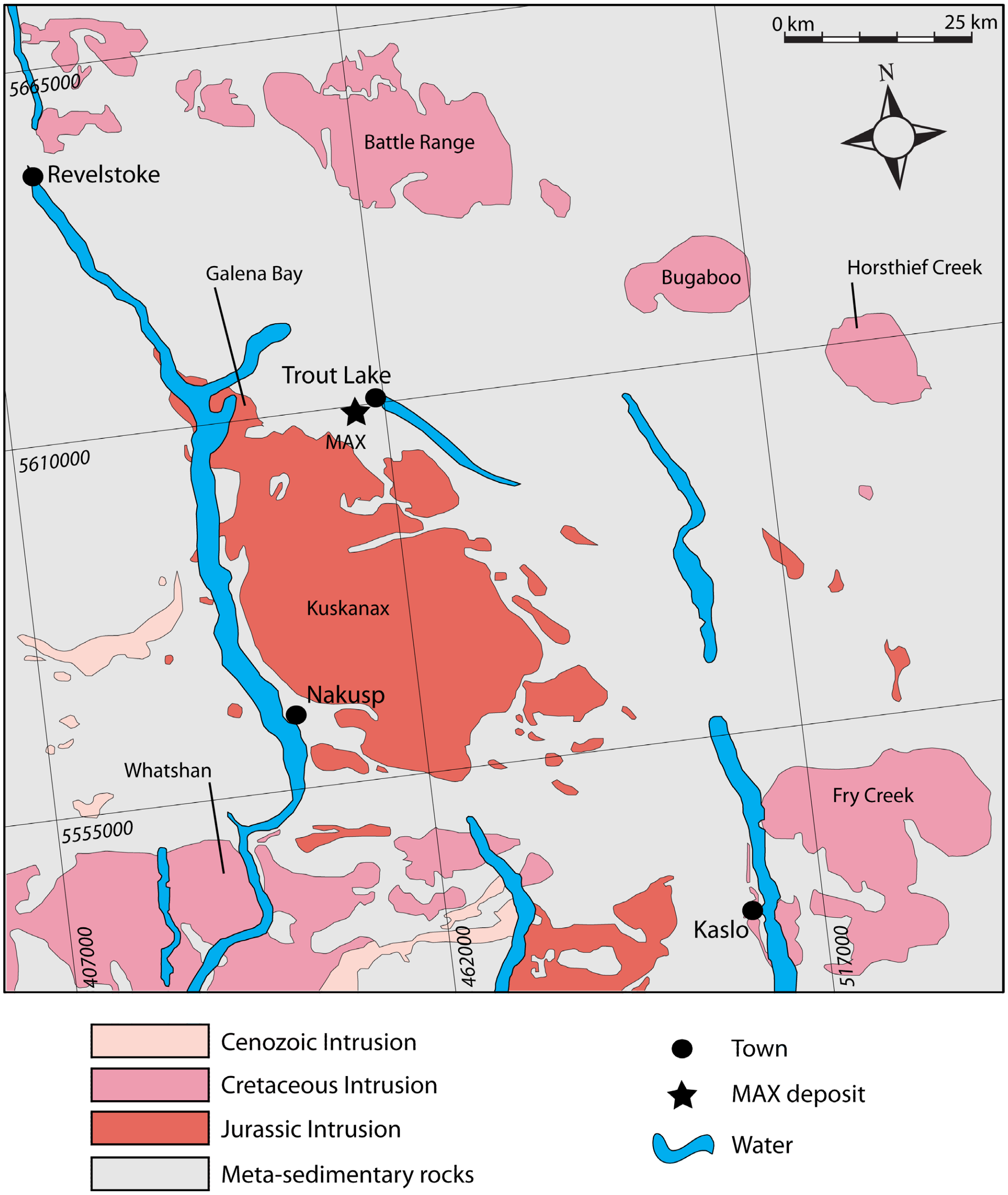

Figure 5. Regional geologic setting of the MAX deposit (UTM grid NAD 27, Zone 11; modified from Massey et al., 2005).

2.3 Geology of the MAX Porphyry Mo Deposit

2.3.1 Intrusive Phases

The MAX deposit possesses at least five distinct intrusive phases (Fig. 6). Igneous textures, mineralogy, and appearance are variable due, in part, to overprinting hydrothermal alteration. Additional intrusive phases may be identified with future mine development and exploration drilling. All intrusive phases have been classified according to the International Union of Geological Sciences scheme (Le Maitre, 2002). Modal mineralogy was estimated during petrography that is summarized in Appendix E.

Biotite granodiorite is the most abundant phase and is host to the majority of molybdenite mineralization. Mineralized quartz veins both crosscut and are crosscut by granodiorite dikes. Igneous textures vary from porphyritic to equigranular and massive to foliated. Quartz phenocrysts are common and range in size from 2 to 5 mm. Concentrically zoned plagioclase phenocrysts are observed locally (Fig. 7a). Dikes vary in color from white and black to light gray. Primary igneous minerals in typical order of abundance include plagioclase, quartz, K feldspar, and biotite. Secondary minerals include chlorite, muscovite, biotite, titanite, epidote, rutile, calcite, pyrite, and molybdenite. Biotite granodiorite dikes possess the most textural and mineralogical variability compared to the other intrusive phases. Dikes can be traced over 2 km of vertical extent and tend to coalesce at depth.

Narrow biotite tonalite dikes are the second most abundant phase at MAX.

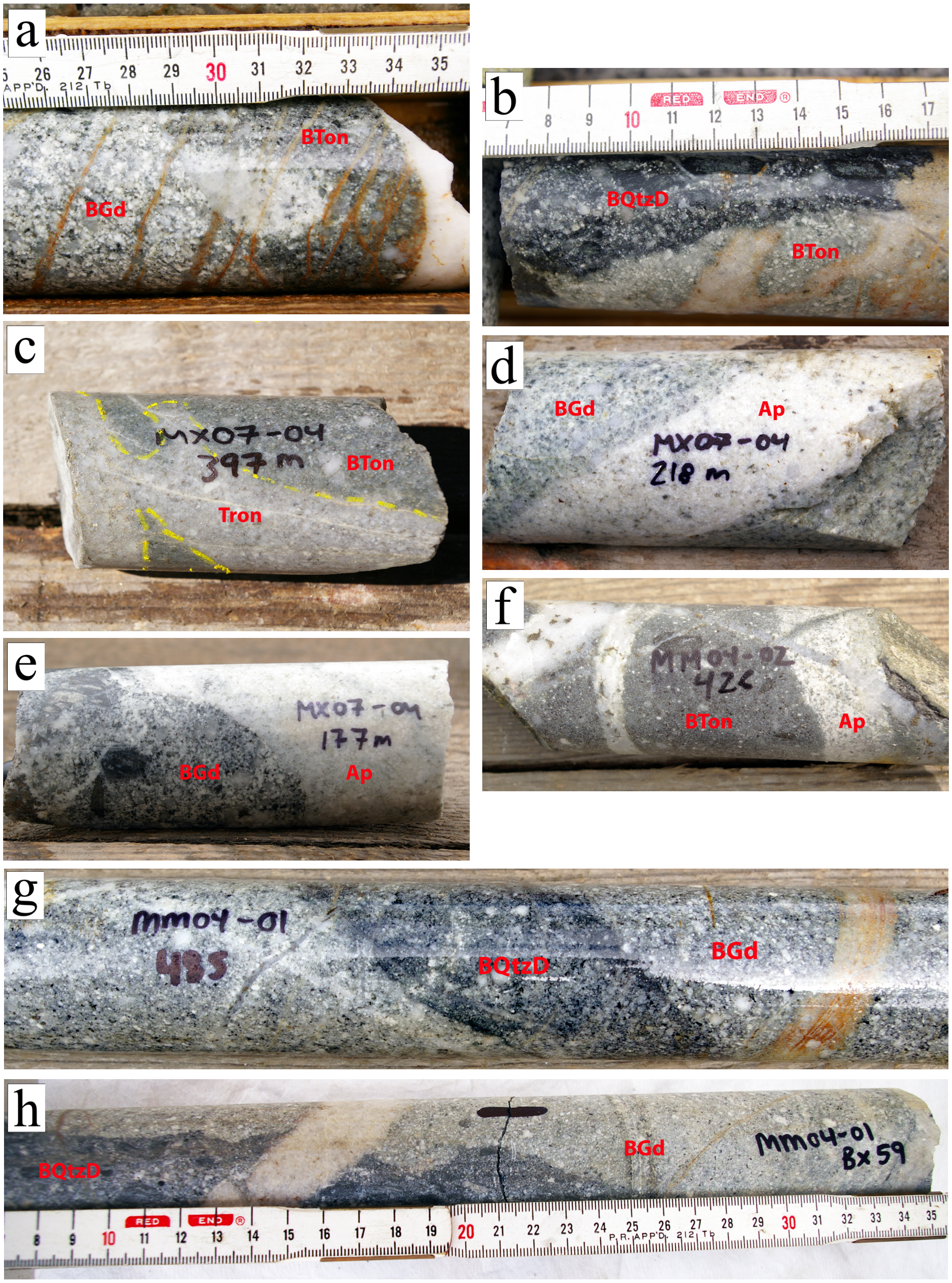

Figure 6. (a) Biotite granodiorite (BGd)–biotite tonalite (BTon) contact; (b) biotite quartz diorite (BQtzD)–biotite tonalite contact; (c) biotite tonalite–trondhjemite (Tron) contact; (d) aplite (Ap) dike crosscutting biotite granodiorite; (e) aplite dike crosscutting biotite granodiorite; (f) aplite dike crosscutting biotite tonalite; (g) biotite quartz diorite dike crosscutting biotite granodiorite; (h) biotite granodiorite–biottie quartz diorite contact

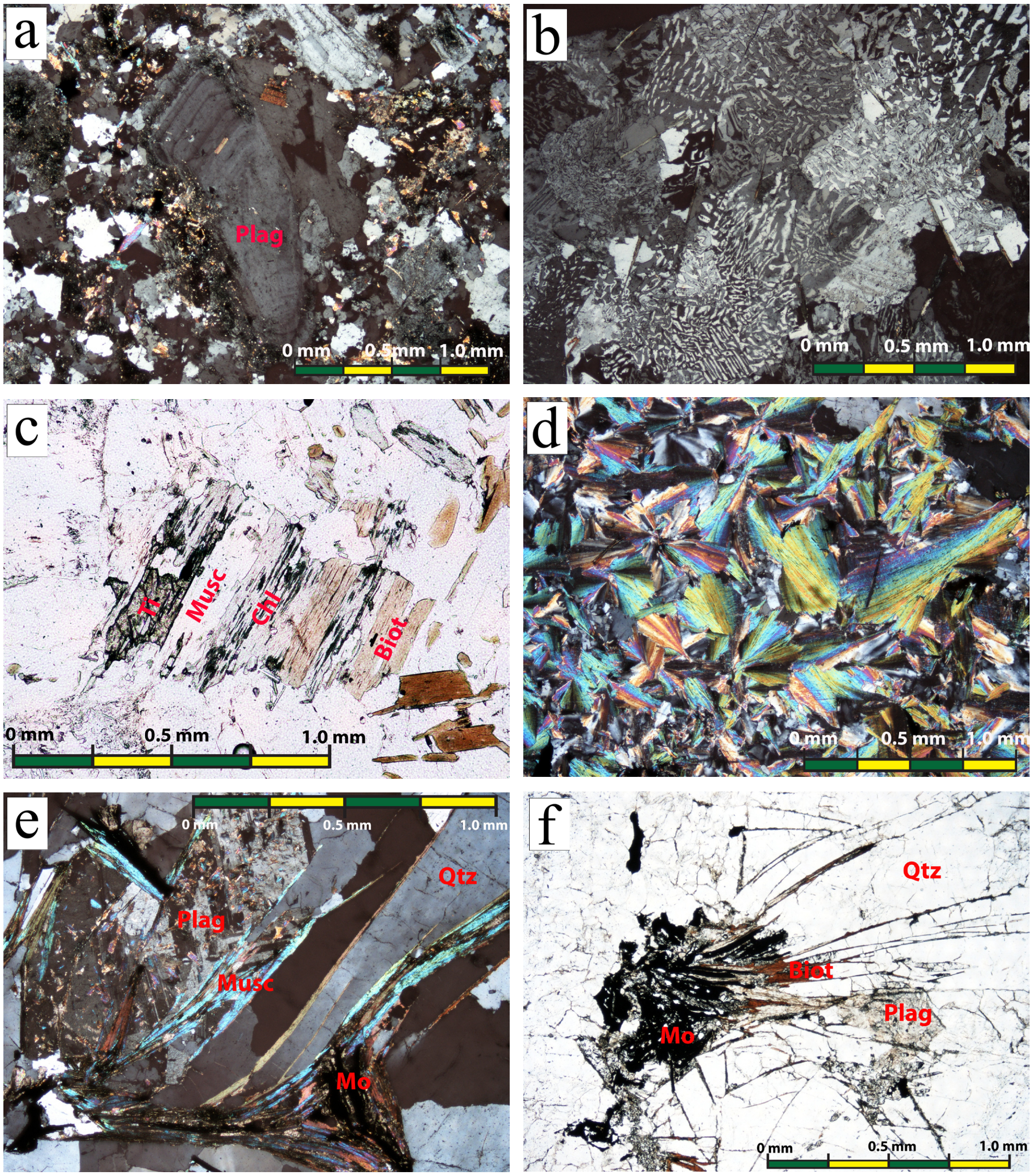

Figure 7. Transmitted light photomicrographs of: (a) concentrically-zoned and twinned plagioclase (Plag). Note the minor sericite alteration at the margin and peripheral to plagioclase phenocryst (crossed polars); (b) micrographic texture in aplite dike (crossed polars); (c) titanite (Ti)-muscovite (Musc)-chlorite (Chl) pseudomorphing biotite (Biot); (d) coarse muscovite replacement of plagioclase within intensely phyllic altered dike (crossed polars); (e) muscovite–molybdenite (Mo) intergrowths. Plagioclase is slightly replaced by sericite and quartz (Qtz) is interstial (crossed polars); (f) Molybdenite–biotite intergrowths; plagioclase and quartz are interstial.

Biotite tonalite dikes are porphyritic, dark-gray, massive, and typically crosscut granodiorite. Quartz phenocrysts are similar in appearance to those within granodiorite and typically range in size from 2 to 5 mm. Mineralized quartz veins both crosscut and are crosscut by biotite tonalite dikes. The decreased abundance of K feldspar and striking dark-gray color warrants the biotite tonalite dikes being classified as a separate phase. Primary igneous minerals in typical order of abundance include plagioclase, quartz, biotite, and K feldspar. Secondary minerals include chlorite, titanite, and epidote.

Aplite dikes are another abundant intrusive phase at MAX. These dikes are typically narrow (<1 m), fine grained, equigranular, and massive. Disseminated molybdenite rosettes are locally observed, and rare pyrite is present in more altered examples. Graphic and micrographic textures are a ubiquitous igneous texture in this phase (Fig. 7b). Many underground exposures of aplite are gradational between igneous dikes and quartz + feldspar veins. A continuum between hydrothermal and igneous phases has been observed at other porphyry Mo deposits (White et al., 1981; Seedorff, 1988). Primary igneous minerals in typical order of abundance include quartz, K feldspar, plagioclase, muscovite, garnet. The lack of biotite, finer grained appearance, cream color, and increased abundance of K feldspar distinguish this phase from the others.

Recent drilling has intersected two additional intrusive phases that have an extremely restricted distribution. Five narrow biotite quartz diorite dikes have been intersected that are visually distinct. White plagioclase phenocrysts are scattered within a black biotite-rich groundmass. Primary igneous minerals in order of abundance include biotite (~30%), plagioclase, quartz, and K feldspar. Secondary minerals include chlorite, muscovite, biotite, epidote, titanite, calcite, and pyrite. Biotite quartz diorite dikes have been observed crosscutting biotite tonalite and biotite granodiorite dikes, and are in turn crosscut by mineralized quartz veins.

Trondhjemite dikes are the fifth and least abundant intrusive phase at MAX. Le Maitre et al. (2002) suggests using the term "trondhjemite" for rocks with tonalite modal compositions that contain an insignificant mafic component (i.e., <10% mafic minerals). White plagioclase phenocrysts, the absence of biotite, and light gray color distinguish this phase from the more abundant biotite tonalite dikes. Major (e.g., enriched in Na_2O) and trace element geochemistry of this intrusive phases also distinguishes it from other MAX phases (see below). Primary igneous minerals in order of average abundance include plagioclase, quartz, and K feldspar. Trondhjemite dikes have been observed crosscutting biotite tonalite dikes and are in turn crosscut by mineralized quartz veins. Future drilling and underground development may expose additional examples of these restricted phases and may allow better assessment of their significance. An example of the complex temporal relationships between dikes and veins is represented by a schematic sketch of an underground face on 920L (Fig. 8).

Excellent exposure in underground workings provides a window into magmatic process (Figs. 9–10). Most intrusive–country rock contacts exhibit evidence of both injection and permeation (Fig. 8). Angular fragments of biotite hornfels and altered hornfels have been observed within all intrusive phases.

These xenoliths indicate that hydrothermal alteration locally took place before emplacement of dikes. Angular fragments and resorbed mineralized quartz vein xenoliths have also been observed entrained within granodiorite dikes. Biotite granodiorite dikes locally become increasingly biotite rich towards dike–country rock contacts. These gradational contacts indicate that assimilation of the country rock took place, and are commonly referred to as permeation textures (Winter, 2001). Enclaves provide further evidence of mixing and assimilation. Sheared fragments of biotite hornfels and schlieren are commonly observed in all intrusive

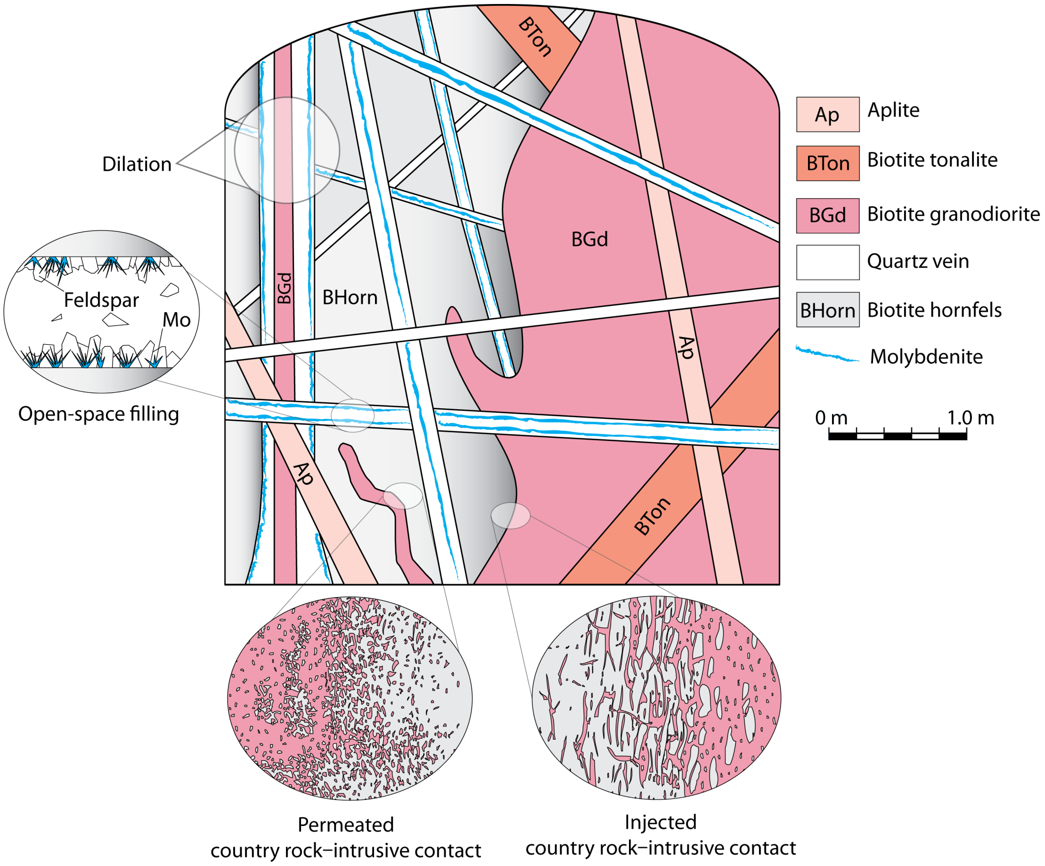

Figure 8. Schematic drawing of underground ore face at 920L. Note complex crosscutting relationships between dikes and quartz veins. Intrusive–country contacts range in texture from injected to permeated. Molybdenite and feldspar crystals grow inward from quartz vein margins.

phases. Biotite tonalite enclaves have also been observed within aplite and granodiorite dikes. Magmatic textures and complex crosscutting relationships provide evidence that hydrothermal alteration, Mo mineralization, and magmatic activity are closely related in time and space (Figs. 11 and 12).

2.3.2 Alteration

Linnen and Williams-Jones (1990) completed a comprehensive study on MAX alteration assemblages that broadly correspond to the model developed by Lowell and Guilbert (1970). Alteration assemblages identified by this author generally coincide with those of Linnen and Williams-Jones (1990) and are

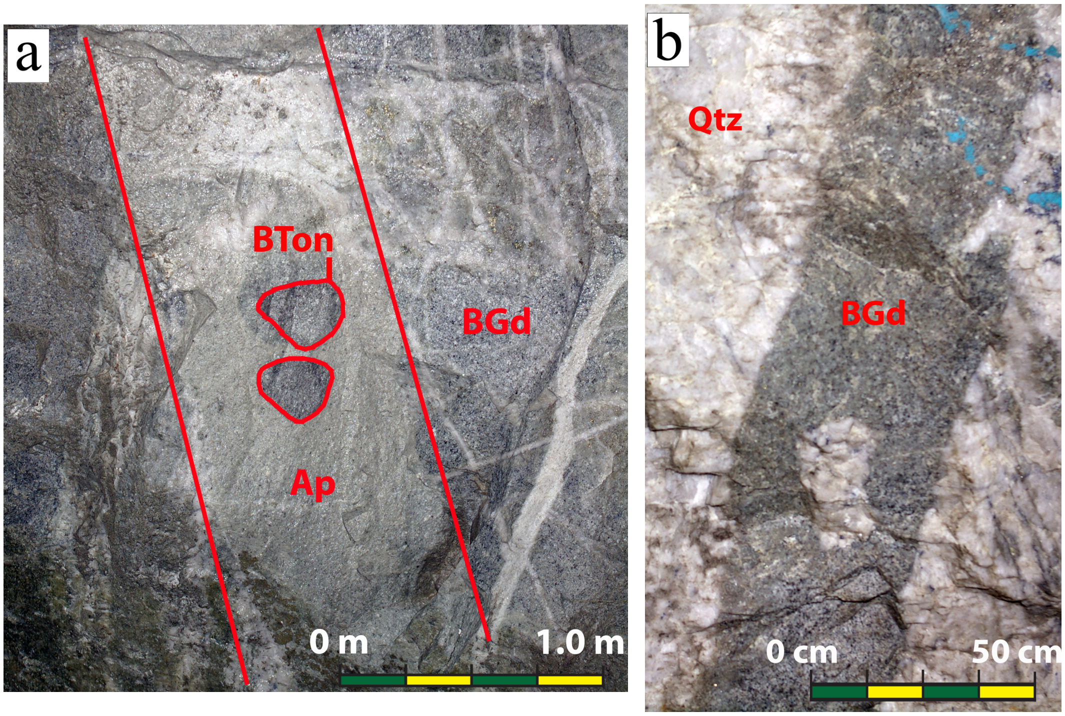

Figure 9. (a) Aplite dike crosscutting biotite granodiorite (BGd) in underground exposure at 960L. Round enclaves of biotite tonalite (BTon) are enclosed within aplite dike (Ap); (b) biotite granodiorite dike crosscutting thick Mo-bearing quartz (Qtz) vein with subangular Mo-bearing quartz vein xenolith.

based on petrography and observations made in underground workings. Quartz, molybdenite, K feldspar/plagioclase, and muscovite have been contoured to summarize the distribution of alteration assemblages in Figure 13 (Boyle and Leitch, 1983).

An elliptical zone of strongly-developed biotite hornfels is localized around the Trout Lake stock. Biotite hornfels is more massive, coarser grained, and more biotite-rich than surrounding Lardeau Group phyllite and schist (Fig.

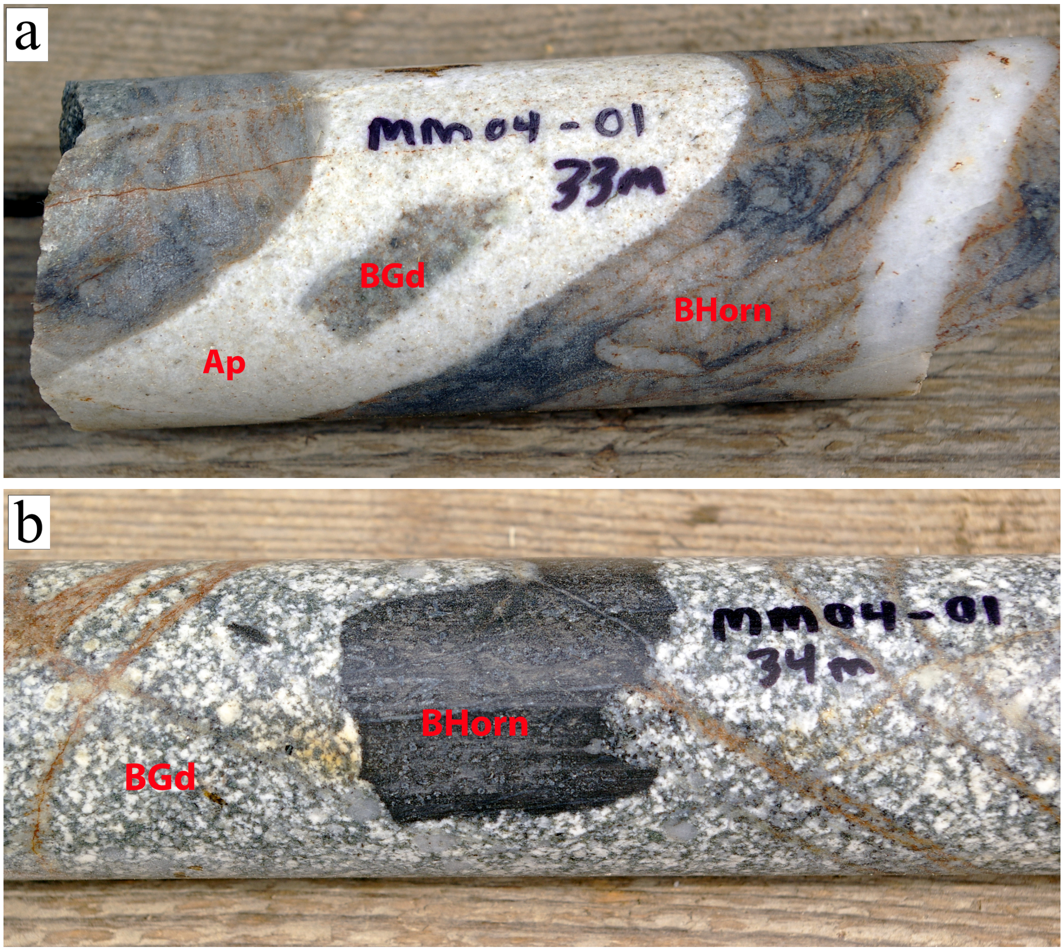

Figure 10. (a) Sub-angluar biotite granodiorite xenolith (BGd) within aplite dike (Ap) crosscutting phyllic-altered biotite hornfels (BHorn); (c) angular biotite hornfels xenolith within veined biotite granodiorite dike.

14). At the adit level, the limit of biotite hornfels roughly corresponds with the Z fault. Secondary minerals associated with the hornfels include biotite, quartz, muscovite, and rare andalusite. Biotite hornfels overprints regional metamorphism and is overprinted by potassic, phyllic, and propylitic alteration associated with the MAX hydrothermal system.

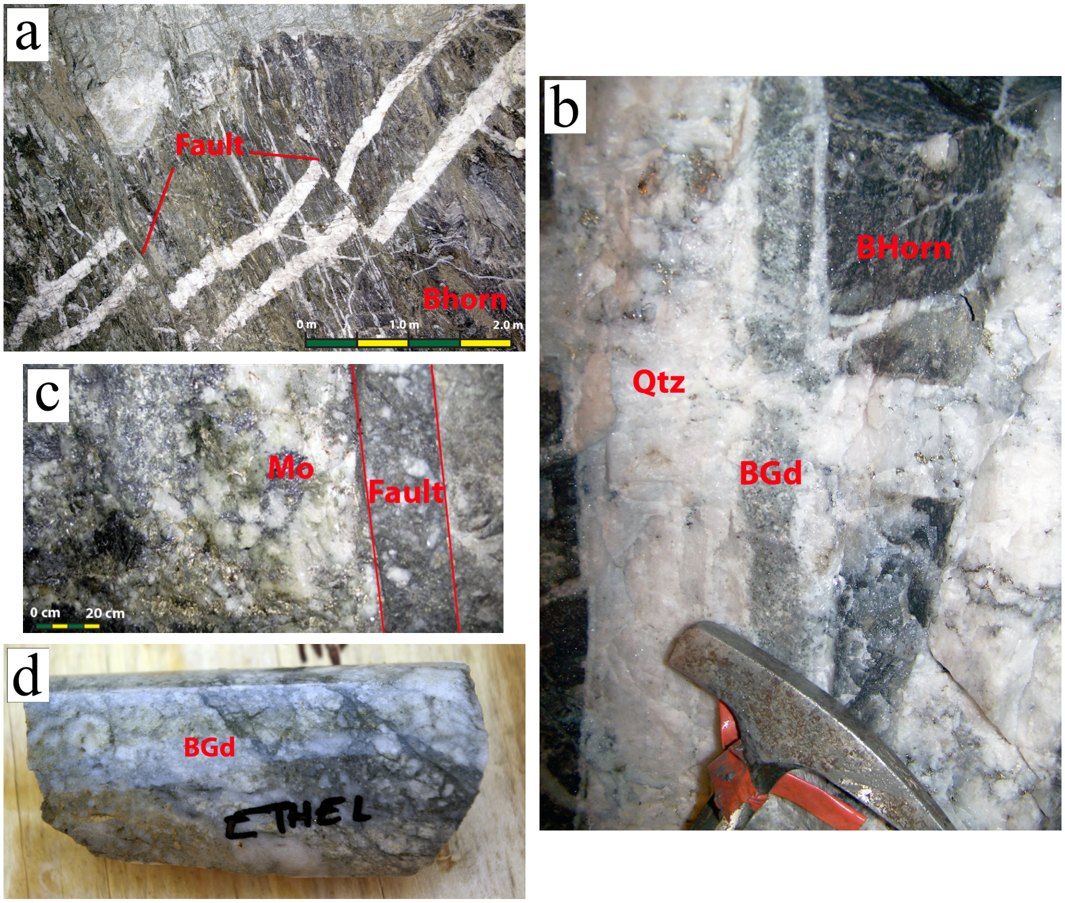

Figure 11. (a) Normal faults, interpreted to be splays off the Z-fault, displace Mo-bearing quartz veins in biotite hornfels (BHorn). Post-mineral faults are commonly observed throughout the deposit; (b) a close temporal relationship between between magmatic and hydrothermal activity is inferred from the complex crosscutting relationships between biotite granodiorite dikes (BGd) and quartz veins (Qtz). (c) pseudotachylite separates silicified country rock from Mo-bearing quartz vein; (d) Ethel fault bounds the deposit on the west side and contains silicified fragments of the Trout Lake stock within pseudotachylite. Intermineral faults, such as the Ethel and Z fault, may have been important localization mechanisms for the emplacement of the Trout Lake stock

Potassic alteration is characterized by biotite + K feldspar flooding and is most strongly developed within the high-grade zone (Fig. 14). Silicic alteration, characterized by quartz flooding and increased quartz vein density, is also most strongly developed within the high-grade zone. Quartz flooding is commonly observed crosscutting potassic altered rocks; however, narrow potassically altered dikes can also be observed crosscutting intense silicic alteration. The intimate relationship between silicic and potassic alteration with Mo mineralization suggests that all three events were coeval. Potassic alteration continues to depth,

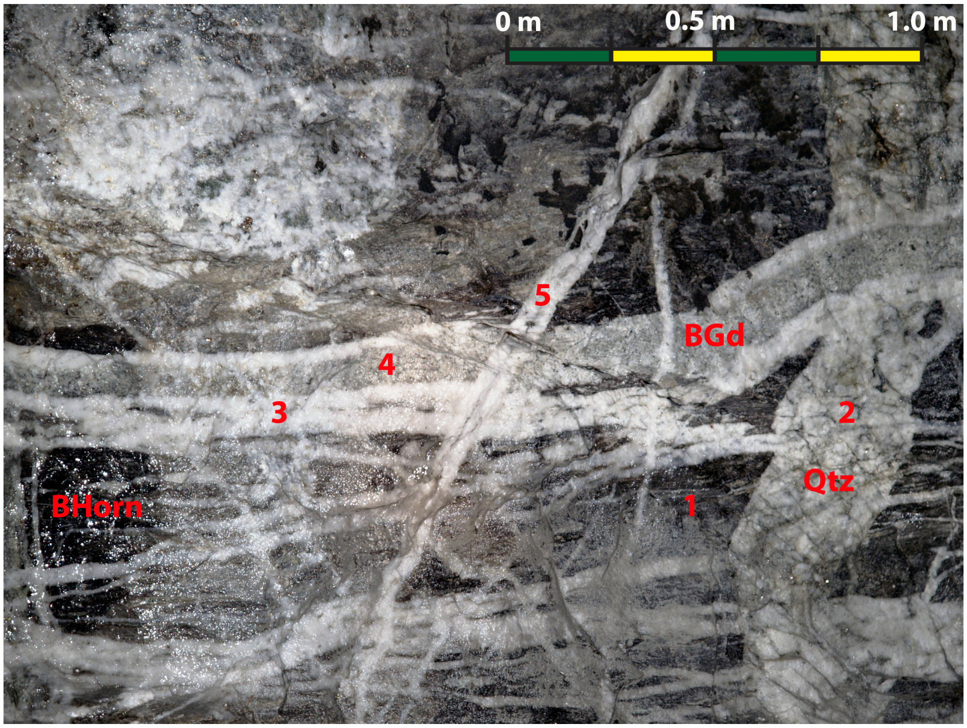

Figure 12. Underground expsoure at 960L providing an example of the complex crosscutting relationships between biotite granodiorite (BGd) dikes and quartz (Qtz) veins within biotite hornfels (BHorn). Early quartz sweats (1) within the Lardeau Group are always barren and are likely related to Jurassic deformation. Variably-oriented Mo-bearing quartz veins (2 and 3) form a complex stockwork. A biotite granodiorite dike (4) intrudes into the medial portion of a Mo-bearing quartz vein (3) and is subsequently crosscut by a Mo-bearing quartz vein (5).

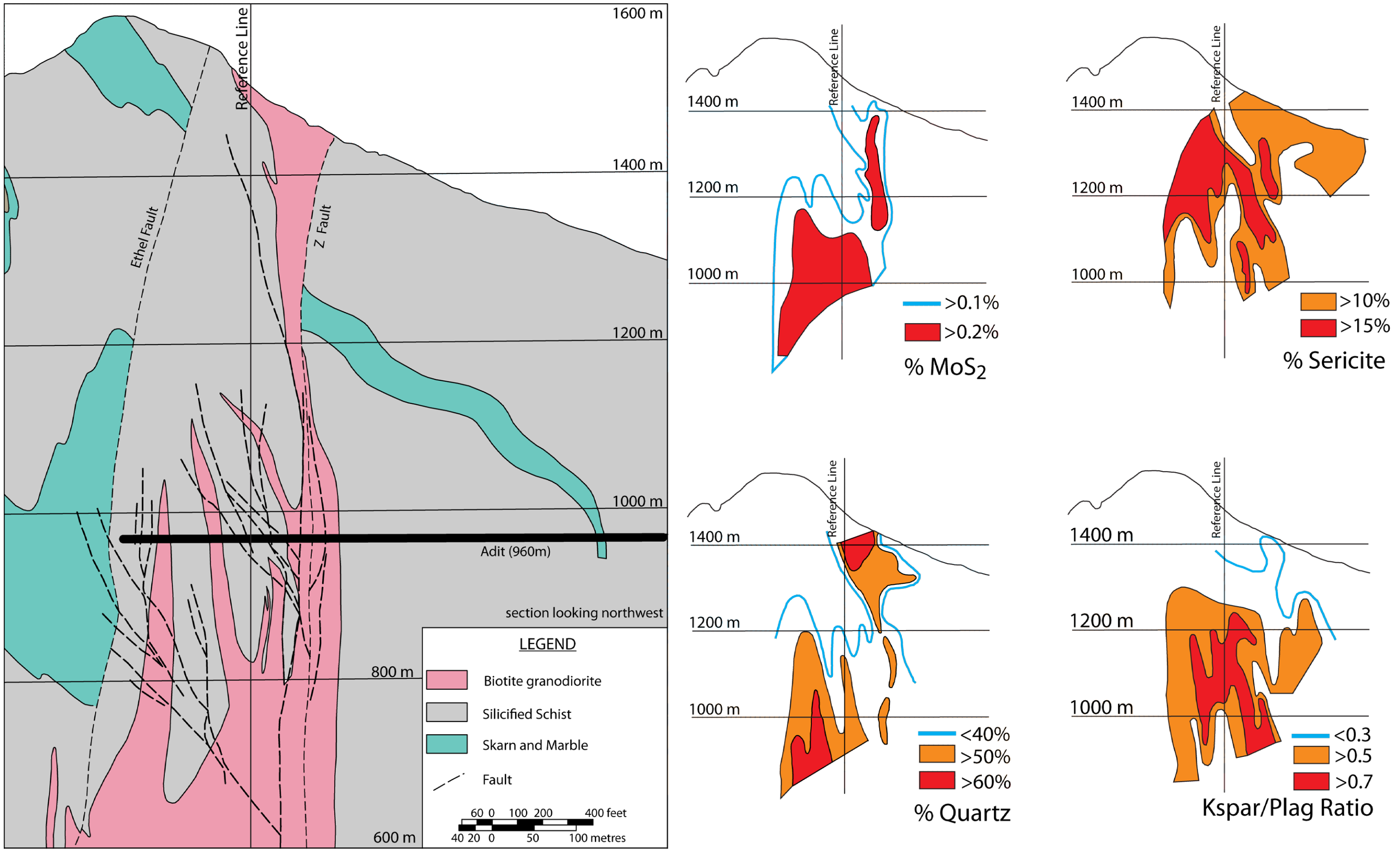

Figure 13. Geologic cross section of MAX with smaller cross sections showing generalized XRD alteration patterns (modified from Boyle and Leitch, 1983). See Fig. 4 for section and reference line location in plan.

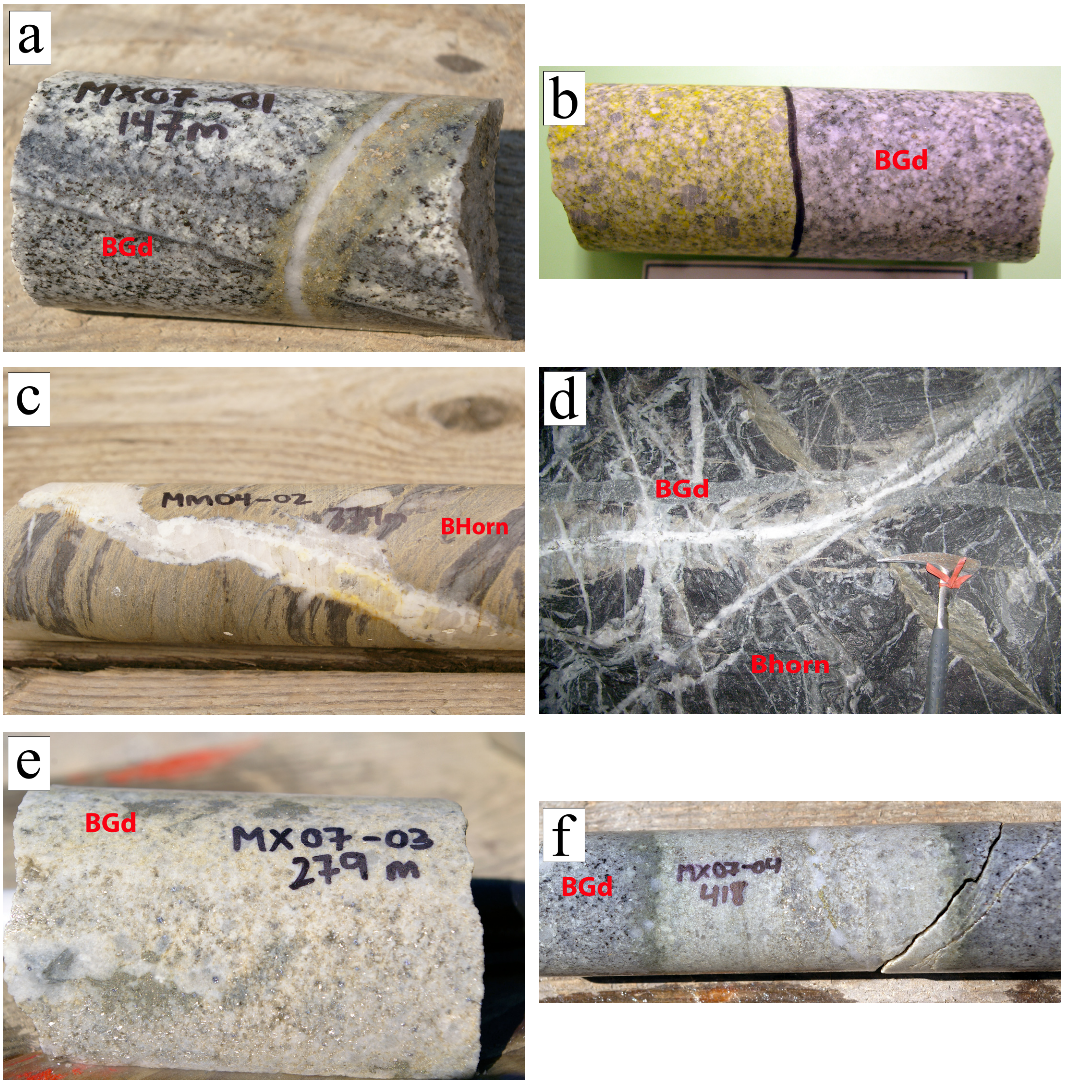

Figure 14. (a) Potassic-altered biotite granodiorite (BGd) dike (biotitized) overprinted by late propylitic alteration associated with quartz vein; (b) biotite granodiorite from high grade-zone stained with sodium cobaltnitrite to show extent of K feldspar flooding (yellow); (c) phyllic alteration halo around quartz vein overprinting biotite hornfels (BHorn); (d) biotite hornfels crosscut by mineralized stockwork and locally overprinted by phyllic alteration; (e) phyllic altered biotite granodiorite; (f) zoned alteration halo around quartz vein. Coarse muscovite-pyrite-calcite alteration grades into chlorite-dominated alteration.

whereas silicic alteration is limited to the apex of the high-grade dike.

Phyllic alteration, characterized by muscovite ± pyrite ± calcite, is widely distributed and locally pervasive (Fig. 14). Muscovite–molybdenite intergrowths are a common feature in zones of pervasive phyllic alteration. Areas peripheral to the high-grade zone have typically undergone intense and pervasive phyllic alteration. Petrographic examination reveals that coarse-grained muscovite replacement of biotite is accompanied by fine-grained muscovite replacement of feldspars (Fig. 7). Phyllic alteration halos around mineralized quartz veins overprint potassic and silicic alteration assemblages.

Late propylitic alteration is widely distributed and is characterized by chlorite ± epidote ± muscovite ± calcite ± titanite ± pyrite. Biotite in all samples has undergone partial replacement by chlorite-epidote-muscovite-titanite. Intense propylitic alteration is rare, and is exclusively localized along Pb-Zn-Ag-bearing quartz vein margins. Secondary biotite within the biotite hornfels is overprinted by late propylitic alteration (e.g., chlorite). The presence of regional metamorphic chlorite makes it difficult to determine the extent of propylitic alteration overprinting schist and phyllite away from MAX.

Clinopyroxene ± garnet ± pyrrhotite ± calcite ± wollastonite ± scheelite skarn is strongly developed along fault zones extending towards the Trout Lake stock and along granodiorite–marble contacts. A continuum of replacement intensity is evident from slightly altered phyllite and schists to completely-replaced massive skarn (Figs. 15 and 16). Foliated skarn typically contains less high-temperature minerals, lower WO_3 grades, and retains the

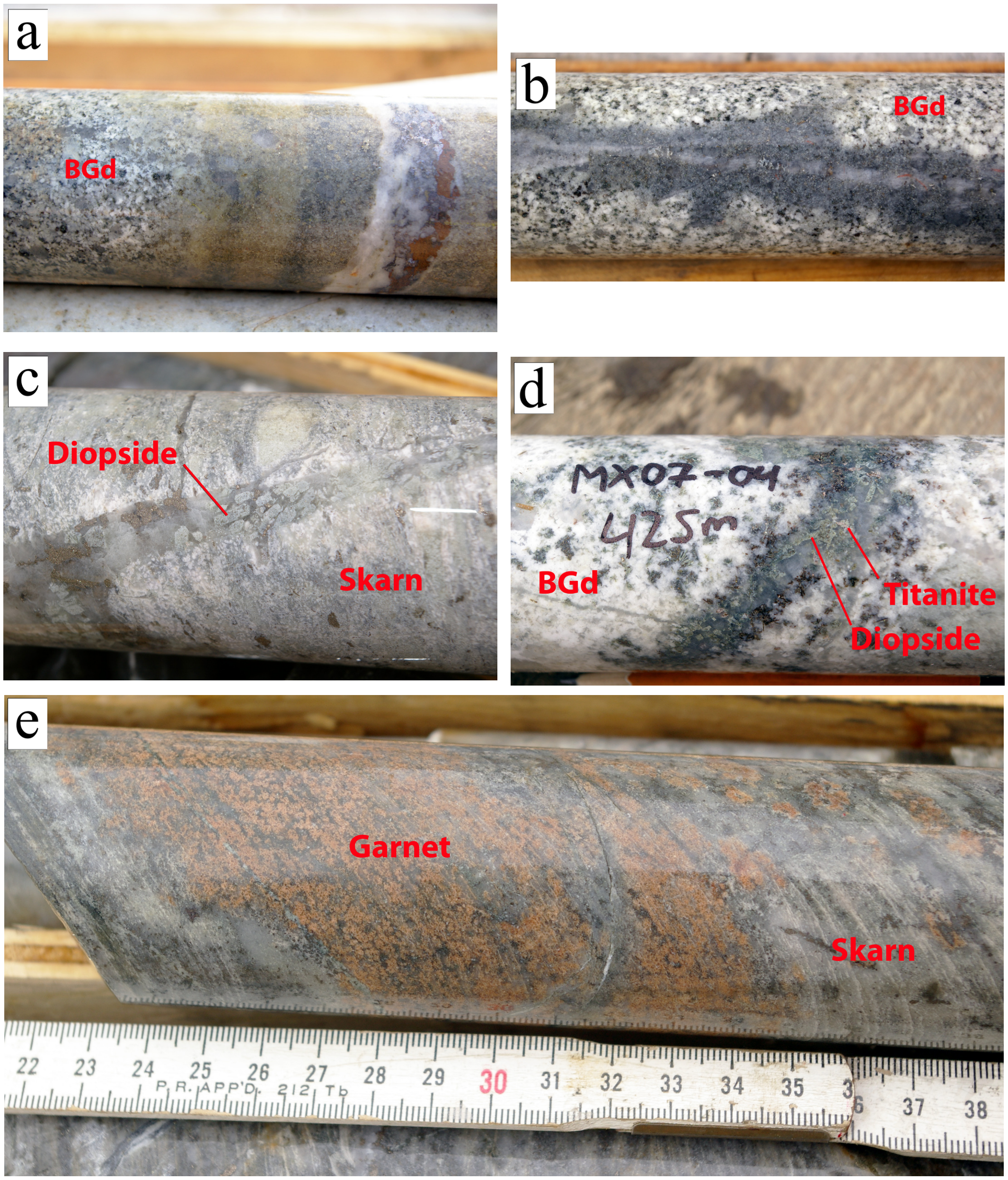

Figure 15. (a) Propylitic alteration associated with Pb-Zn-Ag-bearing quartz vein overprinting biotite granodiorite (BGd); (b) propylitic alteration halo around quartz vein overprinting biotite granodiorite; (c) coarse diopside and pyrrhotite aggregates within quartz vein crosscutting skarn; (d) locally developed endo-skarn near granodiorite–skarn contact. Note diopside (dark green) and titanite (pink) within quartz vein that crosscuts biotite granodiorite; (e) foliated skarn becomes completely replaced by garnet.

regional metamorphic fabric. Massive skarn is associated with higher WO_3 grades, abundant high-temperature minerals, and is semi-continuous down-dip towards the Trout Lake stock. Garnet and clinopyroxene are locally observed in granodiorite near granodiorite–skarn contacts. This skarn mineralogy is interpreted to be locally developed endo-skarn (Fig. 15).

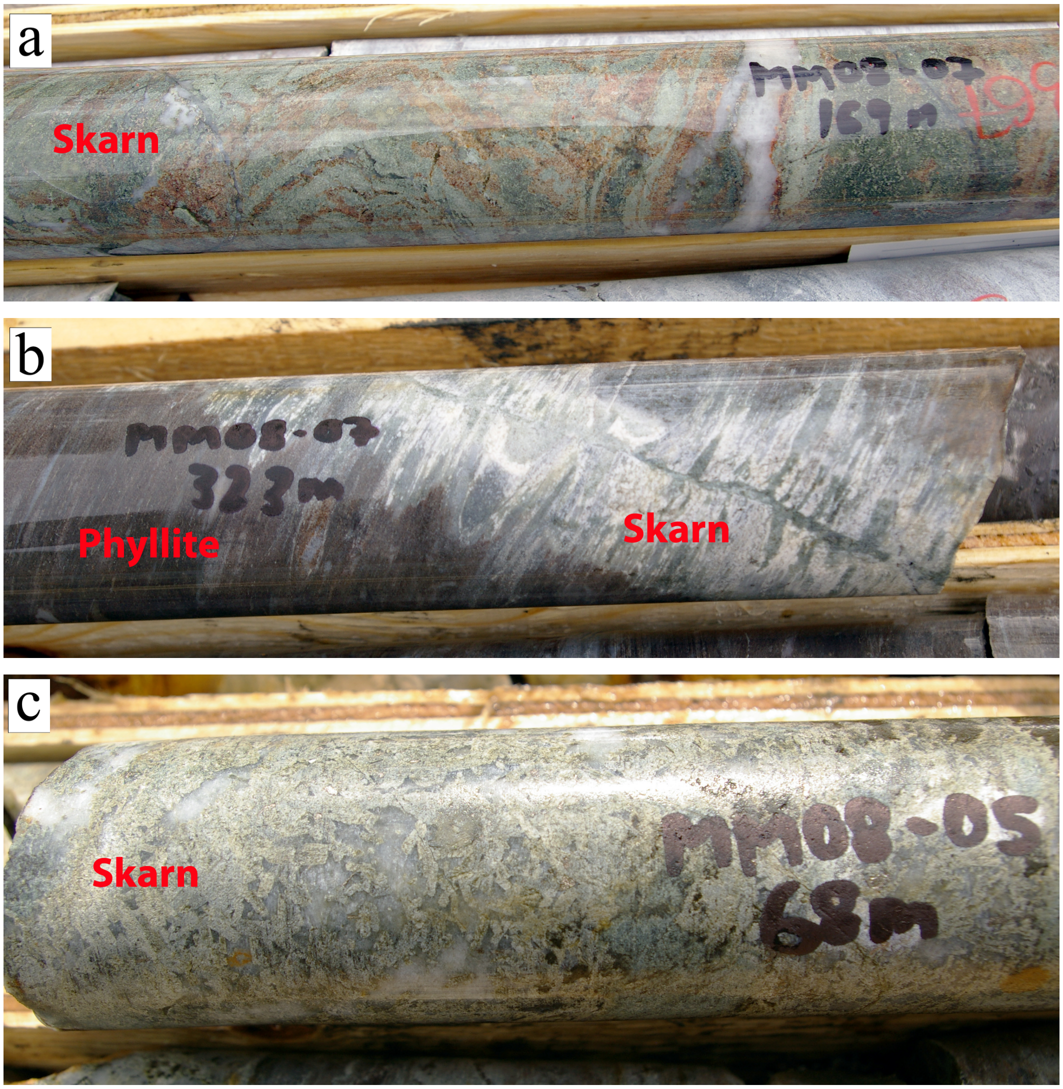

Figure 16. (a) Garnet-diopside-scheelite skarn. Note how skarn pseudormorphs previously deformed foliation; (b) biotite phyllite being replaced by diopside-epidote skarn around quartz vein; (c) coarse diopside replacing biotite phyllite protolith. Skarn becomes massive where more strongly developed.

2.3.3 Mo Mineralization

Molybdenite is the only mineral of economic interest at the MAX deposit, and is largely hosted within a well developed quartz vein stockwork and several granodiorite dikes (Fig. 17). Fine- to coarse-grained disseminations and rosettes of molybdenite deposited along quartz ± feldspar vein margins are the most common ore textures. Molybdenite is locally observed as radiating fans growing away from quartz vein margins. A high-grade zone is intimately associated with one of several lenticular granodiorite apophyses extending from the much larger biotite granodiorite body at depth. Molybdenite mineralization in this zone is present as coarse-grained disseminations within granodiorite, molybdenite–pyrrhotite intergrowths, and irregular stringers that are oriented parallel to the strike of the dikes and the regional foliation (Fig. 18). Rare chalcopyrite is locally observed associated with pyrrhotite in high-grade zones, and in late Pb-Zn-Ag veins. High-grade Mo mineralization is restricted to the upper portions of the host dike and becomes progressively less enriched with increasing depth.

Molybdenite is associated with each of the alteration assemblages. Biotite–molybdenite intergrowths are observed in the high-grade and potassic altered core of the deposit. Muscovite–molybdenite intergrowths are widely distributed and correspond to phyllic alteration. These intergrowths are the end-product of two different scenarios: (1) feldspar–molybdenite intergrowths where the feldspar has been completely replaced by muscovite, and (2) muscovite–molybdenite intergrowths where muscovite and molybdenite are coeval. Minor molybdenite disseminations are associated with late propylitic alteration halos along quartz

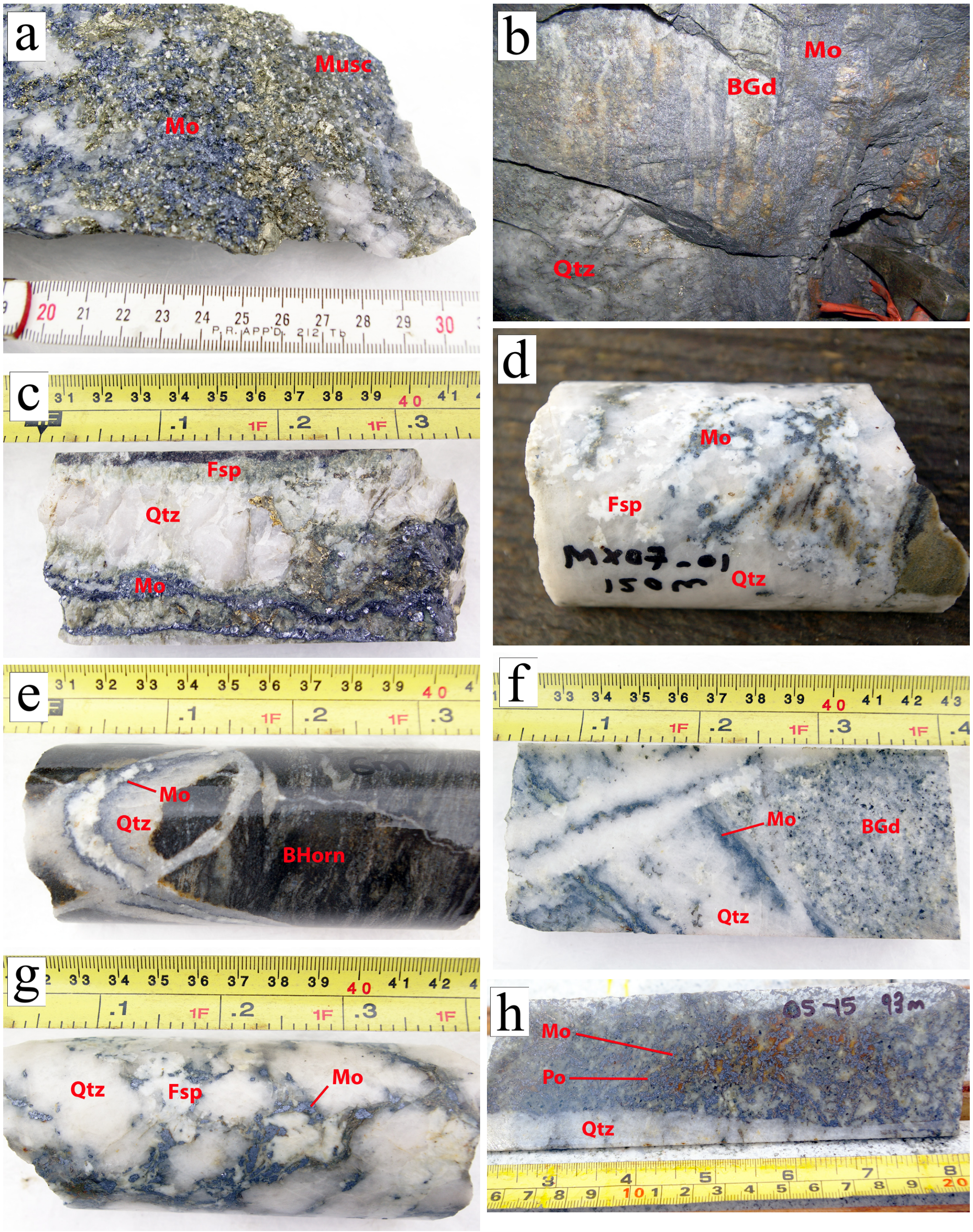

Figure 17. (a) Molybdenite (Mo)-muscovite (Musc) intergrowths from quartz stockwork crosscutting high-grade zone; (b) molybdenite stringers from high-grade zone crosscutting biotite granodiorite (BGd); (c) molybdenite-rich selvages along quartz (Qtz)-K feldspar (Fsp) vein margin; (d) molybdenite–K feldspar intergrowths in high-grade zone; (e) molybdenite-rich quartz-feldpsar vein crosscut by barren quartz vein within biotite hornfels (BHorn); (f) crosscutting Mo-bearing veins; (g) molybdenite–K feldspar intergrowths; (h) molybdenite–pyrrhotite intergowths .

vein margins. Recent drilling has confirmed the presence of rare molybdenite in peripheral W skarn and Pb-Zn-Ag veins.

The highest Mo grades are positively correlated with the intensity of silicic and potassic alteration (Fig. 13). The decrease in quartz ± K feldspar vein abundance away from high-grade mineralization likely reflects a reduced fluid flux (Linnen and Williams-Jones, 1987). Sheeted quartz ± K feldspar veins crosscut irregular molybdenite stringers and are in turn crosscut by variably oriented mineralized quartz ± K feldspar veins within the stockwork. All

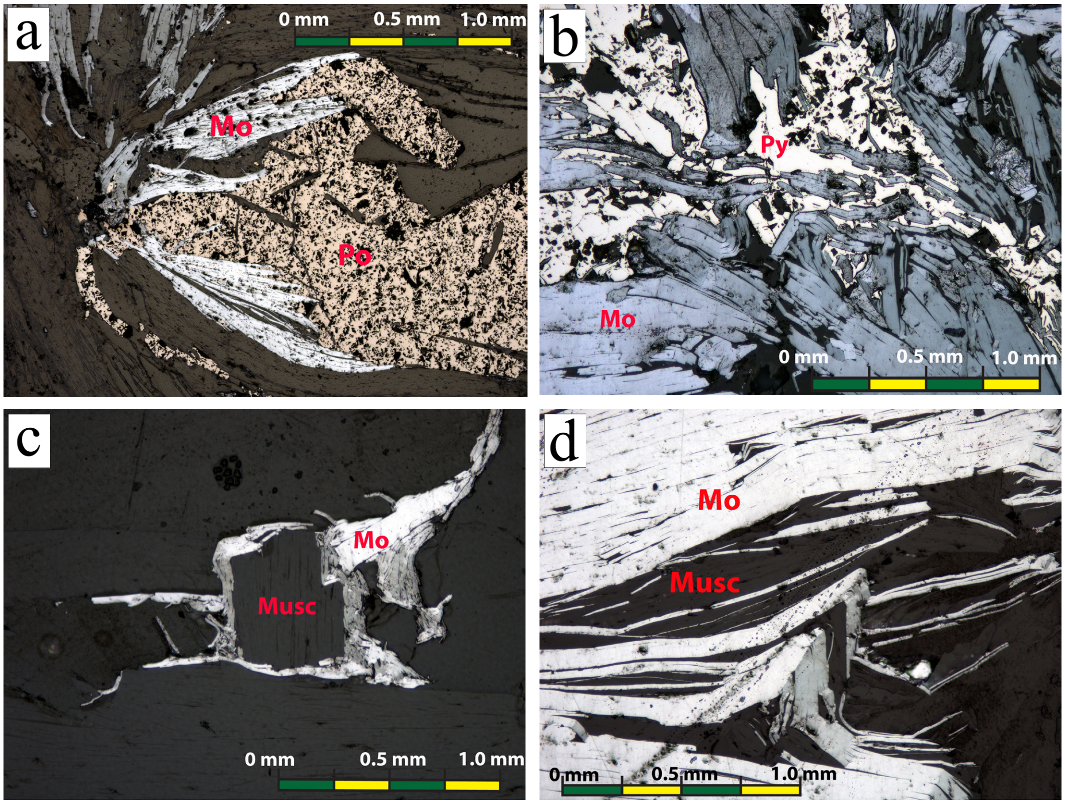

Figure 18. Reflected light photomicrographs of ore vein textures. (a) molybdenite (Mo)–pyrrhotite (Po) intergrowths typical of high-grade zone; (b) pyrite (Py)–molybdenite intergrowths commonly associated with phyllic alteration; (c and d) molybdenite–muscovite (Musc) intergrowths. This texture is typically associated with phyllic alteration

mineralized quartz ± K feldspar veins crosscut folded quartz sweats within the Broadview Formation, which are most likely the product of Jurassic deformation and predate the intrusion of the Trout Lake stock. This temporal order of quartz veining was used to broadly identify early and late Mo mineralization for the purposes of Re–Os geochronology and fluid inclusion study.

Quartz ± feldspar (plagioclase and/or K feldspar) veins commonly show evidence of open-space filling and repeated opening and regeneration of mineralized fluids. Euhedral quartz and feldspar crystals growing away from quartz veins margins are commonly observed. Many veins possess multiple molybdenite-rich selvages, which is indicative of multiple fluid flow events. Underground exposures at MAX provide a natural laboratory to observe magmatic–fluid evolution in a porphyry system. Narrow granodiorite dikes can be observed filling the medial portions of mineralized veins, which are in turn crosscut by mineralized quartz veins (Fig. 12). Complex crosscutting relationships between mineralized quartz ± feldspar veins and granodiorite dikes suggests all events occurred contemporaneously as the source intrusion differentiated at depth (Boyle and Leitch, 1983).

Unidirectional solidification textures (UST) provide further evidence of a rhythmic period of mineralization that is typical of porphyry deposit cupola zones (Figs. 19–21; Shannon et al., 1982; Kirkham and Sinclair, 1988; Lowenstern and Sinclair, 1996). Crenulated quartz and K feldspar veins known as “brain rock” provide an example of a UST (Fig. 19). These textures are interpreted to represent periodic release of volatiles at the top of a cooling magma chamber (Lowenstern

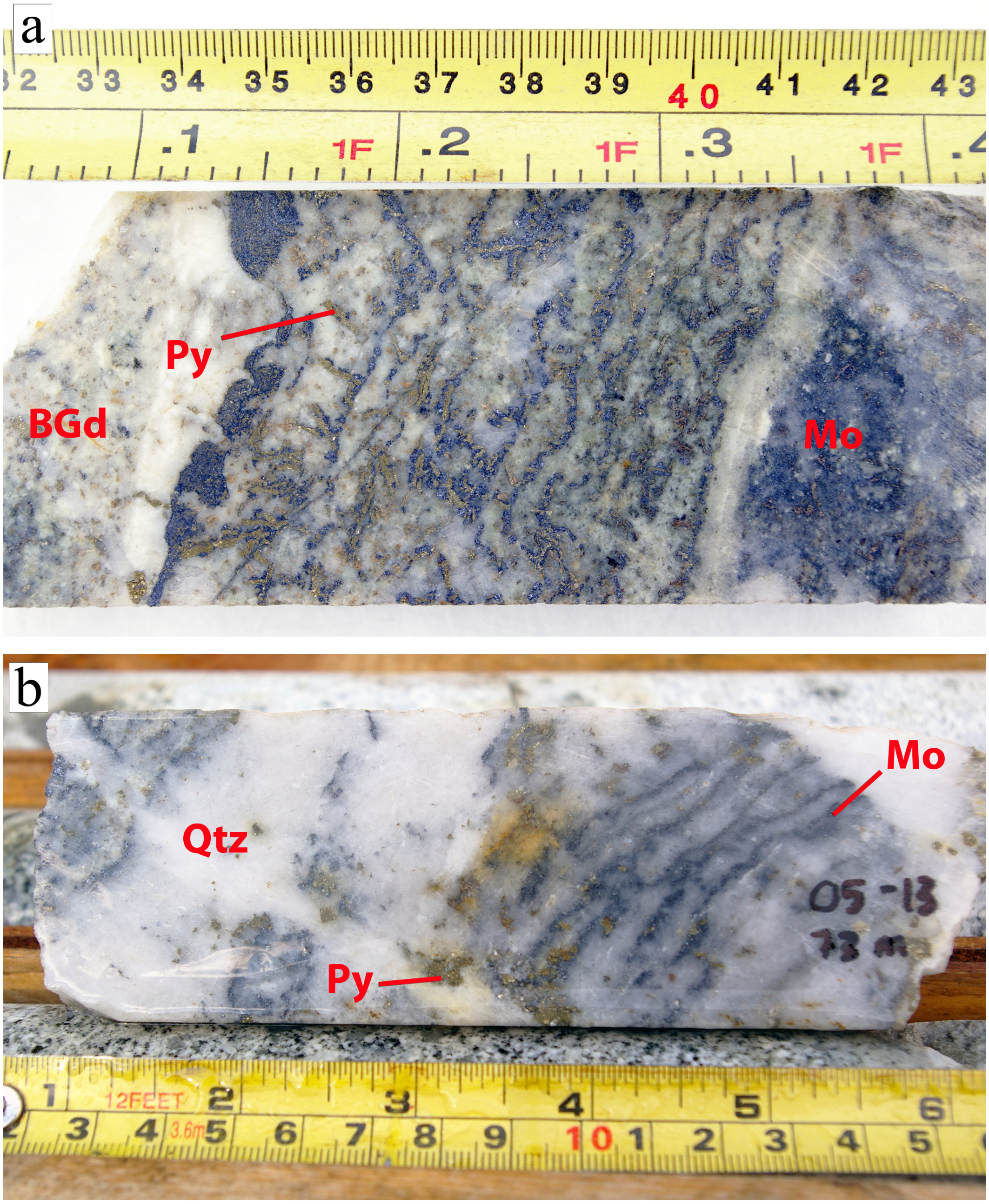

Figure 19. (a) Mo-bearing “brain rock” at the margin of a biotite granodiorite (BGd) dike. Note pyrite (Py)–molybdenite (Mo) intergrowths; (b) undulating Mo stringers in quartz veins (qtz).

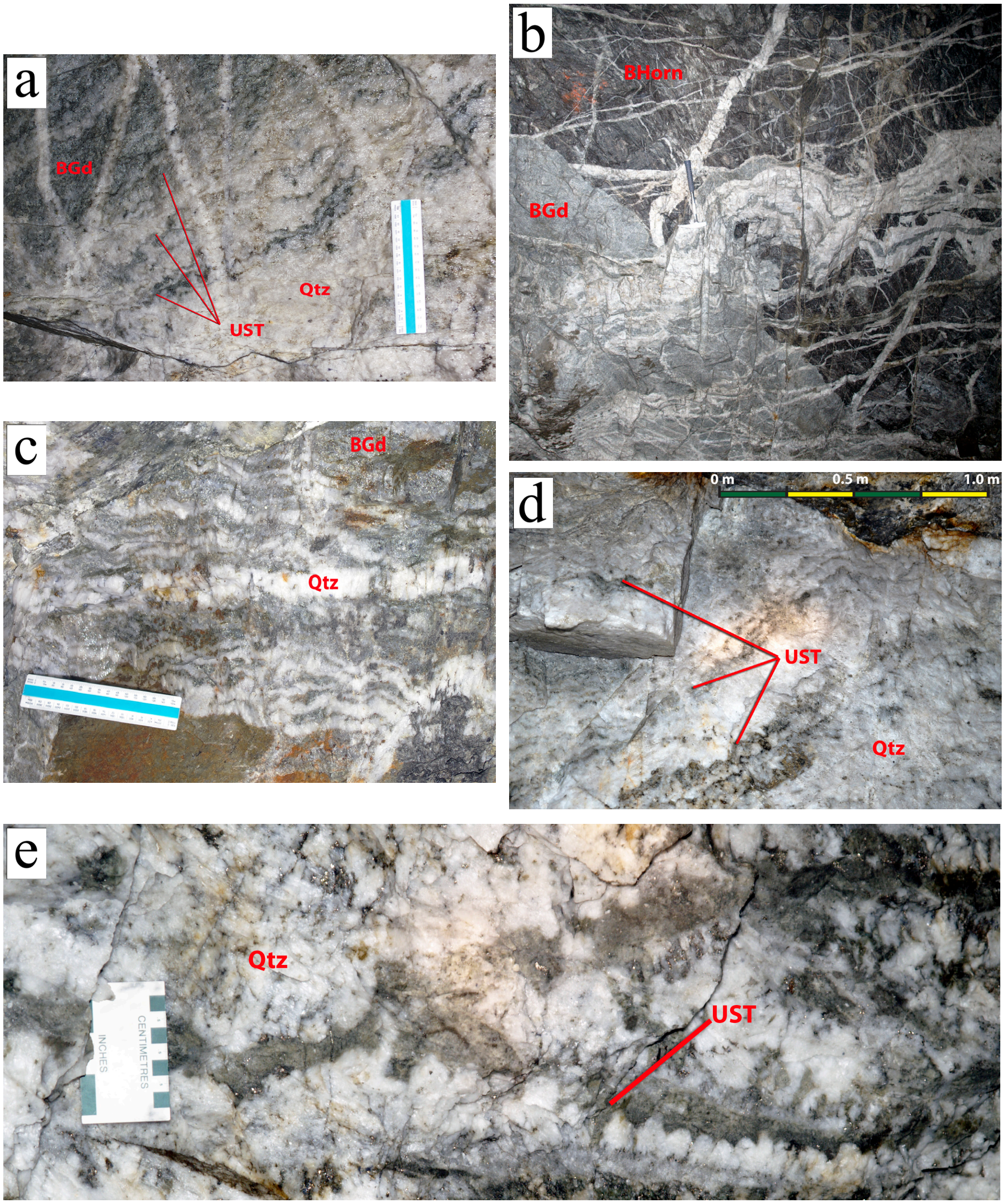

Figure 20. (a–e) Unidirectional solidification textures (UST) within biotite hornfels (BHorn) located adjacent to the high-grade zone on 960L. Couplets of undulating biotite granodiorite (BGd) dikes and euhedral quartz (Qtz) crystals record periodic build-up and release of volatiles from the cooling Trout Lake stock.

and Sinclair, 1996). Volatile saturation is a common process in evolved magma systems due, in part, to resurgent boiling. These volatiles accumulate at the tops of magma chambers due to their lower density and cause progressively increasing fluid pressure. During fluid pressure build-up, euhedral quartz and feldspar crystal grow into fluid-filled space (Lowenstern and Sinclair, 1996). Eventually fluid pressure exceeds the lithostatic load and fractures begin to propagate into the

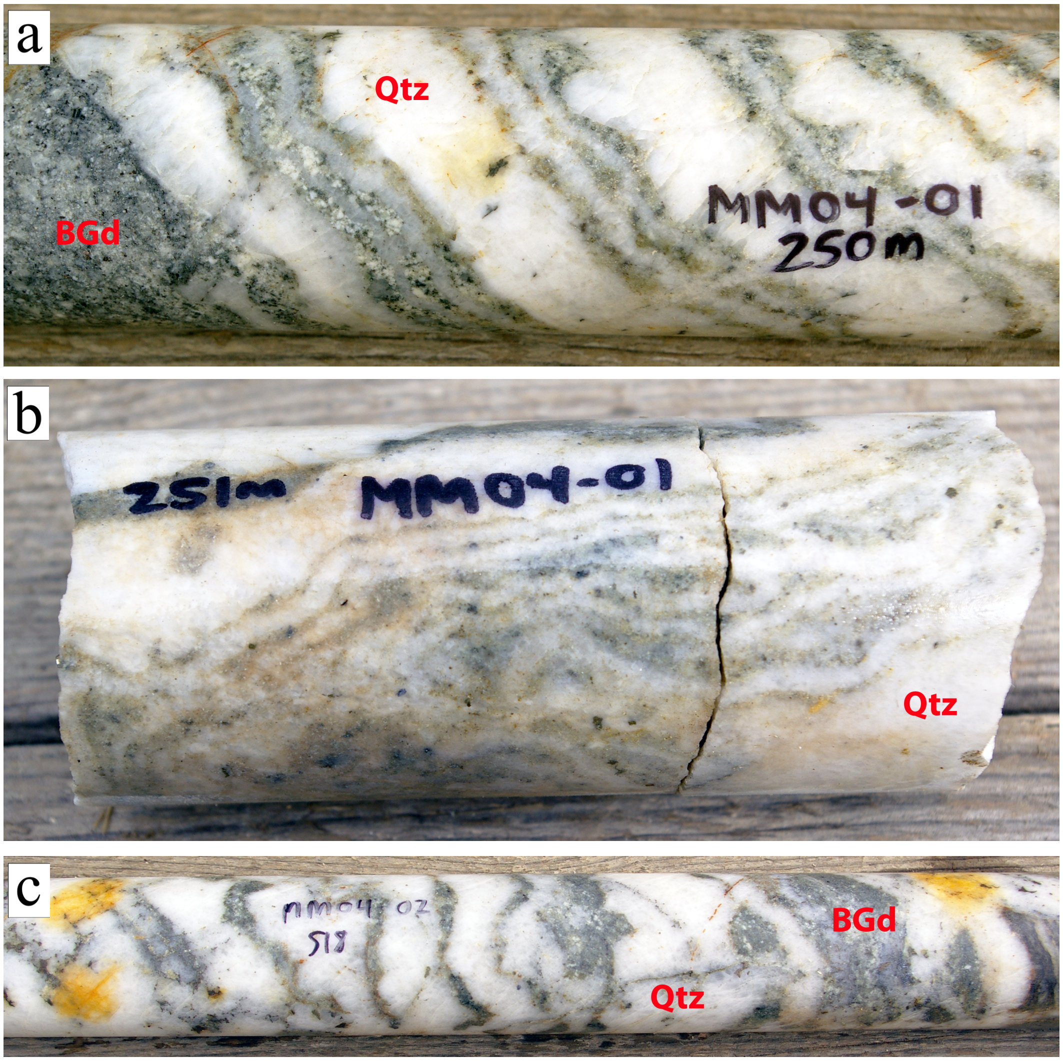

Figure 21. (a–c) Unidirectional solidification textures (UST) in core.

country rock. The fractures rapidly seal with quartz ± K feldspar ± molybdenite and allow fluid-pressure to rebuild. During fluid escape, pressure drops drastically and magma becomes pressure quenched into the interstices of euhedral quartz-K feldspar crystals (Lowenstern and Sinclair, 1996). Each euhedral quartz-feldspar and undulating porphyritic couplet represents one cycle of pressure build-up and release (Kirkham and Sinclair, 1988). Unidirectional solidification textures at MAX record dozens of these cycles. Repeated generation of hydrothermal fluids explains the complex nature of the magmatic–hydrothermal system at most porphyry deposits.

2.3.4 W Mineralization

During World War 2, scheelite was mined from Copper Chief and the Lucky Boy dump. Underground workings at both properties are now badly caved and inaccessible. Fyles and Eastwood (1962) describe the scheelite-bearing skarn as a green pyrrhotite-diospide-garnet-bearing unit that grades into buff colored skarn and gray marble. Scheelite within these zones is fine-grained and is visible only with the aid of ultraviolet light. WO_3 grades within these zones can reach 1.62% over 4 feet (Fyles and Eastwood, 1962). Several hundred feet of development were completed at Copper Chief until work stopped in 1943.

Recent drilling by Roca Mines has targeted similar skarn zones adjacent to MAX. Scheelite in these zones is also associated with clinopyroxene ± garnet ± pyrrhotite skarn lenses. Skarn is strongly developed in close proximity to major faults and in contact with granodiorite. Scheelite is present as coarse pyramid-shaped disseminations and fine grained mono-mineralic stringers (Fig. 22). Quartz veins crosscutting skarn lenses locally possess fine grained disseminated scheelite. The highest WO_3 grades are positively correlated with the most intensely replaced zones and are semi-continuous down-dip towards the Trout Lake stock. Mo- and Pb-Zn-Ag-bearing veins locally crosscut mineralized skarn.

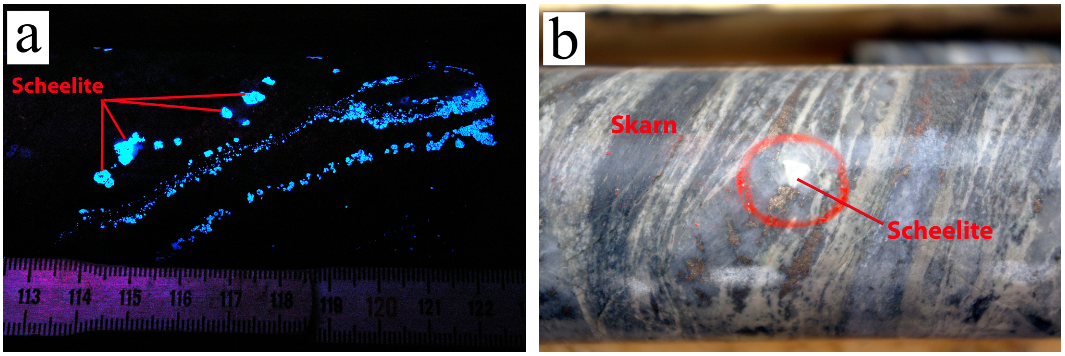

Figure 22. (a) Scheelite-bearing skarn viewed under ultraviolet light; (b) coarse-grained scheelite with pyramid-shaped habit.

2.3.5 Pb-Zn-Ag Mineralization

Pb-Zn-Ag veins are present throughout the Kootenay Arc and represent British Columbia's only Pb-Zn-Ag metallogenic province. Fyles (1966) identified two Pb-Zn-Ag deposit types based on their relationship with the surrounding country rocks. Concordant-type deposits are stratiform and commonly associated with calcareous rocks. These deposits are typically interpreted to be pre-metamorphic (Muraro, 1966). Transgressive-type deposits are associated with narrow quartz veins that crosscut the country rock. The area around MAX possesses both concordant- and discordant-type Pb-Zn-Ag deposits. Trout Lake mineral deposits have been described by a number of authors including Brock

(1904), Emmens (1914), Walker et al. (1929), and Fyles (1966). Brock (1904) was the first to recognize that Pb-Zn-Ag deposits could be subdivided into three belts: Lime Dyke, Central, and Southwest. All three belts strike parallel to the regional foliation. Deposits around the Trout Lake stock are situated in the Southwest belt and include: Copper Chief, Horseshoe, Lucky Boy, Ethel, and Craig. Walker et al. (1929) suggested that some of these deposits were related to magmatic fluids.

Very little is known about these deposits. Sinclair (1966) sampled galena ore from 16 deposits in the Kootenay Arc and was able to distinguish two classes of Pb-Zn-Ag deposits based on their lead isotopic composition. The Sullivan ore body belongs to the single-stage group of deposits that are interpreted to have formed in a single U-Th environment through time. A number of deposits record a more complicated history and have been termed multi-stage or anomalous lead deposits. Sinclair (1966) suggested that these deposits may have formed as a result of local melting related to Jurassic–Cretaceous plutonism. Andrew et al. (1984) built on this early work and included additional galena ore samples to expand their results to similar Pb-Zn-Ag deposits in Idaho and Montana.

Recent drilling at MAX has intersected Pb-Zn-Ag veins that are identical in appearance and metallogeny to those described at the nearby Lucky Boy and Copper Chief deposits. Argentiferous galena, sphalerite, tetrahedrite, and rare molybdenite are disseminated within 10 to 30 cm wide quartz veins (Fig. 23). These veins extend to >1 km below the current workings at 960L, and have also been intersected above and peripheral to MAX. Base metal veins are almost exclusively associated with late propylitic alteration. The relative timing of mineralization, magmatic activity, hydrothermal alteration, and paragenetic veins is summarized in Fig. 24.

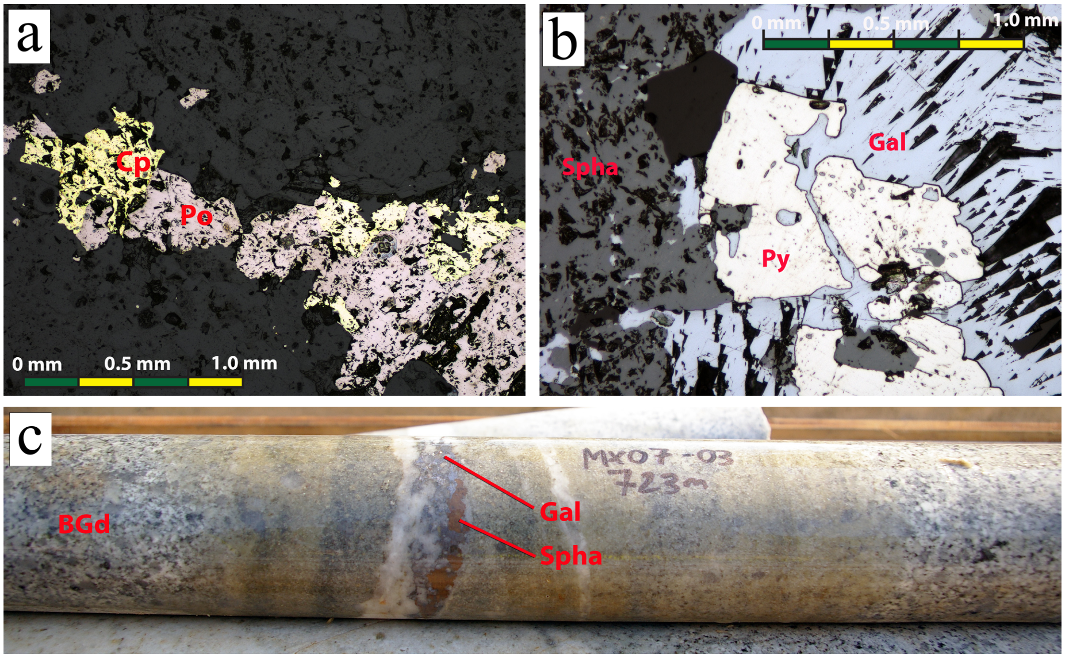

Figure 23. (a) Reflected light photomicrograph of rare chalcopyrite (Cp) associated with pyrrhotite (Po) in late vein peripheral to MAX; (b) reflected light photomicrograph of pyrite (Py), galena (Gal), and sphalerite (Spha) in late vein peripheral to MAX; (c) typical late Pb-Zn-Ag vein crosscutting biotite granodiorite (BGd) with propylitic alteration.

2.4 Analytical Methods

2.4.1 Lithogeochemical Methods

Lithogeochemistry was completed at Actlabs, in Ancaster, Ontario. A representative suite (16 samples) of each of the intrusive phases was collected to deduce host-rock petrogenesis. An additional 4 samples were collected from nearby Jurassic plutons (e.g., Kuskanax batholith, and Galena Bay stock). Pervasively-altered dikes representative of each alteration assemblage were

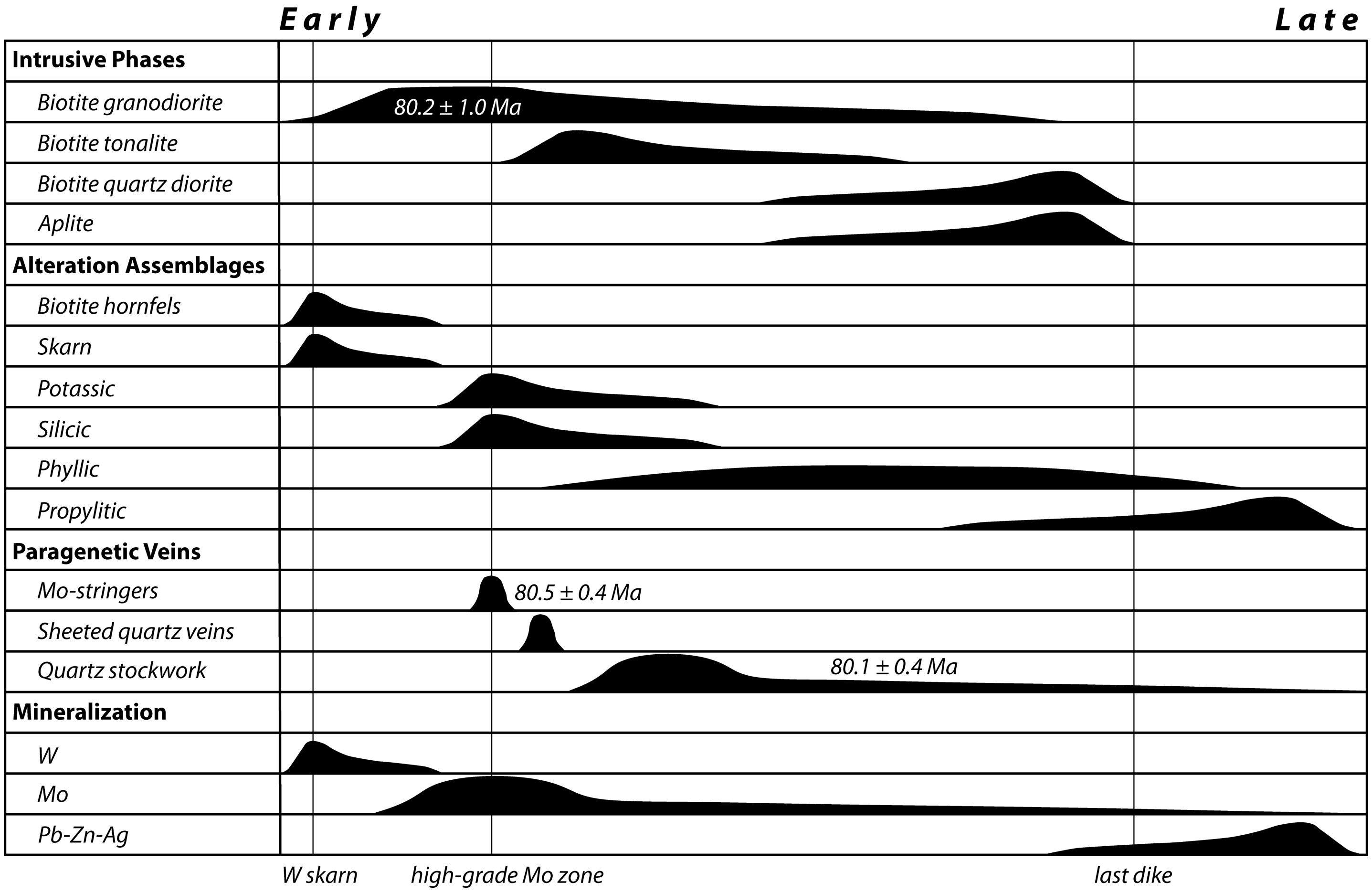

Figure 24. Paragenetic sequence showing the relative timing of magmatic and hydrothermal activity at MAX.

sampled to compare against less-altered intrusive phases. Samples were crushed and pulverized to pass through 150 mesh, and analyzed using a combination of fusion inductively coupled plasma-mass spectrometry (ICP-MS) and instrumental neutron activation analysis (INAA). The assay package used was research grade “Code 4E”. Detection limits for this assay package are typically in the low ppm and ppb range. Selected samples were split and both aliquots were analyzed as a means of quality control. Difference between sample splits was <0.5 wt. % for major elements and <1 ppm for most trace elements. All geochemical diagrams were plotted using Petrograph (Petrelli et al., 2005).

2.4.2 Re–Os Geochronology Methods

Three molybdenite mineral concentrates were collected in order to determine the duration of mineralizing events at the MAX. One sample of early molybdenite stringers, CL100, was collected from the high-grade ore zone at 920L. Two samples of late molybdenite-rich quartz veins, CL200 and CL300, were collected from the quartz vein stockwork adjacent to and crosscutting the high-grade ore zone. Collectively, these samples represent the oldest and latest Mo mineralizing events within the paragenetic scheme. Molybdenite is a prized geochronometer because of its tendency to incorporate large concentrations of Re and insignificant nonradiogenic Os at the time of crystallization (Stein et al., 2001). This property allows a Re–Os model age to be calculated from the simplified isotope equation:

$t = \ln({}^{187}\mathrm{Os}/{}^{187}\mathrm{Re} + 1)/\lambda$

Where:

t = model age
λ = ^{187}Re decay constant (1.666 x 10^{-11} yr $^{-1}$; Smoliar et al., 1996)

Molybdenite concentrates were generated at the University of Alberta using modified mineral separation techniques that minimized contact with metal. Samples were pulverized with a porcelain disc mill and magnetic minerals were removed using a Frantz isodynamic magnetic separator. Molybdenite was separated using a combination of heavy liquids, and flotation with high-purity water. Final molybdenite concentrates were handpicked under a microscope as a last step in quality control.

^{187}Re and ^{187}Os were measured using isotope dilution mass spectrometry and the methods of Selby and Creaser (2004). Mass-dependent fractionation during analysis was corrected by using a mixed tracer solution with a well established ^{185}Re composition and isotopically normal Os. Samples were equilibrated with the Re–Os tracer using the Carius tube method. Purified Re and Os concentrates were then loaded onto barium-coated Pt filaments and the respective isotopic concentrations were measured using negative thermal ionization mass spectrometry (Creaser et al., 1991). Total procedure blanks are on the order of <5 pg for Re and <2 pg for Os. Re–Os model age errors account for uncertainties in mass spectrometry measurements, spike and standard Re–Os isotopic compositions, calibration of the tracer solution, and uncertainties with the Re–Os decay constant.

2.4.3 U–Pb Geochronology Methods

Thermal ionization mass spectrometry (TIMS) remains the most precise analytical method in U–Pb zircon geochronology. The precision and accuracy of TIMS is currently unequaled at the scale of individual zircon crystals (Cocherie and Robert, 2008). Granitoids that form in arc environments are the result of complex melting and emplacement histories (Richards and Kerrich, 2007). Zircon crystals record this complex history within distinct zones. Each zone represents a period of zircon growth and potentially records a different U–Pb isotopic composition. Conventional TIMS is unable to resolve zoned zircons because the entire mineral is typically digested. Laser ablation multi-collector inductively coupled mass spectrometry (LA-MC-ICP-MS) provides a possible alternative for dating complexly zoned zircons because of its capability to analyze 30–40 μm domains within individual zircons. The greater resolution of LA-MC-ICP-MS comes at the expense of precision, which is less than provided by TIMS.

Previous U–Pb geochronological studies of porphyry deposits have been plagued by complexly zoned zircons that hinder interpretation of the magma's crystallization age (e.g., Richards et al., 1999; Scott et al., 2008). This inherent feature of the zircon geochronometer was avoided in the present study by using the University of Alberta's Nu Instruments Plasma multi-collector inductively coupled plasma mass spectrometer (MC-ICP-MS) coupled with a New Wave Research UP213 laser ablation system. This system allows simultaneous measurement of ^{238}U, ^{235}U, ^{207}Pb, ^{206}Pb, ^{205}Tl, ^{204}Hg, ^{204}Pb, ^{203}Tl, and ^{202}Hg. Zircon mineral separates were prepared using traditional mineral separation techniques that include: crushing, pulverizing, Wilfley table, heavy liquid, magnetic separation, and hand picking. Zircon crystals were then mounted in epoxy pucks and polished.

Analytical methods and corrections are briefly described here and are summarized from Simonetti et al. (2005). Each analysis consists of 30 s of laser ablation and is followed by a period with no laser firing in order to purge the sample cloud from the chamber and prepare for the next analysis. Ablated material is then carried by He gas to the MC-ICP-MS. Spot sizes ranged from 30 to 40 μm depending on the zircon size.

Prior to any analysis a 30 s blank was measured. Blank measurements were repeated every 50 analyses in order to measure the ^{204}(Pb or Hg) contribution. After analyzing 12 MAX zircons, an in-house zircon standard (LH94-15) was analyzed. This standard–sample–standard bracketing technique allows instrumental drift to be measured and corrected for. Instrumental mass bias is an inherent feature of mass spectrometry due to mass-dependent fractionation during ionization. ^{205}Tl/^{203}Tl can be used to correct Pb mass fractionation by assuming fractionation per mass unit is constant. Prior to analysis, the ICP source was doped with a ~1 ppb Tl solution. Pb isotope ratios are then corrected using the difference between measured ^{205}Tl/^{203}Tl values before and after analysis.

Common-Pb is an important variable that must be controlled in any U–Pb geochronology study. Sources of common-Pb vary from the epoxy puck, carrier gas, isobaric interferences produced during laser ablation, or the zircon itself. Each analysis was corrected for common-Pb by using the projected age of the mineral and the corresponding initial Pb isotopic compositions taken from the two-stage evolution model of Stacey and Kramers (1975). Because MAX zircons contained extremely-low concentrations of common-Pb, the correction has minimal impact on the calculated dates.

Precision and accuracy can be greatly improved through proper sample selection. Zircons with obvious cracks or inclusions were avoided. Zoned zircons were analyzed more than once, where possible, to identify the U/Pb isotope ratios of the core and rim component. In total, 101 zircons were ablated from sample TL201, and 107 zircons were ablated from sample TL202. Concordia diagrams and $^{206}Pb/^{238}U$ weighted average ages were calculated using ISOPLOT (Ludwig, 1991). $^{206}Pb/^{238}U$ weighted average ages are calculated by weighting each $^{206}Pb/^{238}U$ age inversely to its analytical error so that $^{206}Pb/^{238}U$ ages with the most analytical error have minimal impact on the final weighted average. This method is advantageous because precision if often considered an indicator of measurement quality. Nevertheless, in the case of zircons, large analytical errors are commonly due to low U, and therefore low radiogenic Pb, concentrations, which make precise mass spectrometric measurements difficult. Such zircons, however, are least likely to undergo Pb-loss due to metamictization, and are therefore most likely to preserve undisturbed (accurate) crystallization ages, albeit with low precision. Weighted average ages therefore preferentially weight zircons according to their U contents and potentially bias the dataset towards ages reflecting Pb-loss. This effect was monitored by comparing weighted average ages to their un-weighted equivalent average ages.

2.4.4 Fluid Inclusion Methods

A suite of 6 samples from Pb-Zn-Ag-bearing quartz veins were selected for fluid inclusion analysis. A further 9 samples of Mo-bearing veins from each of the paragenetic vein sets were collected to compare the P-T-X conditions of the hydrothermal fluids. Quartz is the dominant vein gangue mineral and is host to all of the fluid inclusions analyzed. Doubly polished thin sections were prepared and selected chips were analyzed using a Linkham THMSG600 microthermometric stage. Calibration was completed at the beginning and end of study using CO_2 and H_2O standards. Temperature measurements are accurate to ±0.1°C near or below 0°C and ±1°C above 100°C. Fluid inclusions were supercooled to -120°C and then heated until total homogenization (Th) of the fluid inclusion. All possible phase changes were recorded during each heating experiment. Sequential freezing was occasionally required to obtain accurate melting temperatures (Haynes, 1985).

2.5 Results

2.5.1 Lithogeochemistry Results

Widespread hydrothermal alteration at MAX makes sampling of unaltered intrusive phases impossible. The effects of the different alteration assemblages is evident in the major element chemistry. Secondary quartz, K feldspar, plagioclase, muscovite, and biotite have a strong impact on major element chemistry and hinder petrogenetic interpretation. In order to minimize the effects of secondary minerals, the least altered examples of each intrusive phases were collected, and strongly altered rocks have been identified on geochemical diagrams.

Total alkalis vs. silica diagrams (TAS) provide a convenient means of comparing major element chemistry between samples (Fig. 25). All samples have been normalized to a volatile free basis by subtracting the weight percent of "loss on ignition" (LOI) and renormalizing SiO_2 and alkalis to the new total. Most of the MAX intrusive phases plot in the granite field of the diagram. Least altered biotite granodiorite and biotite tonalite dikes plot in a tight cluster, whereas aplite dikes possess compositional variability. Three pervasively-altered granodiorite dikes plot away from the other intrusive phases due to varying degrees of silicification. The apparent isolation of the trondhjemite dike, relative to other MAX phases, justifies its classification as a separate intrusive phase (discussed

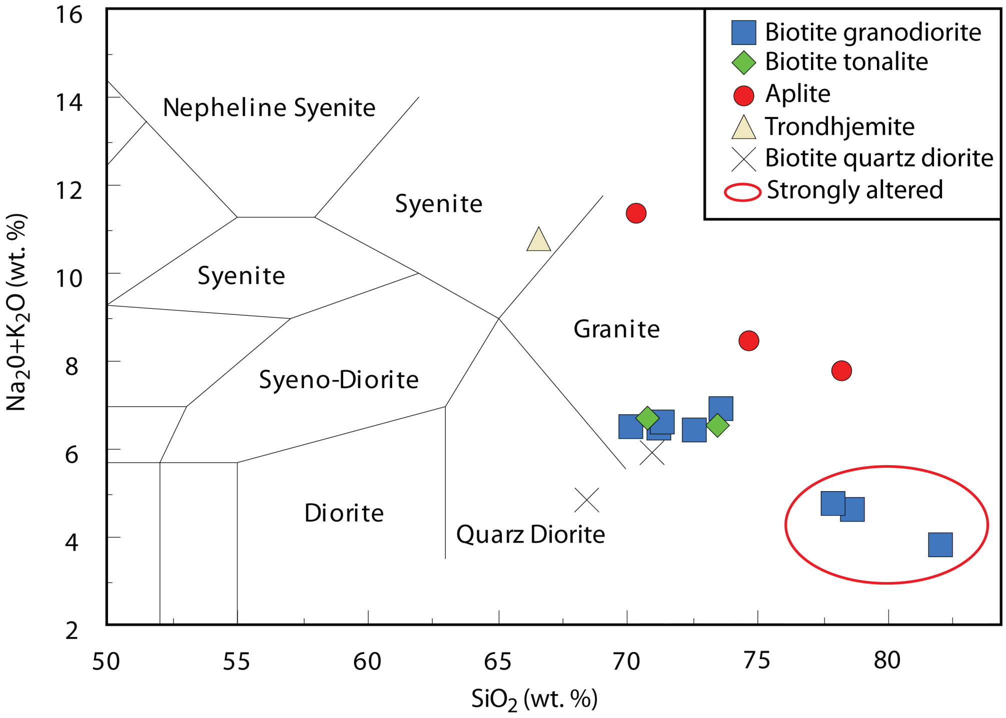

Figure 25. Scatter plot of total alkalis ($Na_2O + K_2O$) vs. SiO_2 (modified from Cox et al., 1979).

above) and reflects a large modal proportion of sodic plagioclase.

Harker variation diagrams plot SiO_2 (wt. %) against other major and minor element oxides (wt. %). Unmodified rock suites that are related through fractional crystallization typically exhibit strong correlations between SiO_2 and the other element oxides. Smooth trends can be modeled to better understand fractional crystallization and parent rock composition. Weak correlations are a symptom of several potential processes: hydrothermal alteration, sample heterogeneity, and the combined effects of complex igneous processes (partial melting, fractional crystallization, magma mixing, and crustal contamination). MAX phases exhibit significant scatter even when the most intensely altered dikes are ignored (Fig. 26). The presence of secondary minerals associated with each of the alteration assemblages at MAX best explains the observed scatter in Harker variation diagrams.

The partitioning behavior of trace elements is a function of temperature, pressure, fO_2, and the bulk chemical composition of the melt and mineral. The majority of trace elements do not strongly partition into the common rock-forming minerals (i.e., quartz, feldspar, pyroxene, olivine, and amphibole). As a result, the abundance and character of accessory minerals exerts a strong control on trace element distribution. Zircon, apatite, and allanite are the dominant accessory phases in MAX intrusive rocks.

Rare earth element (REE) profiles for altered and unaltered biotite granodiorite dikes are indistinguishable (Fig. 27). Biotite granodiorite dikes are all enriched relative to chondrite values and possess gently–dipping slopes

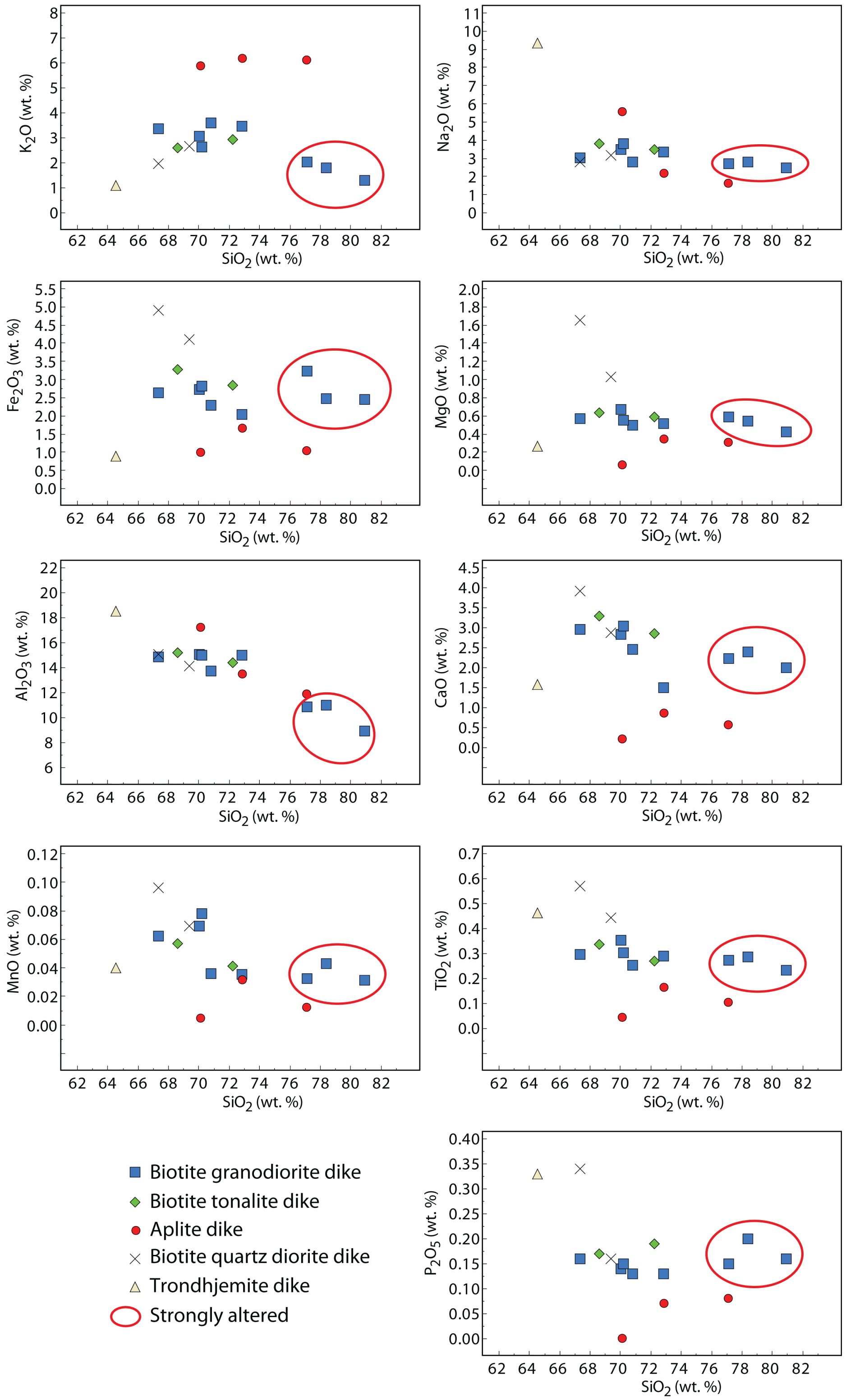

Figure 26. Harker variation diagrams plotting major element oxide (wt.%) vs. SiO_2 (wt. %).

towards the heavy rare earth elements (HREE). Younger biotite tonalite dikes tightly cluster with the REE pattern of granodiorite dikes. Progressively younger aplite dikes exhibit a flatter slope and are typically relatively-enriched in HREE and depleted in light rare earth elements (LREE) compared to biotite granodiorite and biotite tonalite dikes (Fig. 28). Aplite dikes also possess small-negative Eu anomalies that are consistent with plagioclase fractionation. Biotite quartz diorite and trondhjemite dikes also possess distinct REE patterns. Two biotite quartz diorite samples share similar LREE concentrations as granodiorite samples but are enriched in HREE. Trondhjemite dikes can be distinguished from biotite tonalite dikes by the occurrence of abundant sodic-plagioclase phenocrysts and a lighter-gray color. This later trondhjemite phase also possess a distinct REE pattern that is the most enriched in LREE and possesses a small-negative Eu anomaly.

All MAX phases exhibit similar patterns when plotted on extended trace element diagrams normalized to primitive mantle (Fig. 29). Late aplite dikes possess more fractionated patterns that are typical of late-stage magmatic phases. Granites in arc environments typically possess enriched spikes at U, K, and Pb in combination with negative spikes at Ta, Nb, and Ti.

Four samples from the nearby Galena Bay Stock and Kuskanax Batholith were collected to compare the chemistry of the Trout Lake stock to other nearby intrusive bodies. The trace element concentrations from each of these intrusive bodies is distinct (Fig. 30). Kuskanax batholith REE distributions are enriched relative to chondrite values and possess a weak U-shape. LREE are depleted relative to MAX igneous phases, whereas HREE concentrations are similar to

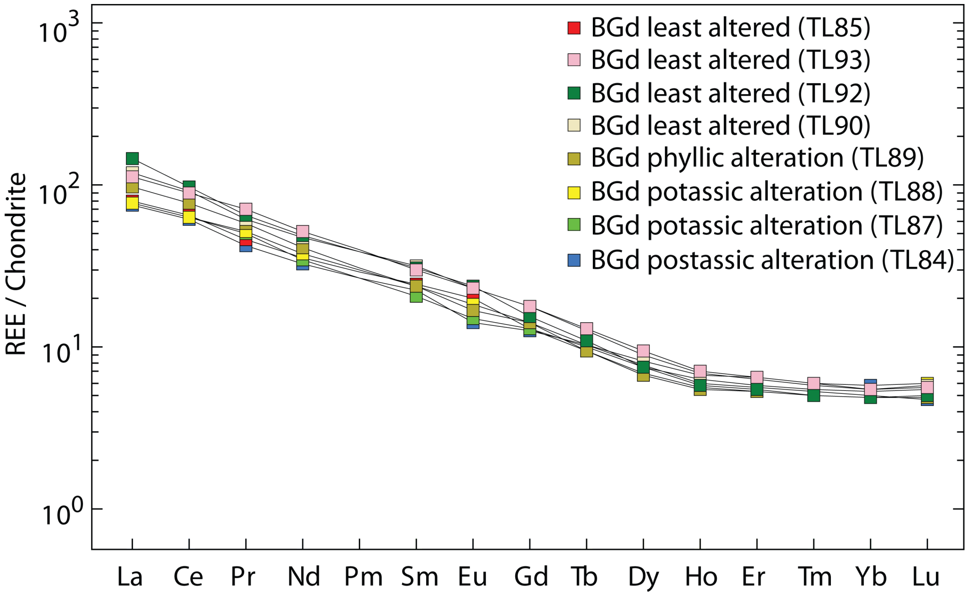

Figure 27. REE profiles of biotite granodiorite dikes (BGd). Alteration assemblages and intensity have no impact on REE profiles. REE normalized to Cl chondrite values of Sun and McDonough (1989).

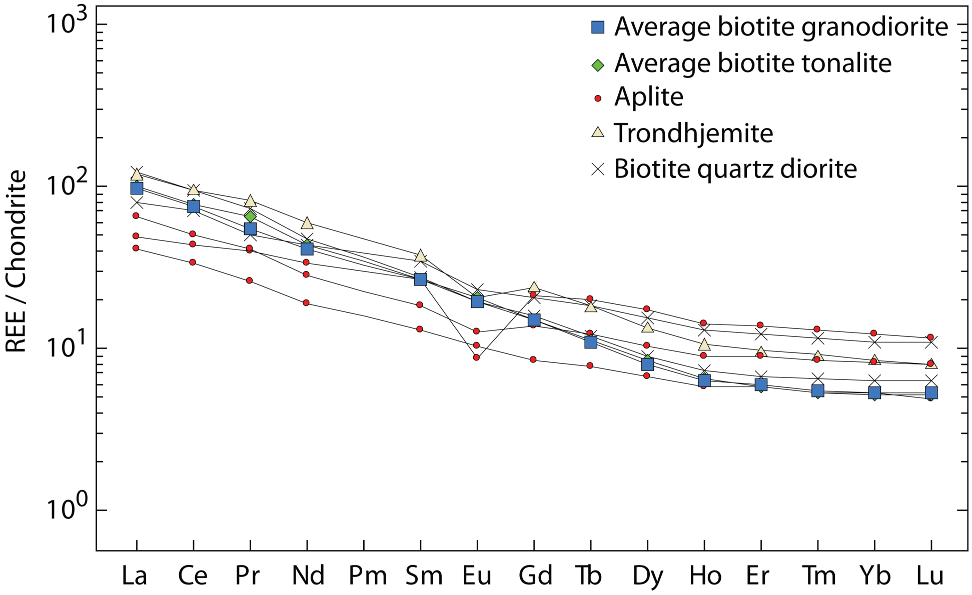

Figure 28. REE profiles of all MAX instrusive phases. Note the differences between late-stage aplite dikes and early granodiorite and tonalite dikes. REE normalized to Cl chondrite values of Sun and McDonough (1989).

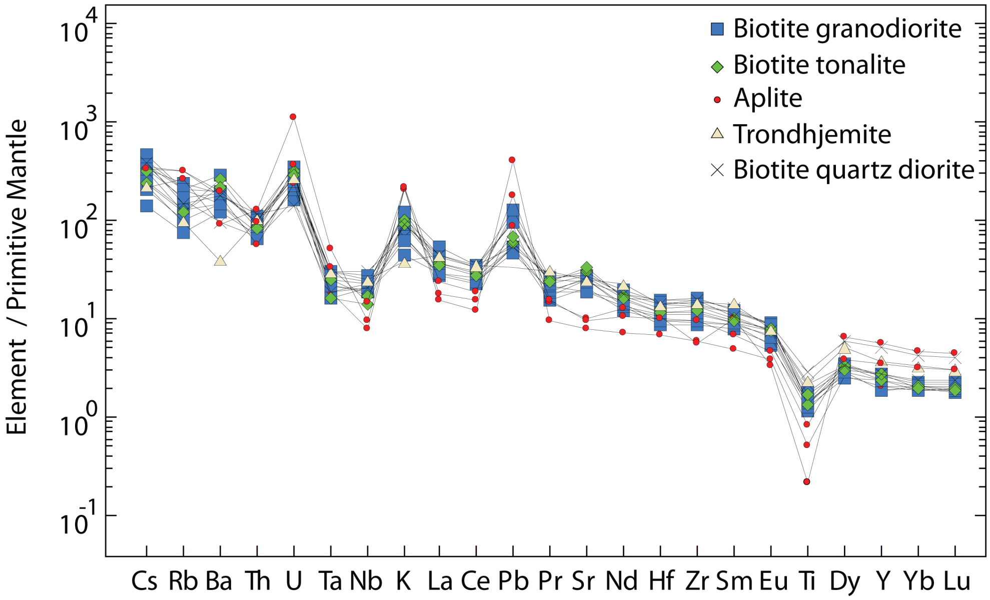

Figure 29. Extended trace element diagram with all MAX intrusive phases normalized to the primitive mantle values of McDonough and Sun (1995). Enriched spikes at U, K, and Pb, and negative spike at Ta, Nb, and Ti are typical of arc granites.

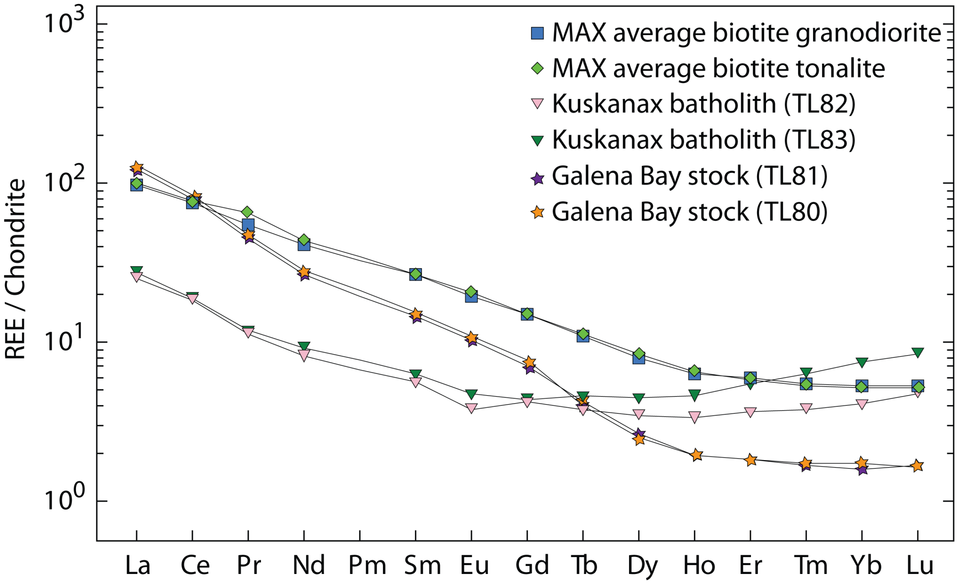

Figure 30. REE profiles of average MAX biotite granodiorite and biotite tonalite compared to samples of the Kuskanax and Galena Bay plutons. REE normalized to Cl chondrite values of Sun and McDonough (1989).

MAX. Galena Bay stock REE distributions possess a gently–dipping pattern towards the HREE. LREE are similar to MAX igneous phases but possess significantly lower HREE concentrations. The dissimilarity of these trace element patterns to MAX suggests that they are not genetically related.

2.5.2 Geochronology Results

Re–Os Geochronology Results

Re content in ~99% molybdenite varied from 19.71 to 44.15 ppm, and total Os varied from 2.5 to 3.5 ppb. Model ages for the three samples are 80.5 ± 0.4 Ma, 80.2 ± 0.4 Ma, and 80.1 ± 0.4 Ma (Table 1). Errors are reported at the 2σ level and include uncertainties in mass spectrometry measurements, spike and standard Re–Os isotopic compositions, calibration of the tracer solution, and uncertainties with the ^{187}Re decay constant (1.666×10^{-11} yr $^{-1}$; Smoliar et al., 1996). All three samples are within analytical error of each other and provide strong evidence that molybdenite was deposited over a restricted time period. A weighted average of all three model ages calculated by ISOPLOT (Ludwig, 1991) is 80.3 ± 0.2 Ma at 2σ (MSWD = 1.06).

Sinclair (pers. commun.) provide an up-to-date compilation of Re data for molybdenite samples from around the world. Different Mo deposit types can be distinguished based on the Re content in molybdenite. BC porphyry Mo deposits are characterized by a range of Re from 10 to 100 ppm. Other porphyry Mo deposits in Colorado possess a similar range. Re in MAX molybdenite concentrates range from approximately 20 to 44 ppm and are typical of porphyry

Mo deposits. Molybdenite from porphyry Cu-Au deposits contain significantly higher Re contents.

Table 1. Re-Os data for three molybdenite samples

Sample	Re (ppm)	± 2σ	^{187}Re (ppb)	± 2σ	^{187}Os (ppb)	± 2σ	Total common Os (pg)	Model Age (Ma)	± 2σ
CL100[1]	44.15	0.15	27.75	0.09	37.25	0.03	3.5	80.5	0.4
CL200[2]	19.71	0.07	12.39	0.04	16.55	0.02	2.5	80.1	0.4
CL300[2]	35.16	0.12	22.10	0.08	29.56	0.03	2.6	80.2	0.4

[1] CL100 is a sample of molybdenite from an early vein

[2] CL200 and CL300 are samples of molybdenite from late quartz veins.

U–Pb Geochronology Results

Molybdenite mineralization is spatially and temporally related to granodiorite dikes. Crosscutting relationships observed in underground exposures and core suggest that the majority of dikes crosscut and are crosscut by Mo-bearing quartz veins (Fig. 12). The intermineral nature of granodiorite dikes places additional constraints on the timing of Mo mineralization. The only previous geochronology on the Trout Lake stock is a K–Ar biotite date of 78.6 ± 2.9 Ma (deMille, 1976). Two intrusive dikes were selected for U–Pb geochronology in order to quantify the crosscutting relationships observed in the field. TL201 is a sample of an intermineral biotite granodiorite dike adjacent to the high-grade zone on 960L. TL202 is a sample of biotite granodiorite collected from drill core down-plunge of high-grade mineralization that hosts the majority of Mo mineralization. U–Pb geochronology dates the timing of igneous activity and acts as an independent check on the timing of mineralization obtained from

Re–Os molybdenite dating.

MAX zircons exhibit obvious signs of inheritance when plotted on concordia diagrams (Figs. 31–34). Inheritance is also confirmed by those zircons that were ablated at the core and rim. Zoned zircons are informative; however, they hinder the interpretation of dike crystallization ages. As a result, zircons with obvious inheritance were removed from the data set in order to better constrain the crystallization age of the dikes. The intermineral nature of granodiorite dikes allows Re-Os molybdenite geochronology to place geologically-reasonable upper-limits on dike crystallization ages. A weighted average of three Re-Os molybdenite dates is approximately 80 Ma. The average 2σ error on individual ^{206}Pb/^{238}U zircon ages is approximately 15 Ma. As a result, zircons with ^{206}Pb/^{238}U ages of <95 Ma are within the average 2σ error of the expected age. Zircons with ^{206}Pb/^{238}U ages ≥95 Ma were interpreted to be the result of inheritance and were excluded from the averages.

Weighted average ^{206}Pb/^{238}U ages for concordant zircons with ages <95 Ma from samples TL201 and TL202 (Tables 2 and 3) are within analytical error of each other at 80.9 ± 1.6 Ma (MSWD = 0.43, n = 66) and 80.2 ± 1.0 Ma (MSWD = 1.05, n = 70), respectively. Weighted average errors are reported at 2σ and include analytical uncertainties propagated according to Simonetti et al. (2005) and include uncertainty in the ^{238}U decay constant of Jaffey et al. (1971). Unweighted ^{206}Pb/^{238}U average ages for samples TL201 and TL202 are 81.0 Ma and 80.3 Ma, respectively, and are very similar (within error) to the weighted average ages, suggesting that Pb-loss from U-rich zircons is not a problem in this dataset.

Table 2. U-Pb data of selected 52 zircons from sample TL201 (see text).

Grain ID	^{206}Pb cps	^{204}Pb cps	^{206}Pb/^{238}U	2σ error	^{207}Pb/^{235}U	2σ error	^{207}Pb/^{206}Pb	2σ error	rho	^{206}Pb/^{238}U AGE (Ma)	2σ error	^{207}Pb/^{235}U AGE (Ma)	2σ error
TL201-34	112112	0	0.01159	0.00197	0.07864	0.01353	0.04923	0.00117	0.990	74.3	12.6	76.9	12.7
TL201-21	243046	163	0.01172	0.00197	0.07951	0.01348	0.04921	0.00092	0.994	75.1	12.6	77.7	12.6
TL201-40-1	204188	149	0.01178	0.00197	0.07913	0.01453	0.04873	0.00365	0.913	75.5	12.6	77.3	13.6
TL201-29	34197	0	0.01185	0.00198	0.07923	0.01390	0.04848	0.00265	0.950	76.0	12.6	77.4	13.0
TL201-32	219742	117	0.01186	0.00198	0.08003	0.02092	0.04894	0.00986	0.637	76.0	12.6	78.2	19.5
TL201-12	27438	0	0.01195	0.00198	0.08087	0.01385	0.04910	0.00219	0.966	76.6	12.6	79.0	12.9
TL201-35	90527	0	0.01201	0.00198	0.08207	0.01370	0.04957	0.00141	0.985	76.9	12.6	80.1	12.8
TL201-17	75495	0	0.01209	0.00198	0.08652	0.04236	0.05192	0.02396	0.334	77.4	12.6	84.3	38.8
TL201-65	136652	0	0.01210	0.00198	0.08189	0.01348	0.04910	0.00100	0.992	77.5	12.6	79.9	12.6
TL201-49	90158	143	0.01211	0.00198	0.08208	0.01362	0.04915	0.00147	0.984	77.6	12.6	80.1	12.7
TL201-22	67445	0	0.01212	0.00198	0.08240	0.01356	0.04930	0.00110	0.991	77.7	12.6	80.4	12.6
TL201-7	156655	0	0.01215	0.00198	0.08618	0.02164	0.05144	0.00984	0.648	77.9	12.6	83.9	20.0
TL201-37	135996	0	0.01215	0.00198	0.08451	0.01398	0.05043	0.00153	0.983	77.9	12.6	82.4	13.0
TL201-30	318901	206	0.01219	0.00198	0.08203	0.01352	0.04879	0.00144	0.984	78.1	12.6	80.0	12.6
TL201-24	152763	0	0.01221	0.00198	0.08613	0.04384	0.05118	0.02470	0.318	78.2	12.6	83.9	40.2
TL201-11	106467	135	0.01223	0.00198	0.08271	0.01680	0.04905	0.00603	0.796	78.4	12.6	80.7	15.6
TL201-33	44890	0	0.01223	0.00198	0.08235	0.02781	0.04883	0.01447	0.479	78.4	12.6	80.4	25.8
TL201-31	64284	0	0.01226	0.00198	0.09913	0.01679	0.05865	0.00303	0.952	78.5	12.6	96.0	15.4
TL201-53	40111	0	0.01227	0.00198	0.08163	0.02028	0.04826	0.00912	0.649	78.6	12.6	79.7	18.9
TL201-84	219569	139	0.01230	0.00198	0.08319	0.01390	0.04904	0.00223	0.962	78.8	12.6	81.1	13.0
TL201-15	67818	0	0.01231	0.00198	0.08660	0.03292	0.05103	0.01758	0.423	78.9	12.6	84.3	30.3
TL201-38	63037	0	0.01233	0.00198	0.08427	0.01437	0.04957	0.00286	0.941	79.0	12.6	82.2	13.4
TL201-8	25187	0	0.01234	0.00198	0.09342	0.04870	0.05489	0.02723	0.307	79.1	12.6	90.7	44.2
TL201-1	21487	0	0.01236	0.00198	0.08426	0.01372	0.04945	0.00149	0.983	79.2	12.6	82.1	12.8
TL201-13	175625	95	0.01236	0.00198	0.09186	0.01676	0.05391	0.00472	0.877	79.2	12.6	89.2	15.5
TL201-79	33154	0	0.01238	0.00198	0.10025	0.10786	0.05874	0.06250	0.149	79.3	12.6	97.0	95.0
TL201-100	175609	128	0.01241	0.00198	0.08960	0.02225	0.05236	0.00997	0.642	79.5	12.6	87.1	20.5
TL201-45	229176	125	0.01243	0.00198	0.08802	0.06924	0.05137	0.03957	0.202	79.6	12.6	85.7	62.6
TL201-74	48122	0	0.01244	0.00198	0.08871	0.01491	0.05171	0.00281	0.946	79.7	12.6	86.3	13.8
TL201-62	131172	0	0.01245	0.00198	0.08477	0.01845	0.04938	0.00735	0.730	79.8	12.6	82.6	17.1
TL201-98	186560	0	0.01251	0.00198	0.08431	0.01367	0.04889	0.00173	0.976	80.1	12.6	82.2	12.7
TL201-47	87979	0	0.01251	0.00198	0.08602	0.02169	0.04987	0.00979	0.627	80.1	12.6	83.8	20.1
TL201-101	75318	0	0.01252	0.00198	0.08463	0.01469	0.04904	0.00352	0.911	80.2	12.6	82.5	13.7
TL201-50	134326	0	0.01252	0.00198	0.08793	0.06470	0.05095	0.03661	0.215	80.2	12.6	85.6	58.7
TL201-73	106725	0	0.01254	0.00198	0.08576	0.05065	0.04959	0.02822	0.267	80.3	12.6	83.5	46.3
TL201-41	48137	0	0.01254	0.00198	0.09074	0.05562	0.05246	0.03108	0.257	80.4	12.6	88.2	50.5
TL201-6	230491	0	0.01257	0.00198	0.09099	0.08030	0.05251	0.04559	0.179	80.5	12.6	88.4	72.1
TL201-4	50813	0	0.01257	0.00198	0.08836	0.01600	0.05098	0.00455	0.870	80.5	12.6	86.0	14.8
TL201-87	258357	167	0.01258	0.00198	0.09124	0.03531	0.05260	0.01860	0.407	80.6	12.6	88.7	32.3
TL201-76	250150	169	0.01259	0.00198	0.09368	0.05406	0.05396	0.02996	0.272	80.7	12.6	90.9	49.0
TL201-9	298070	0	0.01259	0.00198	0.09166	0.01465	0.05279	0.00150	0.984	80.7	12.6	89.1	13.5

Table 2. U-Pb data of selected 66 zircons from sample TL201 (see text) cont'd.

TL201-72	26622	0	0.01260	0.00198	0.08205	0.02650	0.04723	0.01332	0.487	80.7	12.6	80.1	24.6
TL201-44	125608	130	0.01263	0.00198	0.08323	0.02256	0.04781	0.01057	0.578	80.9	12.6	81.2	20.9
TL201-71	19758	0	0.01264	0.00198	0.08562	0.01372	0.04913	0.00165	0.978	81.0	12.6	83.4	12.8
TL201-54	14717	0	0.01272	0.00198	0.08728	0.01372	0.04976	0.00111	0.990	81.5	12.6	85.0	12.7
TL201-48	13422	0	0.01276	0.00198	0.09131	0.09987	0.05190	0.05619	0.142	81.7	12.6	88.7	88.9
TL201-58	10525	0	0.01277	0.00198	0.08637	0.01365	0.04906	0.00149	0.981	81.8	12.6	84.1	12.7
TL201-46	75662	0	0.01279	0.00198	0.08883	0.05247	0.05036	0.02870	0.262	81.9	12.6	86.4	47.8
TL201-66	77857	0	0.01280	0.00198	0.08785	0.03025	0.04979	0.01532	0.450	82.0	12.6	85.5	27.9
TL201-52	54948	0	0.01281	0.00198	0.08704	0.03979	0.04929	0.02121	0.338	82.0	12.6	84.7	36.5
TL201-57	13943	0	0.01294	0.00198	0.08847	0.01574	0.04960	0.00448	0.861	82.9	12.6	86.1	14.6
TL201-23	7836	0	0.01296	0.00198	0.10270	0.02359	0.05745	0.00986	0.665	83.0	12.6	99.3	21.5
TL201-67	18321	0	0.01305	0.00198	0.11206	0.09252	0.06229	0.05056	0.184	83.6	12.6	107.8	81.1
TL201-60	16670	0	0.01305	0.00198	0.09400	0.05636	0.05222	0.03030	0.253	83.6	12.6	91.2	51.0
TL201-82	68226	0	0.01307	0.00198	0.09127	0.09019	0.05064	0.04945	0.153	83.7	12.6	88.7	80.6
TL201-81	27950	0	0.01309	0.00198	0.08675	0.05832	0.04808	0.03149	0.225	83.8	12.6	84.5	53.1
TL201-51	68875	0	0.01310	0.00198	0.08819	0.02417	0.04882	0.01116	0.552	83.9	12.6	85.8	22.3
TL201-19	80723	0	0.01314	0.00198	0.08971	0.01365	0.04951	0.00097	0.992	84.2	12.6	87.2	12.6
TL201-63	57103	0	0.01316	0.00198	0.09607	0.05013	0.05296	0.02646	0.289	84.3	12.6	93.1	45.4
TL201-36	21943	0	0.01340	0.00199	0.09677	0.02630	0.05240	0.01193	0.546	85.8	12.6	93.8	24.1
TL201-26	19434	0	0.01348	0.00199	0.11213	0.02595	0.06032	0.01074	0.639	86.3	12.7	107.9	23.4
TL201-61	31546	0	0.01376	0.00199	0.08923	0.03208	0.04702	0.01548	0.402	88.1	12.6	86.8	29.5
TL201-59	16119	0	0.01397	0.00199	0.13175	0.19684	0.06839	0.10171	0.095	89.4	12.6	125.7	162.8
TL201-43	23076	0	0.01478	0.00205	0.16272	0.06779	0.07986	0.03137	0.333	94.6	13.0	153.1	57.5
TL201-75	136048	147	0.01480	0.00199	0.27600	0.30555	0.13525	0.14861	0.122	94.7	12.7	247.5	218.0
TL201-55	93700	0	0.01485	0.00202	0.11149	0.09493	0.05447	0.04578	0.160	95.0	12.8	107.3	83.2

Table 3. U-Pb data for 70 selected zircons from sample TL202 (see text).

Grain ID	^{206}Pb cps	^{204}Pb cps	^{206}Pb/^{238}U	2σ error	^{207}Pb/^{235}U	2σ error	^{207}Pb/^{206}Pb	2σ error	rho	^{206}Pb/^{238}U AGE (Ma)	2σ error	^{207}Pb/^{235}U AGE (Ma)	2σ error
TL202-21	324795	38	0.01151	0.00130	0.07437	0.00844	0.04688	0.00063	0.993	73.8	8.3	72.8	7.9
TL202-18	153924	16	0.01151	0.00130	0.07774	0.00885	0.04897	0.00081	0.989	73.8	8.3	76.0	8.3
TL202-17	11409	0	0.01157	0.00130	0.07082	0.00806	0.04438	0.00085	0.986	74.2	8.3	69.5	7.6
TL202-16	74509	0	0.01167	0.00130	0.07478	0.00838	0.04646	0.00063	0.993	74.8	8.3	73.2	7.9
TL202-13	32976	0	0.01185	0.00130	0.07565	0.00837	0.04630	0.00066	0.992	75.9	8.3	74.0	7.9
TL202-81	328371	0	0.01186	0.00130	0.07832	0.00880	0.04789	0.00120	0.975	76.0	8.3	76.6	8.3
TL202-100	47266	0	0.01189	0.00130	0.07923	0.00960	0.04834	0.00252	0.903	76.2	8.3	77.4	9.0
TL202-22	45564	24	0.01193	0.00130	0.07554	0.00983	0.04590	0.00326	0.837	76.5	8.3	73.9	9.2
TL202-34	72082	0	0.01194	0.00130	0.07861	0.00990	0.04775	0.00302	0.865	76.5	8.3	76.8	9.3
TL202-9	122640	0	0.01200	0.00130	0.07699	0.00844	0.04652	0.00074	0.989	76.9	8.3	75.3	7.9
TL202-75	308314	0	0.01200	0.00130	0.07887	0.01207	0.04765	0.00515	0.708	76.9	8.3	77.1	11.3
TL202-36	25915	0	0.01202	0.00130	0.07487	0.02189	0.04519	0.01227	0.371	77.0	8.3	73.3	20.5
TL202-44	116261	0	0.01204	0.00130	0.07594	0.01298	0.04576	0.00606	0.633	77.1	8.3	74.3	12.2
TL202-27	142000	0	0.01204	0.00130	0.07496	0.00819	0.04515	0.00070	0.990	77.2	8.3	73.4	7.7
TL202-23	196567	10	0.01204	0.00130	0.07703	0.00839	0.04639	0.00064	0.992	77.2	8.3	75.3	7.9
TL202-82	180280	0	0.01205	0.00130	0.08001	0.00905	0.04814	0.00162	0.954	77.2	8.3	78.2	8.5
TL202-35	63117	0	0.01206	0.00130	0.07617	0.01316	0.04580	0.00618	0.625	77.3	8.3	74.5	12.3
TL202-8	566193	102	0.01207	0.00131	0.09097	0.01297	0.05466	0.00508	0.759	77.4	8.3	88.4	12.0
TL202-32	73375	0	0.01213	0.00130	0.07776	0.01027	0.04650	0.00357	0.814	77.7	8.3	76.0	9.6
TL202-61	482771	0	0.01214	0.00130	0.07999	0.02091	0.04777	0.01139	0.410	77.8	8.3	78.1	19.5
TL202-60	307895	0	0.01215	0.00130	0.07967	0.00953	0.04754	0.00253	0.895	77.9	8.3	77.8	8.9
TL202-69	122904	0	0.01218	0.00130	0.07999	0.00883	0.04765	0.00129	0.969	78.0	8.3	78.1	8.3
TL202-47	184171	0	0.01218	0.00130	0.08437	0.19838	0.05023	0.11798	0.045	78.1	8.3	82.2	170.6
TL202-42	130706	0	0.01221	0.00130	0.07990	0.02728	0.04746	0.01540	0.313	78.2	8.3	78.0	25.3
TL202-12	193748	0	0.01222	0.00130	0.06809	0.00739	0.04040	0.00081	0.983	78.3	8.3	66.9	7.0
TL202-103	238966	0	0.01226	0.00130	0.08193	0.00888	0.04847	0.00102	0.981	78.6	8.3	80.0	8.3
TL202-68	83056	0	0.01226	0.00130	0.08011	0.00987	0.04739	0.00295	0.863	78.6	8.3	78.3	9.2
TL202-30	95644	0	0.01226	0.00130	0.07631	0.00824	0.04514	0.00082	0.986	78.6	8.3	74.7	7.7
TL202-93	489769	26	0.01227	0.00130	0.08125	0.04736	0.04801	0.02751	0.182	78.6	8.3	79.3	43.5
TL202-97	100648	0	0.01228	0.00130	0.08080	0.01539	0.04773	0.00755	0.558	78.7	8.3	78.9	14.4
TL202-37	280231	0	0.01228	0.00130	0.06944	0.01199	0.04102	0.00558	0.615	78.7	8.3	68.2	11.3
TL202-43	68647	0	0.01229	0.00130	0.07910	0.00858	0.04670	0.00104	0.979	78.7	8.3	77.3	8.0
TL202-7	327959	11	0.01229	0.00130	0.08697	0.00966	0.05133	0.00168	0.956	78.7	8.3	84.7	9.0
TL202-70	146153	0	0.01230	0.00130	0.08079	0.01401	0.04764	0.00654	0.611	78.8	8.3	78.9	13.1
TL202-2	137311	0	0.01231	0.00130	0.07783	0.00832	0.04587	0.00067	0.991	78.8	8.3	76.1	7.8
TL202-39	118393	0	0.01232	0.00130	0.07958	0.02716	0.04683	0.01519	0.310	79.0	8.3	77.7	25.2
TL202-1	42473	0	0.01234	0.00130	0.07875	0.00839	0.04628	0.00065	0.991	79.1	8.3	77.0	7.9
TL202-71	142499	10	0.01237	0.00130	0.08146	0.00876	0.04776	0.00099	0.981	79.3	8.3	79.5	8.2
TL202-10	155280	0	0.01240	0.00131	0.07961	0.01207	0.04657	0.00508	0.695	79.4	8.3	77.8	11.3
TL202-28	417679	36	0.01243	0.00131	0.07819	0.00833	0.04564	0.00083	0.985	79.6	8.3	76.4	7.8
TL202-67	129689	0	0.01246	0.00131	0.08165	0.00882	0.04752	0.00125	0.970	79.8	8.3	79.7	8.2

Table 3. U-Pb data for 70 selected zircons from sample TL202 (see text) cont'd.

TL202-91	102206	0	0.01250	0.00131	0.08345	0.03875	0.04841	0.02190	0.225	80.1	8.3	81.4	35.7
TL202-5	216785	0	0.01257	0.00131	0.07733	0.00813	0.04463	0.00072	0.988	80.5	8.3	75.6	7.6
TL202-86	153513	0	0.01259	0.00131	0.08300	0.00943	0.04782	0.00221	0.914	80.6	8.3	81.0	8.8
TL202-102	55686	0	0.01263	0.00131	0.09315	0.11133	0.05348	0.06368	0.087	80.9	8.3	90.4	98.5
TL202-87	880092	74	0.01265	0.00131	0.08479	0.05219	0.04862	0.02950	0.168	81.0	8.3	82.6	47.7
TL202-96	34868	0	0.01265	0.00131	0.08498	0.00927	0.04871	0.00171	0.947	81.1	8.3	82.8	8.6
TL202-104	18876	0	0.01268	0.00131	0.08707	0.03043	0.04980	0.01663	0.295	81.2	8.3	84.8	28.0
TL202-72	195192	98	0.01269	0.00131	0.08334	0.02148	0.04764	0.01125	0.400	81.3	8.3	81.3	19.9
TL202-94	151973	0	0.01270	0.00131	0.09507	0.05364	0.05431	0.03013	0.182	81.3	8.3	92.2	48.6
TL202-41	1086144	170	0.01271	0.00131	0.08078	0.04642	0.04611	0.02607	0.179	81.4	8.3	78.9	42.7
TL202-4	87904	0	0.01273	0.00131	0.08195	0.00853	0.04670	0.00080	0.987	81.5	8.3	80.0	8.0
TL202-92	50897	0	0.01274	0.00131	0.08392	0.00880	0.04776	0.00103	0.979	81.6	8.3	81.8	8.2
TL202-88	74334	0	0.01278	0.00131	0.08526	0.01940	0.04837	0.00983	0.450	81.9	8.3	83.1	18.0
TL202-3	80294	0	0.01281	0.00131	0.08356	0.14093	0.04733	0.07967	0.061	82.0	8.3	81.5	124.2
TL202-48	420772	0	0.01282	0.00131	0.09257	0.12720	0.05237	0.07175	0.074	82.1	8.3	89.9	111.8
TL202-99	313403	0	0.01282	0.00131	0.08641	0.16356	0.04888	0.09238	0.054	82.1	8.3	84.2	142.4
TL202-55	36594	0	0.01285	0.00131	0.09301	0.01082	0.05250	0.00294	0.876	82.3	8.3	90.3	10.0
TL202-66	86529	0	0.01286	0.00131	0.08220	0.00957	0.04635	0.00262	0.874	82.4	8.3	80.2	8.9
TL202-65	158532	0	0.01293	0.00131	0.08338	0.01735	0.04675	0.00850	0.487	82.8	8.3	81.3	16.1
TL202-45	181370	0	0.01342	0.00131	0.07349	0.16933	0.03971	0.09140	0.043	86.0	8.4	72.0	148.7
TL202-76	303627	105	0.01351	0.00132	0.09252	0.02583	0.04968	0.01299	0.351	86.5	8.4	89.8	23.7
TL202-54	141307	0	0.01352	0.00132	0.08999	0.00887	0.04826	0.00071	0.989	86.6	8.4	87.5	8.2
TL202-20	277036	134	0.01366	0.00132	0.08996	0.00876	0.04777	0.00066	0.990	87.5	8.4	87.5	8.1
TL202-83	45479	0	0.01372	0.00132	0.09117	0.00962	0.04821	0.00206	0.915	87.8	8.4	88.6	8.9
TL202-53	40182	0	0.01383	0.00132	0.09360	0.02691	0.04909	0.01332	0.332	88.5	8.4	90.9	24.7
TL202-38	120539	0	0.01416	0.00138	0.12327	0.01404	0.06315	0.00370	0.857	90.6	8.8	118.0	12.6
TL202-59	159551	0	0.01426	0.00132	0.09379	0.01324	0.04770	0.00508	0.656	91.3	8.4	91.0	12.2
TL202-52	194908	0	0.01448	0.00133	0.09654	0.01044	0.04835	0.00276	0.850	92.7	8.4	93.6	9.6
TL202-63	87893	0	0.01482	0.00134	0.11375	0.02320	0.05566	0.01017	0.444	94.8	8.5	109.4	20.9

These ^{206}Pb/^{238}U ages are in excellent agreement with each other and with the timing of Mo mineralization as obtained from Re–Os molybdenite geochronology.

Ar–Ar Geochronology Results (Data Pending)

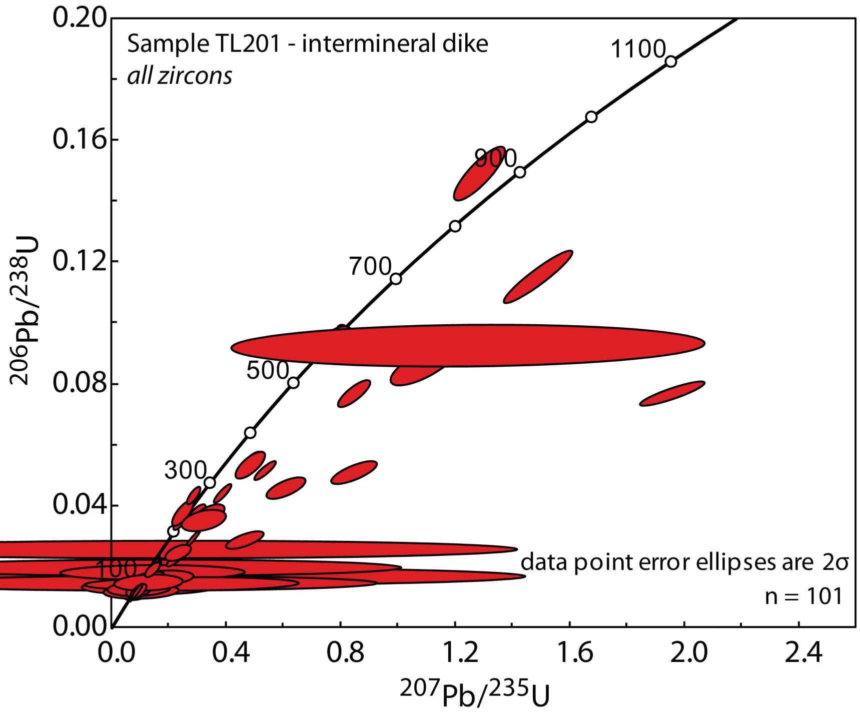

Figure 31. Concordia diagram for all zircons from sample TL201 showing significant inheritance in many grains, but a concentration of data near a lower intercept with concordia.

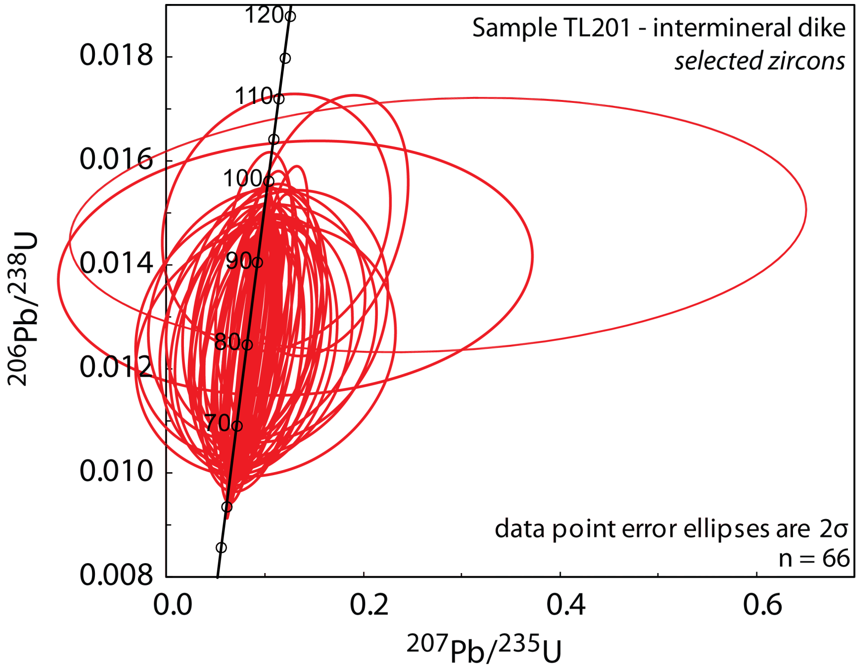

Figure 32. Concordia diagram for selected zircons from sample TL201. A weighted average of ^{206}Pb/^{238}U ages for this zircon population is 80.9 ± 1.6 Ma with a MSWD = 0.43.

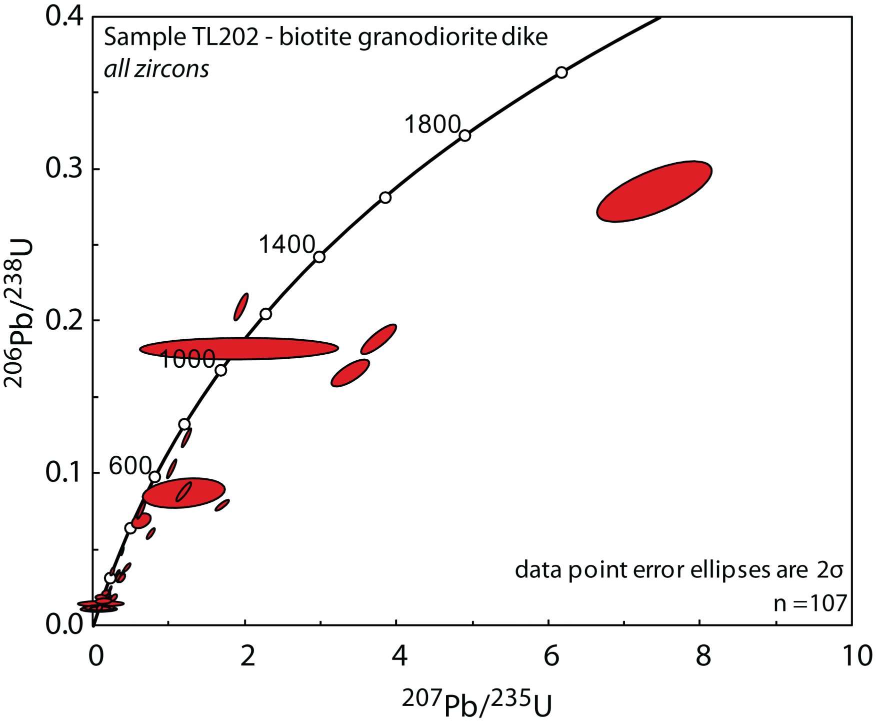

Figure 33. Concordia diagram for all zircons from sample TL202 showing significant inheritance in many grains, but a concentration of data near a lower intercept with concordia.

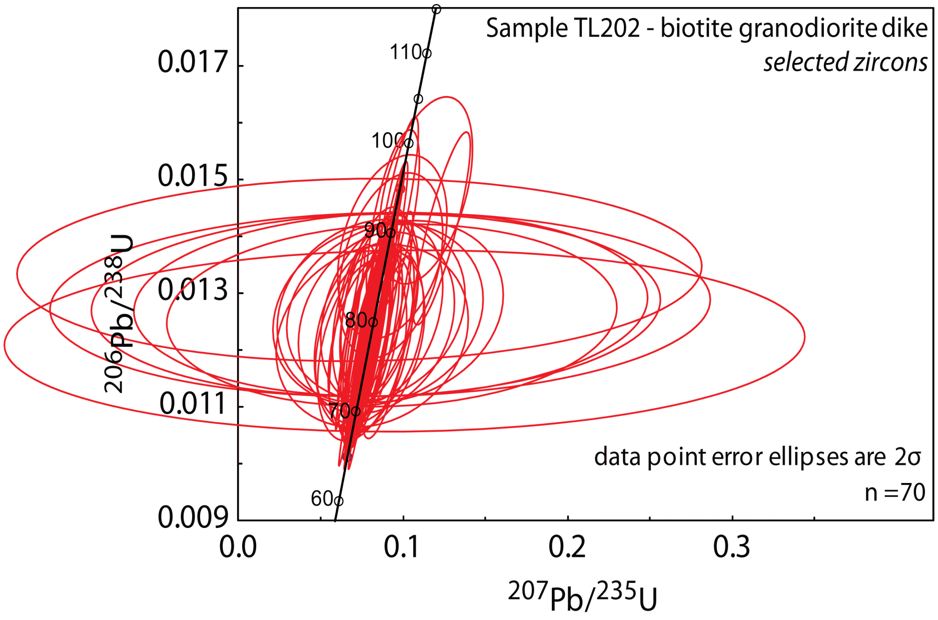

Figure 34. Concordia diagram for selected zircons from sample TL202. A weighted average of ^{206}Pb/^{238}U age for this zircon population is 80.2 ± 1.0 Ma with a MSWD = 1.05)

2.5.3 Fluid Inclusion Results

Previous Work

Linnen and Williams-Jones (1990) provide a detailed account of the different fluid inclusion populations at MAX. These authors collected samples from each of the dominant alteration assemblages and identified two compositional fluid inclusion types. Type 1 inclusions are liquid-rich aqueous inclusions that are most abundant in potassically altered samples. Type 2 inclusions are aqueous-carbonic inclusions that are most commonly associated with late propylitic alteration. Type 1 inclusions from the various alteration assemblages possess relatively uniform salinities (mode at ~8 wt.% NaCl equivalent) and homogenization temperatures (170°C to 310°C). Type 2 inclusions possess range to higher homogenization temperatures than type 1 inclusions (240° to 340°C; Linnen and Williams-Jones, 1990). The association of aqueous-carbonic inclusions with late propylitic alteration led Linnen and Williams-Jones (1990) to suggest that the hydrothermal system evolved to become increasingly carbonic.

Objectives

Recent drilling targeted areas adjacent to the MAX high-grade zone and intersected numerous Pb-Zn-Ag-bearing veins. These veins are typically <30 cm thick and are almost exclusively associated with muscovite-calcite-epidote-pyrite alteration that is identical in mineralogy to late propylitic alteration at MAX (Fig. 23). The distribution, grade, size, and metal association of these veins are identical to those described at the adjacent Lucky Boy and Copper Chief mines. These observations led Linnen and Williams-Jones (1987) to suggest that the peripheral Pb-Zn-Ag showings may be genetically related to the MAX. A fluid inclusion study was undertaken here to determine if the hydrothermal fluids carrying Pb-Zn-Ag mineralization shared any similarities with the hydrothermal system at MAX. Mineralized veins from each of the paragenetic vein sets were sampled to identify the fluid evolution of the system.

Results

The two compositional fluid inclusion types identified in this study are similar to those reported by Linnen and Williams-Jones (1990): aqueous liquid-rich fluid inclusions (type 1) and, aqueous-carbonic liquid-rich fluid inclusions (type 2). Both fluid inclusion types are present in all veins; however, carbonic-rich fluid inclusions are more abundant in late veins. Many type 2 inclusions do not possess sufficient CO_2 to form a separate liquid CO_2 phase at room temperature. In these cases, CO_2 is inferred from observed clathrate formation/melting.

Fluid inclusions from all veins are typically <5 µm long and the majority are localized along fracture planes that crosscut quartz grain boundaries (Fig. 35). These fluid inclusions are classified as secondary using the temporal classification scheme of Roedder (1984) and were not measured because they do not provide information that would answer the study's objectives. Primary or pseudo-secondary fluid inclusions >5 µm were sought for use in this study. Fluid inclusions >20 µm typically showed evidence of necking, leaking, and irregular fluid inclusions shapes. These inclusions were rejected because they do not represent isoplethic and isochoric systems as required for microthermometry.

Clusters of fluid inclusions with variable liquid–vapour ratios are interpreted to be the result of necking down and were also not used in this study. No genuinely vapour-rich fluid inclusions that might represent a trapped vapour phase were recognized in this study. Cuspate–lobate quartz grain boundaries are ubiquitous and interpreted to represent areas of recrystallization. Fluid inclusions within areas of recrystallization were avoided for this study.

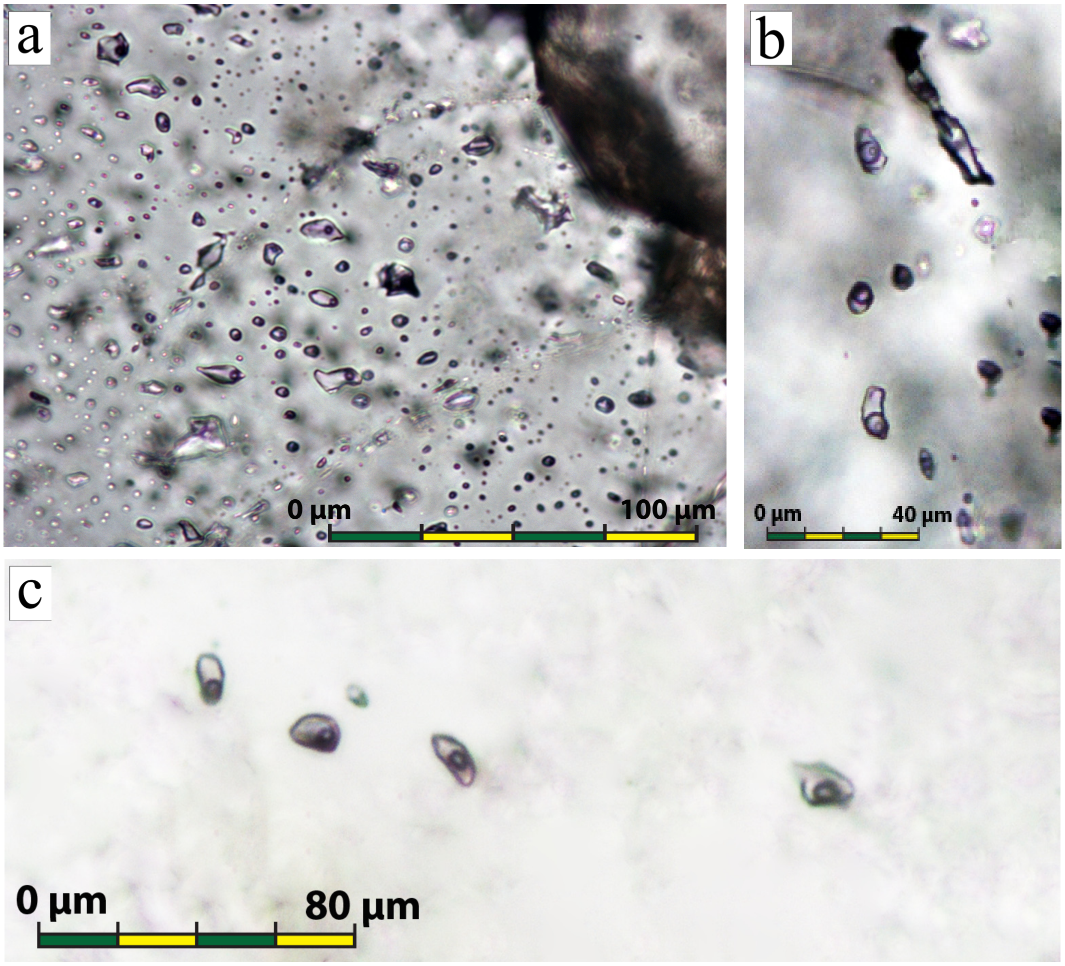

Figure 35. Transmitted light photomicrographs of: (a) an array of secondary fluid inclusions; (b) secondary type 2 aqueous-carbonic inclusions; (c) primary type 1 aqueous inclusions.

Pseudosecondary and primary inclusions were targeted for this study because they represent the best proxy for the P-T-X conditions of Mo- and Pb-Zn-Ag-bearing fluids. Primary inclusions ranged in size from 5 to 15µm and typically occurred in similarly oriented clusters with similar liquid–vapour ratios (Fig. 35). The orientation of these inclusion groups was interpreted to represent growth perpendicular to quartz growth zones. These inclusions are most easily detected at low magnification (20x) as small and distinct zones away from obvious secondary inclusions. Liquid–vapour ratios of these inclusions ranged from 80 to 95% liquid.

Pseudosecondary inclusions are the second most abundant temporal fluid inclusion type. These inclusions were most easily observed in areas of low fluid inclusion density at low magnification (20x). Inclusions typically formed along planes that terminated within quartz grains.

Fluid inclusion results are summarized in Table 4. Degree of fill refers to the volume % of the H_2O liquid phase relative to the other phases present.

Mo veins

Type 1 inclusions typically homogenized to the liquid phase by vapour bubble shrinkage. The homogenization temperatures of type 1 inclusions possess a weak bi-modal distribution with means of 221°C ± 2°C (n = 24) and 303° ± 25°C (n = 63). Homogenization temperatures of type 2 inclusions possess a left-skewed distribution with a mean of 296° ± 31°C (n = 86). Early and late Mo-bearing veins possess an identical range of Th and show no systematic change in homogenization temperatures.

Initial melting temperatures of type 1 inclusions are very similar to the H_2O-NaCl eutectic (i.e., -21.2°C) and suggests that this inclusion type can be approximated by the H_2O-NaCl system. Using the freezing-point depression of type 1 inclusions and the equation of Bodnar (1993), salinity was calculated for Mo veins from all paragenetic vein sets. Mo-vein salinities possess a slightly bi-modal distribution with a means of 5.0 ± 1.1 wt.% NaCl equivalent (n = 55) and 9.4 ± 1.0 wt.% NaCl equivalent (n = 28; Fig. 36). Type 1 inclusions, from early and late Mo-bearing veins, exhibit no systematic change in salinity.

Table 4. Fluid inclusion summary table.

		Type 1 (n=87)	**Type 2 (n=86)**			**Type 1 (n=45)**	**Type 2 (n=103)**
Mo Veins	degree of fill %	70 to 95	50 to 95	**Ag-Pb-Zn Veins**	degree of fill %	70 to 95	50 to 95
	Tm_{CO_2} °C	-	-62.4 to -54.7		Tm_{CO_2} °C	-	-64.3 to -54.0
	average	-	*-57.2*		*average*	-	*-57.0*
	Te °C	-20 to -5			Te °C	-20 to -5	
	Tm_{ice} °C	-1.1 to -5.7	-		Tm_{ice} °C	-0.7 to -5.7	-
	average	*-3.3*	-		*average*	*-3.2*	-
	Salinity[1] wt.% NaCl equiv.	2.0 to 11.7	-		Salinity[1] wt.% NaCl equiv.	1.3 to 11.7	-
	average	*5.0 and 9.4*	-		*average*	*4.1 and 8.5*	-
	Tm_{Clath} °C	-	4.3 to 13.0		Tm_{Clath} °C	-	5.9 to 14.4
	average	-	*8.6*		*average*	-	*8.3*
	Salinity[2] wt.% NaCl equiv.	-	0.4 to 10.0		Salinity[2] wt.% NaCl equiv.	-	1.0 to 7.6
	average	-	*3.4*		*average*	-	*3.7*
	$Th_{CO_2\ L\text{-}V(L)}$ °C	-	15.7 to 28.1		$Th_{CO_2\ L\text{-}V(L)}$ °C	-	9.2 to 29.0
	average	-	*20.3*		*average*	-	*21.4*
	$Th_{total\ (L)}$ °C	166 to 348	213 to 344		$Th_{total\ (L)}$ °C	169 to 302	178 to 330
	average	*221 and 303*	*296*		*average*	*225*	*241 and 305*
	Tt °C	276 to 508			Tt °C	279 to 462	
	X_{CO_2} *average*		*0.08*		X_{CO_2} *average*		*0.08*

[1] Salinity for type 1 inclusions are calculated from the equation of Bodnar (1993)
[2] Salinity for type 2 inclusions are caculated from the equation of Bozzo et al. (1975)

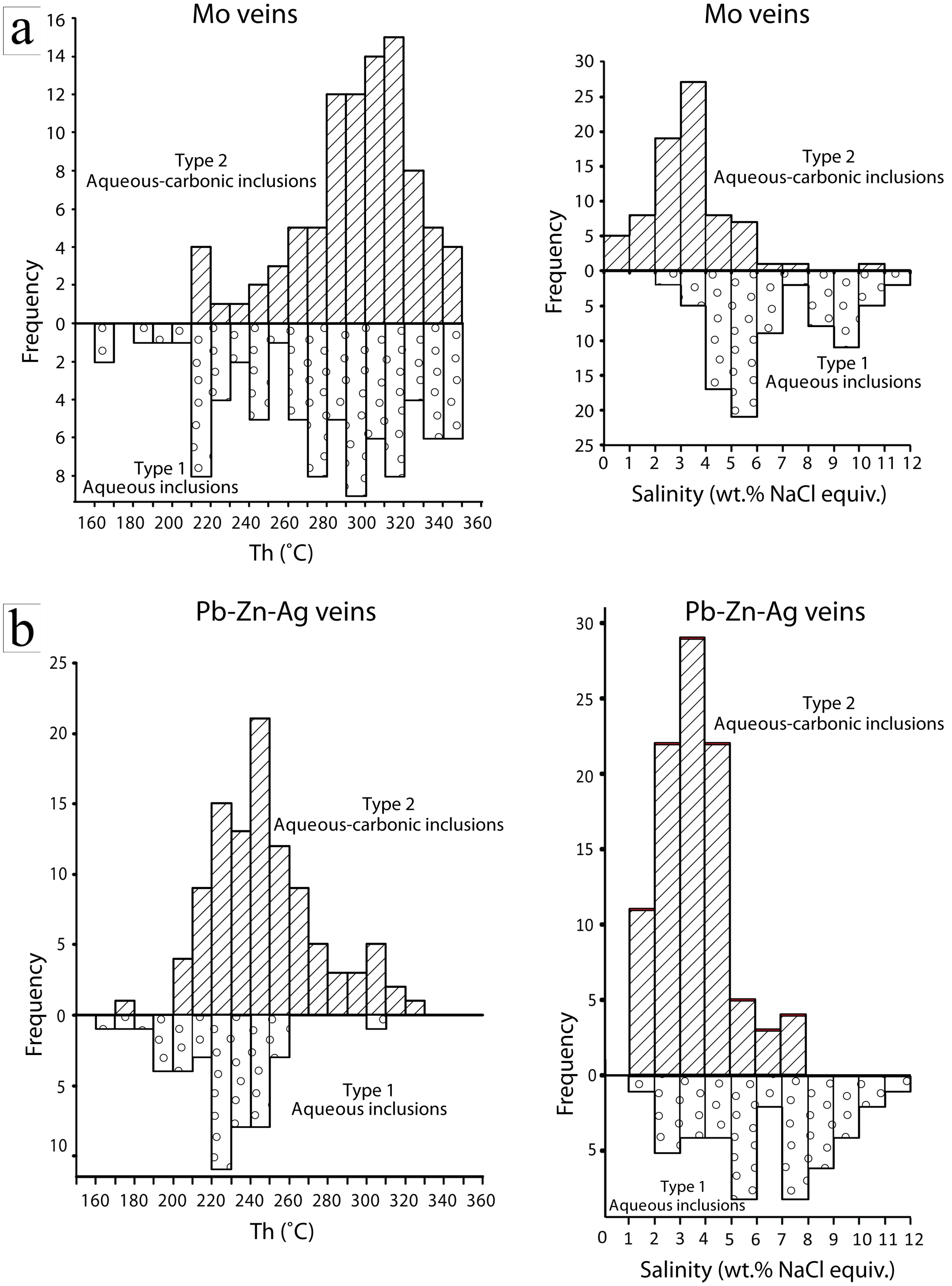

Figure 36. (a) Histograms showing homogenization temperature and salinity distribution for type 1 and 2 inclusions from Mo-bearing veins; (b) histograms showing homogenization temperature and salinity distribution for type 1 and 2 inclusions from Pb-Zn-Ag-bearing veins.

CO_2 melting temperatures for type 2 inclusions averaged -57.2°C ± 1.6°C (n = 43). This value is close to the CO_2 eutectic (i.e., -56.6°C) and suggests that type 2 inclusions contain relatively pure CO_2. Samson (1985) confirmed the presence of minor gaseous CH_4 (most X_{CH_4} between 0.0 and 0.05) in MAX hydrothermal fluids by Raman spectroscopy. No other volatile species were identified. Minor amounts of CH_4 could explain the depressed CO_2 melting temperatures observed in some type 2 inclusions. Rare inclusions with clathrate melting temperatures greater than 10°C also indicate that type 2 inclusions do not represent a pure H_2O-CO_2-NaCl system. CH_4, hydrocarbons, and/or other species all cause clathrate to melt at temperatures in excess of 10°C (Collins, 1979). Because CO_2 and H_2O in the majority of type 2 inclusions melt at temperatures near the H_2O-CO_2 and H_2O-NaCl respective eutectics, type 2 inclusions can be approximated by the H_2O-CO_2-NaCl system. Using the final melting temperature of clathrate, and the equation of Bozzo et al. (1975), salinities were calculated for type 2 inclusions from all paragenetic vein sets. Salinity for type 2 inclusions possess a normal distribution with a mean of 3.4 ± 1.6 wt.% NaCl equivalent (n = 77; Fig. 36). This corresponds to clathrate melting temperatures ranging from 4°C to 10°C. Clathrate melting temperatures translate to minimum estimations of salinity as a result of minor amounts of methane. Type 2 inclusions, from early and late Mo-bearing veins, exhibit no systematic change in salinity. Liquid and vapor CO_2 homogenized to the liquid phase over a range of temperatures for all Mo veins (15° to 29°C).

Pb-Zn-Ag Veins

Homogenization temperatures of type 1 inclusions from Pb-Zn-Ag veins possess a left-skewed distribution with a mean of 225°C ± 24°C (n = 45), whereas type 2 inclusions possess a weakly bi-modal distribution with means of 241˚C ± 20°C (n = 29) and 305°C ± 12°C (n = 74). Salinity for type 1 and 2 inclusions were calculated as above. Salinities of type 1 inclusions show a weak bi-modal distribution with means of 4.1 ± 1.4 wt.% NaCl equivalent (n = 23) and 8.5 ± 1.3 wt.% NaCl equivalent (n = 22). This corresponds to ice melting temperatures ranging from 0° to -5.7°C. Salinities of type 2 inclusions show a slightly right-skewed distribution with a mean of 3.7 ± 1.5 wt.% NaCl equivalent (n = 96). This corresponds to clathrate melting temperatures of 5.9° to 10°C. Clathrate melting temperatures translate to minimum estimations of salinity as a result of minor amounts of methane. Gaseous CO_2 homogenizes to liquid CO_2 over a wide range of temperatures (9° to 29°C).

Summary

Type 1 and 2 inclusions from Mo- and Pb-Zn-Ag-bearing veins possess similar ranges in homogenization temperature but different means (Fig. 37). Average $Th_{total(L)}$ for type 1 and 2 inclusions from Mo veins = 288° ± 39°C (n = 173), whereas average $Th_{total(L)}$ for type 1 and 2 inclusion from Pb-Zn-Ag veins = 242° ± 29°C (n = 148). The salinity of type 1 and 2 inclusions from both vein types show identical bi-modal distributions. Average salinity for type 1 and 2 inclusions from Mo veins = 3.8 ± 1.4 wt.% NaCl equivalent (n = 121) and 8.8 ± 1.4 wt. % NaCl equivalent (n = 38), whereas average salinity for type 1 and

2 inclusions from Pb-Zn-Ag veins = 3.6 ± 1.2 wt.% NaCl equivalent (n = 113) and 8.3 ± 1.3 wt.% NaCl equivalent (n = 28). The salinities of type 2 inclusions from both vein types are minimum estimates owing to minor concentrations of methane.

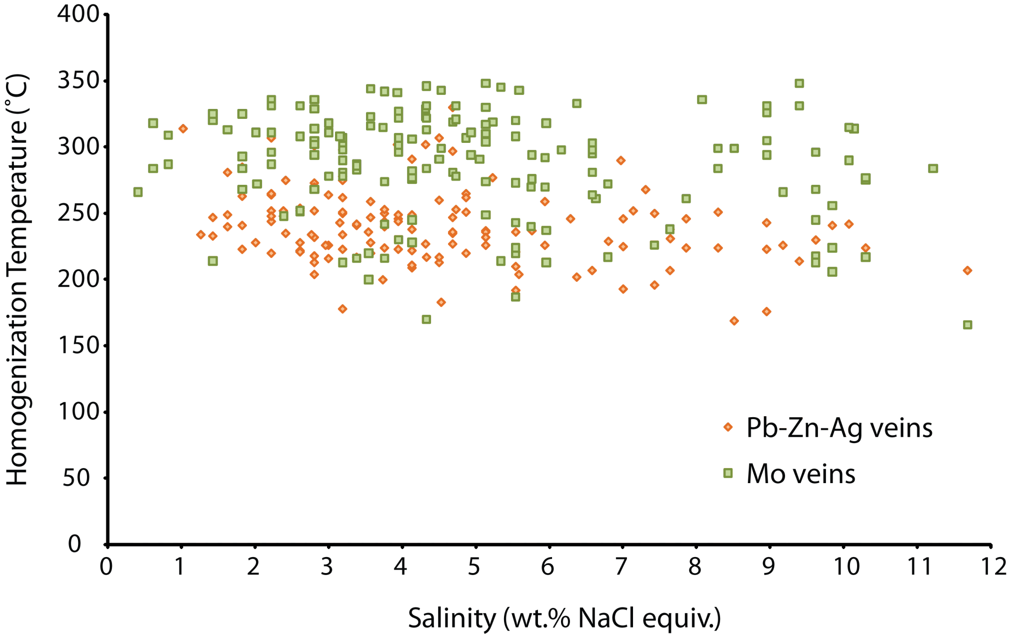

Figure 37. Scatter plot of fluid inclusion homogenization temperatures vs. salinity for Mo- and Pb-Zn-Ag-bearing veins.

3.0 Discussion

3.1 Lithogeochemistry Discussion

Lithogeochemistry is often used to classify igneous rocks according to widely recognized suites and tectonic settings (White and Chappell, 1977; Brown et al., 1984; Pearce et al., 1984). MAX intrusive phases are typical of the calc-alkaline suite, as shown by plotting MAX phases on granite discrimination diagrams. MAX intrusive phases mostly plot in the volcanic arc field of Pearce et al. (1984) based on the relative concentrations of Yb and Ta (Fig. 38). Brown et al. (1984) also linked granitic trace element chemistry to specific tectonic environments. This classification uses the concentration of high field strength elements (Nb, Ta, Hf, and Y) relative to the concentration of large ion lithophile elements (K, Rb, Th, U, and LREE) to distinguish primitive-, normal-, mature-, and back-arc settings. Potassically altered samples of the Trout Lake stock contain excess K and Rb and spuriously suggest a mature tectonic association. Least altered samples of the Trout Lake stock belong to the normal arc setting because of high concentrations of U, K, and LREE relative to Nb, Ta, Hf, Y, and Ti.

Granitic rocks can also be discriminated based on the I- and S-type classification of White and Chappell (1977). This classification stems from the

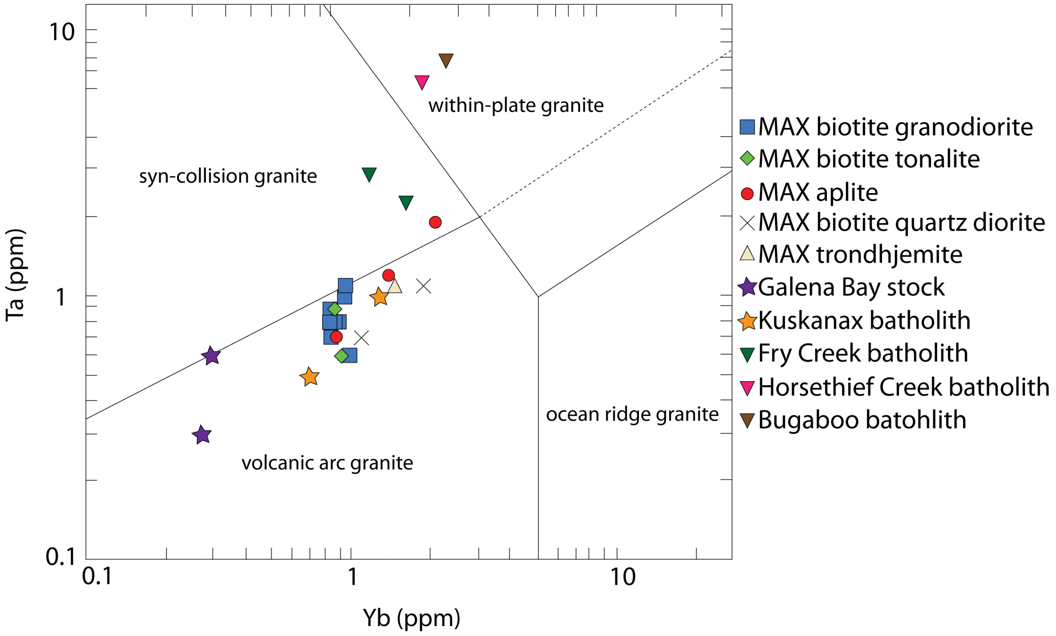

Figure 38. Granite discrimination diagram (Pearce et al., 1984) showing the tectonic affinity of Jurassic–Cretaceous intrusions in southeast British Columbia. Data for Fry Creek, Horsethief, and Bugaboo batholiths were compiled from Brandon and Lambert (1993).

observation that granitic melt chemistry is strongly controlled by the composition of its source. S-type granites are genetically related to partial melts of sedimentary sources that are enriched with respect to Al_2O_3 and depleted in Na_2O and K_2O. I-type granites are genetically related to partial melting of an igneous or "primitive" source and are characterized by low Al_2O_3 and relatively high Na_2O and K_2O contents. Compositional variations between the two source regions ultimately reflects the effects of surficial weathering undergone by sedimentary rocks. The chemical characteristics that define I- and S-type granites reflects the source material composition. Least-altered samples of the Trout Lake stock belong to the I-type granite class because of a moderate concentration of SiO_2 (i.e., 67–73%) , low K_2O/Na_2O ratios (i.e., 0.7–1.3), and low concentrations of Cr and Ni (White and Chappell, 1983). Least-altered samples were used to limit the effects of hydrothermal alteration on major element chemistry. I-type granites are synonymous with an arc environment.

The molecular ratio of Al_2O_3 / (K_2O + Na_2O+ CaO) is known as the alumina saturation index and is a common method of classifying igneous rocks. Least-altered intrusive rocks from MAX are weakly peraluminous (1.00–1.22). Partial to complete replacement of feldspars with hydrothermal muscovite would increase the Al content at the expense of Na_2O + CaO. Because all MAX intrusive phases exhibit some degree of replacement of feldspars with secondary muscovite, it is likely that the peraluminous association of these dikes is a result of hydrothermal alteration.

The REE distribution of MAX intrusive phases is typical of granitoids

(Haskin et al., 1966). LREE elements are typically enriched relative to the HREE and all the REE are enriched relative to chondrite. These features result in gently- to steeply-dipping patterns when plotted on normalized REE diagrams. All MAX phases possess such gently–dipping REE patterns. Several authors have studied the REE concentrations of igneous phases that host porphyry Mo mineralization in the USA (Gunow, 1983; Stein and Crock, 1990). These authors suggested that Mo-bearing intrusions are typically enriched in REE and are extremely differentiated as a result of fractional crystallization. MAX intrusive phases possess very similar REE patterns to other granodiorite-hosted deposits in the USA, but differ from the more fractionated pattern of "Climax-type" (see below) porphyry Mo deposits in Colorado (Figs. 39 and 40). The high LREE/HREE and lack of significant Eu anomalies in granodiorite dikes at MAX is consistent with a source that contains residual garnet and fractionating or minimal residual plagioclase. Minor Eu anomalies exhibited by late-magmatic phases are consistent with removal of plagioclase during crystallization.

3.2 Porphyry Mo Deposit Classification

Porphyry Mo deposits have been classified in a number of ways. Lithogeochemical data from the present study now allows the MAX to be placed within these widely-accepted classification schemes. Sutherland and Brown (1969) and Clark (1972) classified porphyry Mo deposits based on the approximate depth of emplacement and the relative complexity of structural and igneous features. This classification is inadequate because it is based on subjective

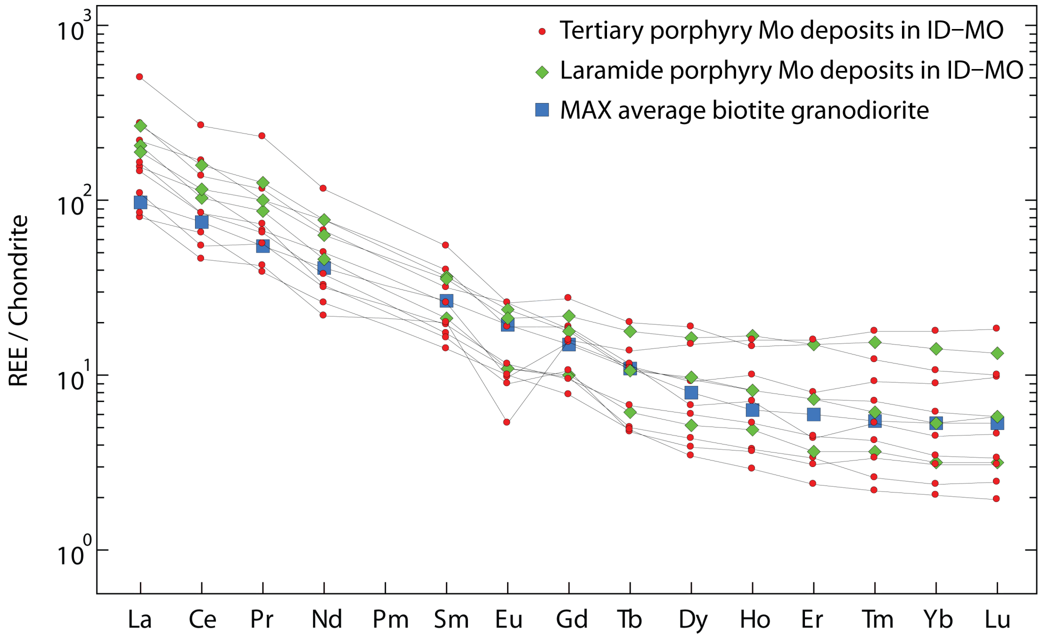

Figure 39. REE profile comparing MAX and other porphyry Mo deposits in the Idaho–Montana (ID–MO) porphyry belt. REE normalized to the Cl chondrite values of Sun and McDonough (1989). Data for Idaho–Montana porphyry deposits were compiled from Taylor et al. (2007).

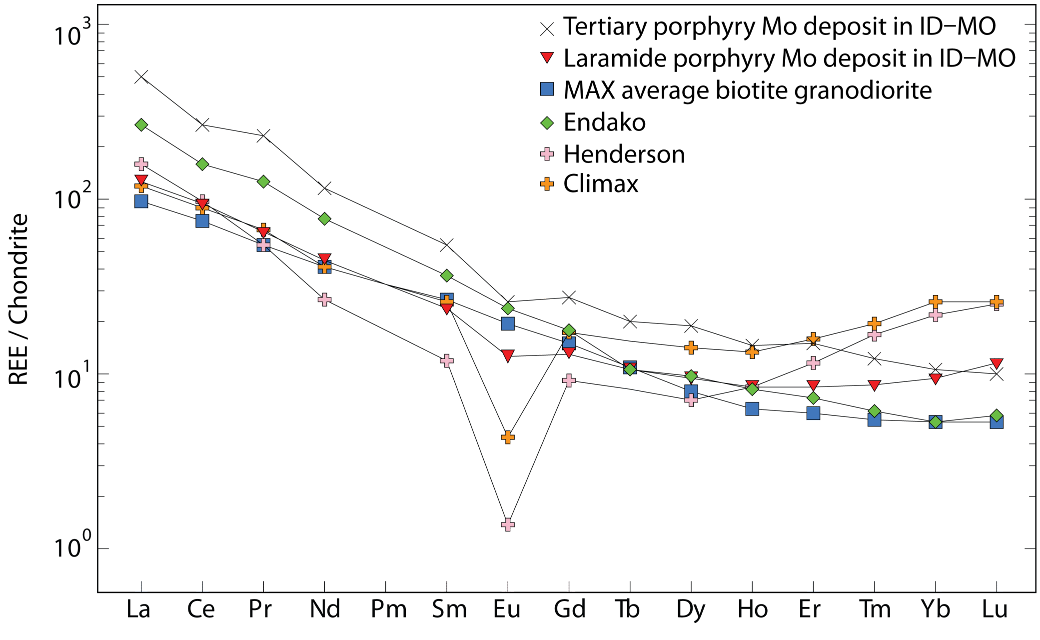

Figure 40. REE profiles comparing MAX and other porphyry Mo deposits. REE normalized to Cl chondrite values of Sun and McDonough (1989). Data for Idaho–Montana porphyry deposits were compiled from Taylor et al., (2007); data for Endako were compiled from Whalen et al. (2001); data for Henderson and Climax were compiled from Stein and Crock (1990).

arguments.

Sillitoe (1980) divided porphyry Mo deposits into two types based on their tectonic setting: arc-related deposits are typically smaller and possess lower Mo grades (i.e., <0.15% Mo) compared to rift-related deposits (i.e., >0.15% Mo). World class deposits such as Climax and Henderson (Colorado, USA) fall into the rift-related category. The primary advantage of this classification is to focus exploration efforts for particular deposit types based on tectonic setting. A major disadvantage is that ancient tectonic settings are often subject to debate. MAX intrusive phases possess a strong arc signature (i.e., Ta, Nb, and Ti depletions) and the Trout Lake stock can be spatially and temporally linked to arc magmatism in the Canadian Cordillera (see below). The high-grade zone at MAX is only one part of a much larger and lower-grade resource, which is consistent with the arc-type classification

Other porphyry Mo classification schemes divide deposits based on their host-rock characteristics (e.g., Mutschler et al., 1981). Granodiorite-type deposits are typically smaller and lower grade than the granite-type deposits. A similar classification scheme was proposed by White et al. (1981). In this scheme, porphyry Mo deposits are divided into two types: (1) Climax (granite) type; and (2) quartz monzonite type. An unfortunate complication inherent in these classifications is that rock naming schemes have changed through time. For example, the “granodiorite type” of Mustchler et al. (1981) includes rocks ranging in composition from granodiorite to granite according to the International Union of Geological Sciences classification scheme (Le Maitre, 2002). However, one advantage of this classification scheme is that clear differences in age, tectonic association, trace element concentrations, and ore body characteristics are evident when porphyry Mo deposits are divided according to host-rock petrology. Biotite granodiorite is the main intrusive phase at MAX and hosts the majority of mineralization. This corresponds to the granodiorite type deposits of Mutschler (1981), the quartz monzonite type deposits of White et al. (1981), and the quartz monzonitic–granitic porphyry type of Seedorff et al. (2005).

The apparent relationship between magma chemistry and metallogeny led Westra and Keith (1981) to divide porphyry Mo deposits into three major magma series based on the source intrusion's trace and major element chemistry. Keith (1978) modified the alkali-lime index of Peacock (1931) to define a magma series by its range of K_2O values at 57.5% SiO_2 ($K_{57.5}$). The resulting magma series is as follows: calcic ($K_{57.5}$ = 0.4 to 1.2), calc-alkalic ($K_{57.5}$ = 1.2 to 2.4), high K calc-alkalic ($K_{57.5}$ = 2.4 to 3.0), alkali-calcic ($K_{57.5}$ = 3.0 to 4.4), and alkalic ($K_{57.5}$ = 4.4 to 6.0). Deposits associated with the calc-alkaline magma series are further subdivided into stock (e.g., Kitsault, British Columbia) and plutonic types (e.g., Endako, British Columbia). Deposits associated with the alkali-calcic magma series are further subdvided into Climax- and transitional-type (e.g., Mount Hope) deposits. Alkalic porphyry Mo deposits are unusual because of their extremely restricted distribution (e.g., Malmberg, Greenland). The correlation between K_2O and SiO_2 for the Trout Lake stock is weak and affected by alteration intensity. When pervasively altered samples are removed from the SiO_2 vs. K_2O plot, the correlation becomes stronger and a $K_{57.5}$ value of 1.3 is obtained. Magma chemistry and the stock-like morphology of the host intrusion allow the MAX to be classified as a stock-type calc-alkaline deposit, as defined by Westra and Keith (1981).

Despite the lack of consensus in the scientific literature, all of these classification schemes are broadly equivalent and divide porphyry Mo deposits into two types: (1) high grade, rift related, fluorine rich deposits associated with alkali-calcic intrusions, and (2) low grade, subduction related, fluorine-poor deposits associated with calc-alkaline intrusions (Carten et al., 1997). MAX fits all of the criteria for the second type of deposit.

3.3 Geochronology Discussion

Previous studies have demonstrated that giant porphyry deposits possess long-lived histories of magmatic–hydrothermal activity (Marsh et al., 1997; Richards et al., 1999; Selby and Creaser, 2001; Harris et al., 2008; and others). These protracted magmatic–hydrothermal histories provide the opportunity to develop multiple overprinting ore zones. Individual mineralizing events within large porphyry deposits occur over a much more restricted period of time (Marsh et al., 1997). Similar studies have not focused on small porphyry Mo deposits. One of the primary focuses of the current project is to integrate several geochronological methods to determine if the absolute timing of Mo mineralization, hydrothermal alteration, and igneous activity can be resolved outside of analytical error. All Re–Os molybdenite and U–Pb zircon dates at MAX are within analytical error of one another (Fig. 41). This confirms that igneous

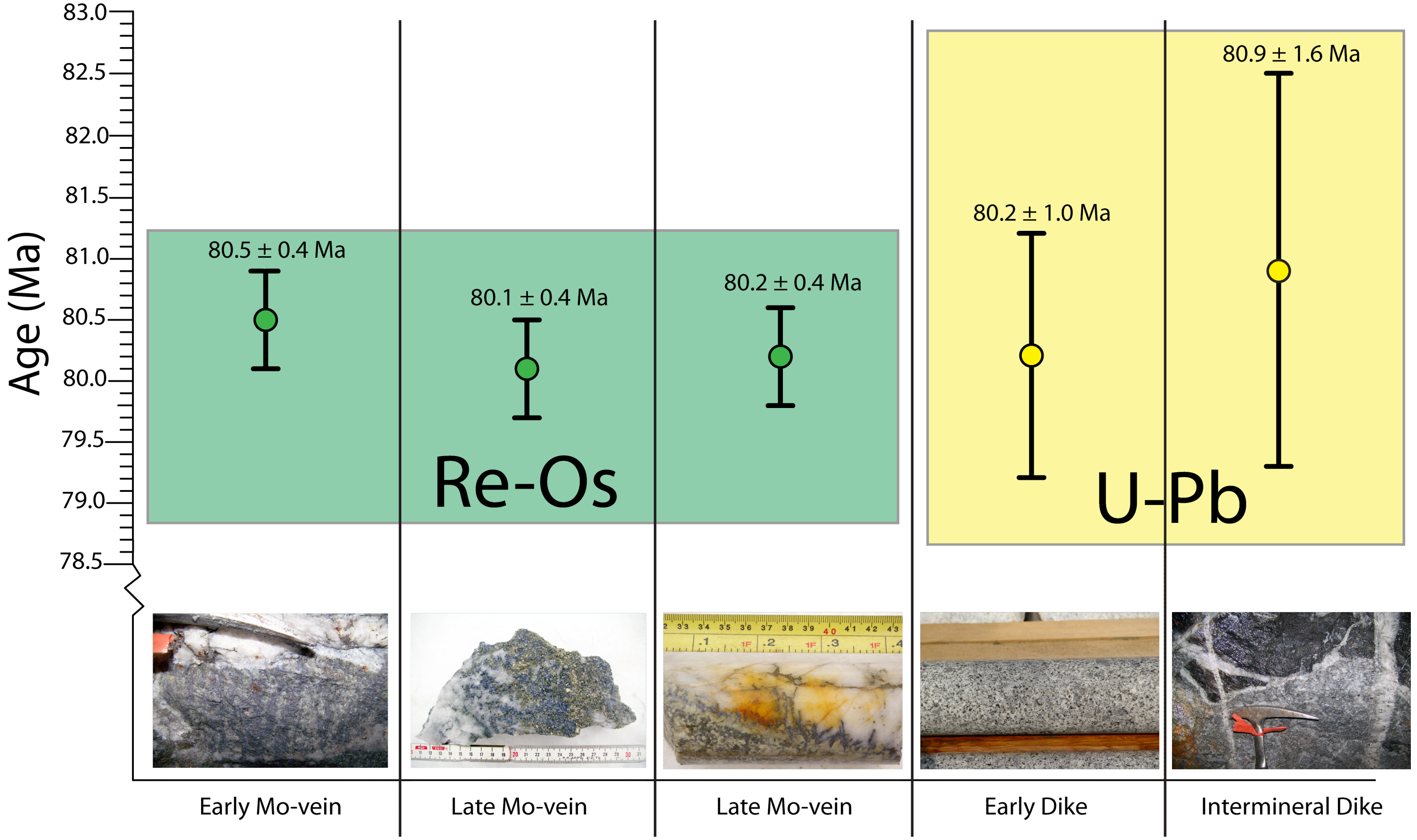

Figure 41. Diagram summarizing Re–Os and U–Pb geochronology. Note how all three Re–Os and two U–Pb dates are within error of each other. U–Pb dates are $^{206}Pb/^{238}U$ weighted average ages from selected zircons (see text). Re–Os dates are model ages (see text). Errors are reported at 2σ and include analytical and decay constant uncertainties.

activity and mineralization are coeval and that Mo mineralization occurred over a time span of ≤ 1,000,000 yr.

The rapid formation of the MAX deposit is not unique. Simmons and Brown (2007) used the metal fluxes from modern geothermal systems to calculate that the metal budget of the largest epithermal ore deposits in the world could have formed in ≤50,000 yr. The analogy between near surface epithermal systems and porphyry deposits is not ideal: near-surface mineral deposition is extremely efficient due, in part, to steep thermal-gradients. However, the 42,940,000 tonne resource at MAX is a fraction of the metal budget of the largest epithermal deposits in the world. Giant porphyry Mo deposits, such as the +700 million tonne Henderson deposit, commonly show evidence of long-lived hydrothermal systems and multiple overprinting mineralized zones (Seedorff, 1988). Only one mineralized zone has been identified at MAX to date. Perhaps the smaller resource size of MAX is related to its restricted magmatic–hydrothermal history, and consequently narrow temporal window for ore formation. This would support the long-standing idea that deposits with protracted hydrothermal–magmatic histories allow for continued metal-upgrading, and is required for the formation of giant porphyry deposits.

3.4 Fluid Inclusion Discussion

3.4.1 Fluid Inclusion Pressure Correction

Measured homogenization temperatures of fluid inclusions provide minimum estimates of the original temperature of the hydrothermal fluid unless boiling occurred or an appropriate pressure correction can be established (Roedder and Bodnar, 1980). An independent estimate of temperature can be used to calculate trapping pressure if a well-constrained geobarometer is absent. Linnen and Williams-Jones (1990) used isochore projections and an independent temperature estimate from oxygen isotope analysis of quartz-muscovite pairs to calculate an entrapment pressure of 1.4 to 1.7 kbars at MAX. Uncertainties in the oxygen isotope analysis combined with the difficulty in generalizing isochores for MAX fluids makes this pressure estimate poorly constrained.

Mo vein trapping temperatures can be estimated from the mean homogenization temperature (i.e., 303°C) and salinity (i.e., 5 wt.% NaCl equivalent) of type 1 inclusions, an entrapment pressure range of 1.4–1.7 kbars, and the pressure correction method of Potter (1977). This corresponds to pressure corrections of 130° to 160°C, and fluid trapping temperatures of mean type 1 inclusions ranging from 430° to 460°C.

Pb-Zn-Ag vein trapping temperatures can be calculated in a similar manner using the mean temperature and salinity of type 1 inclusions from this vein type (i.e., 225°C and 4 wt.% NaCl equivalent). This corresponds to pressure corrections of 110° to 140°C and fluid trapping temperatures of mean type 1 inclusions ranging from 335° to 365°C. There is no evidence that pressure corrections changed during the transition from porphyry Mo to Pb-Zn-Ag mineralization but fluid temperatures appear to have fallen by approximately 100°C.

3.4.2 Fluid Evolution

Linnen and Williams-Jones (1990) observed that the proportion of type 2 inclusions increased from early to late veins. This observation led to the hypothesis that fluids at the MAX evolved to become increasingly carbonic over time. A large proportion of type 2 inclusions do not contain enough CO_2 to form a separate liquid CO_2 phase at room temperature. As a result, visually identifying type 1 and 2 inclusions is impossible and estimates of the relative abundance of fluid inclusion types is unsatisfactory. Even if the proportion of fluid inclusion types could be established, that proportion would not necessarily equate to the proportion of the fluids at the time of trapping. If the fluids at MAX did become increasingly carbonic with time, individual inclusions from late veins should contain a greater molecular proportion of CO_2 (X_{CO_2}) when compared to type 2 inclusions from early veins.

X_{CO_2} was estimated using the volume percentage of CO_2 and several assumptions: (1) CO_2 and H_2O are mutually insoluble at room temperature, (2) fluid inclusions can be modeled by the pure H_2O-CO_2 system, and (3) the volume percentage of a phase is proportional to its mole fraction. Microthermometric experiments demonstrate that type 2 inclusions do not represent pure H_2O-CO_2 systems (e.g., CO_2 melting temperatures ≠ -56.6°C and clathrate melting temperatures >10°C). However, because CO_2 in the majority of type 2 inclusions melts near the CO_2 eutectic and salinity is low; type 2 inclusions can be approximated by the pure H_2O-CO_2 system. Volume estimates of CO_2 and H_2O introduce additional error into the X_{CO_2} calculation. This is because fluid inclusion volumes need to be approximated by simple geometrical shapes. All of these assumptions and poorly defined variables make X_{CO_2} calculations only an approximation. Using the assumptions above, the X_{CO_2} of type 2 inclusions was calculated (Touret, 1977):

$$X_{CO_2} = \frac{\left(\frac{\rho(CO_2)}{\text{mol. wt. }(CO_2)} \times \text{vol. \% } CO_2\right)}{\left(\frac{\rho(CO_2)}{\text{mol. wt. }(CO_2)} \times \text{vol. \% } CO_2\right) + \left(\frac{\rho(H_2O)}{\text{mol. wt.}(H_2O)} \times \text{vol. \% } H_2O\right)}$$

Where:

$\rho(CO_2) = 0.70$ g/cm^3
mol.wt.(CO_2) = 44.01 g/mol
$\rho(H_2O) = 1.0$ g/cm^3
mol.wt.(H_2O) = 18.02 g/mol
vol. % CO_2 = The estimated volume percentage of CO_2 within an individual fluid inclusion at 25°C
vol. % H_2O = The estimated volume percentage of H_2O within an individual fluid inclusion at 25°C

Type 2 inclusions from Mo veins possess a mean X_{CO_2} of 0.08 ± 0.06 (n = 86). No systematic change in X_{CO_2} was observed from early to late veins. Type 2 inclusions from Pb-Zn-Ag veins possessed a mean X_{CO_2} of 0.08 ± 0.05 (n = 103). X_{CO_2} from all type 2 inclusions, regardless of vein type, were <0.22. These values are in good agreement with those obtained by Linnen and Williams-Jones (1990) who calculated X_{CO_2} for MAX fluids using the method of Parry (1986). X_{CO_2} calculations are also in good agreement with the semi-quantitative method of Brown and Lamb (1989). Thus, the identical X_{CO_2} in early and late veins provide no evidence that MAX fluids evolved to become increasingly carbonic.

The P-T-X conditions of MAX hydrothermal fluids are most easily explained by a heterogeneous fluid (i.e., variable X_{CO_2}) that precipitated Mo over a range of temperatures until sufficient cooling caused precipitation of Pb-Zn-Ag.

3.4.3 Fluid Sources

Most porphyry Mo deposits do not possess CO_2 rich fluids (Wilkinson, 2001). The hydrothermal fluids at MAX and the Cannivan Gulch porphyry Mo deposit provide exceptions to this generalization (Darling, 1994). Both deposits are examples of mineralized stocks that have intruded calcareous country rocks. Carbonic inclusions at Cannivan Gulch and MAX suggests a link between host-rock composition and fluid chemistry. Fluids that have equilibrated with carbonate rich rocks would become progressively enriched in CO_2 as a result of $CaCO_3$ dissolution and could explain the carbonic nature of type 2 inclusions. This process would also likely result in Ca-rich fluids which are not observed at MAX.

Linnen and Williams-Jones (1990) determined the $\delta^{18}O$ of mineralizing fluids at MAX to be 8.0‰. These authors interpreted $\delta^{18}O$ data to represent either a magmatic or modified meteoric fluid. Mo-bearing unidirectional solidification textures strongly imply that the fluids were dominantly of magmatic origin.

3.4.4 Fluid Characteristics of Porphyry Deposits

Hydrothermal ore deposits can be subdivided into different deposit types based on their fluid characteristics (Spooner, 1981; Lattanzi, 1994; Wilkinson, 2001). In these compilations, porphyry systems are characterized by high temperature (fluid inclusion homogenization temperatures ranging from 400° to 800°C) and extremely saline fluids (40 to 70 wt.% NaCl equivalent).

This generalization is largely based on the study of porphyry Cu deposits. Hydrothermal fluids in porphyry Mo deposits are typically lower temperature and significantly lower salinity than porphyry Cu deposits (Wilkinson, 2001). Differences in hydrothermal characteristics help to explain the different metallogeny of the two deposit types. Cu solubility is strongly controlled by the concentration of NaCl in the hydrothermal fluid because of the importance of Cl as a complexing ligand (Yardley, 2005). Mo is not affected by NaCl concentrations because it complexes as an oxyacid molecule, as demonstrated in this reaction (Linnen et al., 1995) :

$$H^+ + HMoO_4^- + S_2 = MoS_2 + H_2O + 3/2O_2$$

The different behaviors of Mo and Cu in hydrothermal fluids may explain why igneous intrusions of similar composition and tectonic setting may produce Cu ± Mo deposits in some cases and Mo deposits in others (Candela and Holland, 1984).

Previous porphyry Mo fluid inclusion studies have focused on the rift-type deposits (Hall et al., 1974; Kamilli, 1978; Bloom, 1981; White et al., 1981; Shaver, 1984; Cline and Bodnar, 1994; Klemm et al., 2008). Fluid inclusion studies at these deposits have been problematic because of multiple overprinting hydrothermal events. Interpretation of secondary and primary inclusions becomes virtually impossible when quartz veins with protracted histories of crystallization are studied. Notwithstanding these challenges, Bloom (1981) was able to identify common molybdenite depositional environments for several deposits. The majority of Mo mineralization at the Questa deposit is associated with moderate salinity (30 to 60 wt.% NaCl equivalent) or low salinity (5 to 15 wt.% NaCl equivalent) fluids that typically homogenize at 390°C (Bloom, 1981). Similar bi-modal salinity distributions and homogenization temperatures are observed at the Henderson deposit, Colorado (White et al., 1981). Despite the variability of fluid characteristics at the deposit scale, certain generalizations can be made. Rift-type deposits commonly possess an early barren, hot, and hypersaline fluid that evolves through a variety of processes to a cooler and lower salinity fluid from which the bulk of Mo is precipitated. This evolution has been interpreted as a result of mixing between magmatic and meteoric water (Hall et al., 1974; Bloom, 1981). Detailed fluid inclusion studies at arc-type deposits are more rare (Burrows and Spooner, 1987; Darling 1994; Linnen and Williams-Jones, 1990; Selby et al., 2000). Fluids associated with molybdenite in these deposits are typically less saline (2 to 15 wt.% NaCl equivalent) and possess a lower range of homogenization temperatures (196° to 430°C). MAX fluids closely resemble the composition and homogenization temperatures of other arc-type porphyry Mo deposits.

Most porphyry deposits are characterized by large tonnages of low-grade mineralization. MAX is unusual because of a high-grade zone within a much larger and lower grade resource. Mo grade is controlled by a variety of factors. Many high-grade Mo deposits are associated with highly-differentiated granites that contain a large proportion of Si and F. These elements are thought to increase Mo solubility in the melt and contribute to the higher grades of Henderson and Climax Mo deposits (Gunow, 1983). The Trout Lake stock does not contain any unusual lithogeochemical characteristics that would support this as a possible explanation for the elevated Mo grades at MAX. As discussed above, Mo solubility is controlled by the P-T-X conditions of the hydrothermal fluid. Fluid characteristics at MAX are typical of low-grade Mo deposits and do not support unusual fluid P-T-X conditions as a possible explanation for the deposit's high-grade core. One unusual feature at MAX is the association of high-grade Mo with sheeted quartz veins. Quartz vein density within this zone exceeds 100s of veins per meter. Dike and vein orientations in the high-grade core appear to be strongly controlled by the regional foliation. It is therefore suggested that the pervasive foliation of the Lardeau meta-sedimentary rocks may have focused the flow of hydrothermal fluids and promoted efficient Mo deposition.

3.4.5 Link Between Porphyry Mo and Pb-Zn-Ag veins

One of the main objectives of the current study was to evaluate the genetic link between Pb-Zn-Ag vein deposits and the MAX porphyry. Significant temperature differences exist between the Mo- and Pb-Zn-Ag-bearing veins. Fluid inclusions from both vein types possess a similar range in trapping temperatures but Pb-Zn-Ag vein inclusions are centered at much lower temperatures (i.e., Mo vein trapping temperatures for mean type 1 inclusions range from 430° to 460°C and Pb-Zn-Ag vein trapping temperatures of mean type 1 inclusions range from 335°to 365°C). Lower trapping temperatures for Pb-Zn-Ag veins are in good agreement with the late- and distal-nature of the veins.

Mo- and Pb-Zn-Ag-bearing veins possess identical salinity distributions.

Type 2 inclusions in both vein types possess lower salinities than type 1 inclusions (Fig. 36). This could reflect a natural variation or represent an artefact of estimating salinity by assuming fluid inclusions represent pure H_2O-CO_2-NaCl systems. Despite these two possibilities, low-salinity fluids dominate both vein types. Pb, Zn, and Cu solubility is enhanced by complexing with Cl^- in hydrothermal fluids. Low-salinity fluids at MAX may explain the relatively-low sulphide abundance in Pb-Zn-Ag veins, and lack of significant Cu in the higher temperature Mo veins.

The identical composition (i.e., X_{CO_2} and salinity) of fluid inclusions from both vein types implies that hydrothermal fluids responsible for MAX Mo mineralization are the same as those that produced Pb-Zn-Ag deposits. The lower trapping temperatures (approximately 100°C) of Pb-Zn-Ag veins suggest hydrothermal fluids cooled significantly before base- and precious-metal precipitation.

Other studies have also suggested that Pb-Zn-Ag deposits in the Kootenay Arc could be related to post-kinematic intrusions. As early as 1929, Walker et al. (1929) attributed the Pb-Zn-Ag mineralization “to have been formed by ascending heated solutions which originated during the final stage of consolidation of the magma or magmas that formed the Kuskanax batholith and other masses of igneous rock that more or less surround the district on three sides” (Walker et al., 1929, p. 31). This hypothesis was supported by the close association between igneous dikes and mineralized veins at some deposits. Linnen and Williams-Jones (1987) observed that veins at the MAX, Lucky Boy, and Copper Chief deposits reflect a similar regional stress regime. Regional studies by Sinclair (1966) and Andrew et al. (1984) proposed that anomalous Pb ratios in galena ore from a number of Pb-Zn-Ag deposits may be related to post-kinematic intrusions. Here we identify a genetic link between these two deposit types based on the similar chemistry of the hydrothermal fluids.

Late Pb-Zn-Ag veins are also observed at other porphyry Mo deposits/ districts (e.g., Colorado Mineral Belt, Idaho-Montana porphyry belt, and several porphyry Mo deposits in British Columbia; Soregaroli and Sutherland Brown, 1976; Seedorff et al., 2005; Worthington, 2007). Base and precious metal veins commonly extend further than Mo veins and act to broaden the hydrothermal footprint of porphyry mineralization. Establishing a genetic link between Mo- and Pb-Zn-Ag mineralization at MAX has important implications for on-going mineral exploration efforts for MAX analogs.

3.5 Comparison With Other British Columbia Porphyry Mo Deposits

MAX and most other BC porphyry Mo deposits can be classified as low grade, arc related deposits associated with fluorine-poor and calc-alkaline magma (Carten et al., 1997). Examples of other important porphyry Mo deposits include: Endako (141± 5 Ma), Boss Mountain (102 ± 4 Ma), Glacier Gulch (73.3 ± 3.4 Ma), Adanac (62 Ma), and the Alice Arm deposits (e.g., B.C. Molybdenum; 50 Ma). Of these, only the Endako deposit has been studied in any great detail (Selby et al., 2000, Selby and Creaser, 2001; Villeneuve et al., 2001). Interest in the Endako deposit coincides with its position as Canada's largest Mo producer and one of the larger Mo producers in the world.

Most BC porphyry Mo deposits are situated within the intermontane tectonic belt and are genetically associated with calc-alkaline intrusions that formed in a paleo-arc tectonic setting (Fig. 2). Deposit ages range from the Mesozoic to Cenozoic. Host intrusive rocks are typically porphyritic, and range in modal mineralogy from granodiorite–monzogranite. Molybdenite is typically the only mineral present in economic quantities; however, tungsten, bismuth, and Pb-Zn-Ag mineralization is commonly present. Alteration assemblages can be generalized to consist of potassic (K feldspar and biotite), phyllic (muscovite), argillic (clay minerals), and propylitic (chlorite, epidote, zoisite, albite, carbonate). Each alteration assemblage has been linked to specific stages of mineralization (Soregaroli and Sutherland Brown, 1976). Host intrusion morphology ranges from elongate (e.g., Endako) to cylindrical (e.g., Glacier Gulch). Ore body morphology ranges from tabular (e.g., Adanac) to annular (e.g., BC Molybdenum). The grade, size, and magmatic–hydrothermal characteristics of most BC porphyry Mo deposits are also evident at MAX.

Porphyry Mo deposits in BC tend to cluster in space and time (e.g., Alice Arm District). The apparent isolation of the MAX in southeast–BC may be more related to the difficulties in exploring for this deposit type than to an isolated magmatic event. Middle Cretaceous plutons in and around Trout Lake are also associated with molybdenite showings, but MAX is currently the only Mo producer in the area.

3.6 Comparison with Porphyry Mo deposits in the Idaho–Montana Mineral Belt

Geochemical and temporal similarities between igneous rocks in southern British Columbia and northwestern USA have led many authors to correlate magmatic events across the international border (Miller and Engels, 1975; Armstrong et al., 1977; O`Brien et al., 1991). Mesozoic magmatism is particularly well represented in both countries, and implies a similar tectonic environment. Southeastern British Columbia and northwestern USA also share similar metallogenic characteristics. Similar-aged porphyry Mo deposits and Pb-Zn-Ag deposits suggest that these areas form one continuous metallogenic province (Zartman and Stacey, 1971; Andrew et al., 1984).

Porphyry Mo deposits within the Idaho–Montana porphyry belt fall into three major metallogenic epochs: Tertiary (55–36 Ma), Laramide (78–60 Ma), and Pre-Laramide (>78 Ma). Deposits associated with each epoch share a number of similarities that warrant their separate discussion. Tertiary porphyry Mo deposits in Idaho–Montana are associated with highly evolved granite and rhyolite. Source intrusions range in age from 55 to 36 Ma (Worthington, 2007). CUMO, Little Falls, Emmigrant Gulch, and Big Ben are characteristic deposits of this age group. Molybdenite is typically associated with silicified, sericitized, and pyritized zones within the host intrusion. Tertiary deposits can be distinguished from older deposits based on negative Eu anomalies and other chemical characteristics of the source intrusions. The association of Mo with highly-evolved granite is typical of the high grade, rift related, fluorine-rich porphyry Mo deposit type, whereas the low grade and small size of Tertiary deposits is more typical of the subduction related, fluorine-poor porphyry Mo deposits.

Laramide deposits (78–60 Ma) are the most numerous deposit type in the Idaho–Montana Porphyry belt and are almost exclusively associated with granodiorite intrusions. The calc-alkaline affinity and age of the Laramide deposits led Westra and Keith (1981) to group these deposits, with MAX, into a similar magmatic–metallogenic epoch. Lithogeochemistry from this study supports this hypothesis (Figs. 39 and 40). MAX and Laramide deposits, such as White Cloud and Cannivan Gulch, possess very similar REE patterns and plot in similar locations on granite discrimination diagrams (Fig. 42). Molybdenite

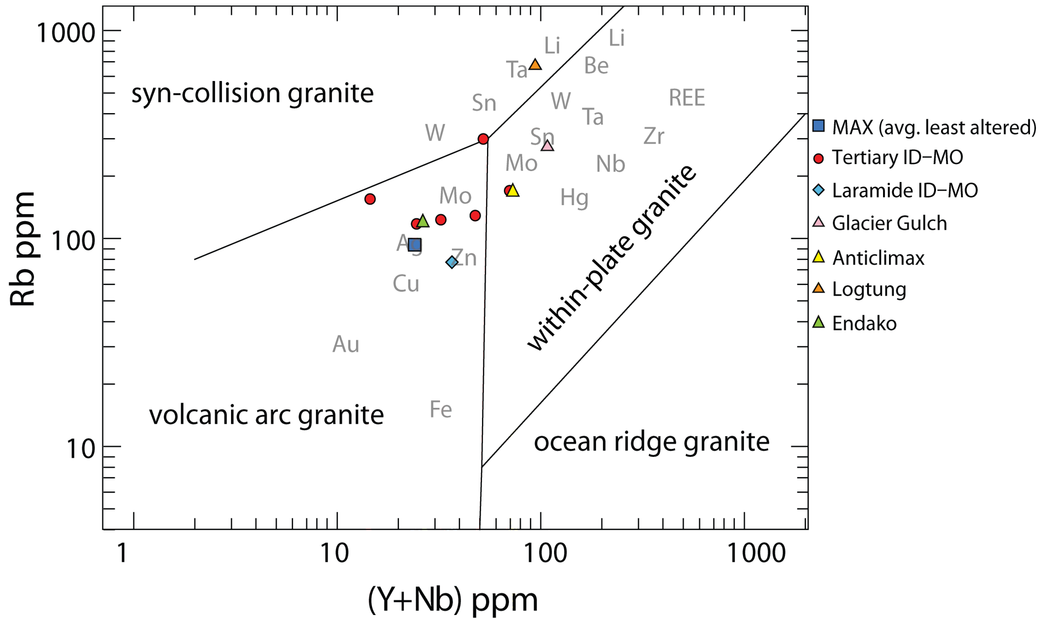

Figure 42. Granite discrimination diagram (Pearce et al., 1984) comparing the tectonic affinity of source intrusions from different porphyry Mo deposits. Elements represent the composition of granite and rhyolite rocks that are host to deposits of that metallogeny (Christiansen and Keith, 1996). Idaho–Montana (ID–MO) porphyry deposit data compiled from Taylor et al. (2007); Glacier Gulch, Anticlimax, Logtung data compiled from Kirkham and Sinclair (1988); Endako data compiled from Whalen et al. (2001).

mineralization within Laramide deposits is typically associated with sericite, silica, and pyrite altered dikes and/or a weakly developed quartz vein stockworks. Minor scheelite and Pb-Zn-Ag is present in quartz veins and some deposits possess peripheral skarn zones. Metal resources for most Laramide deposits are lower than MAX. The Thompson Creek deposit is an exception, with a measured resource of 173 million tonnes at 0.115% Mo (cut-off at 0.05% Mo; Worthington, 2007). Laramide porphyry Mo deposits are typical of the low grade, subduction related, fluorine-poor porphyry Mo deposit type associated with calc-alkaline intrusions.

Chemical, lithological, and temporal similarities between Laramide deposits and MAX suggest the presence of a continuous metallogenic province that extends from southeast–BC into northwestern USA. Future exploration should focus on this highly prospective and underexplored area.

3.7 Implication of Late Cretaceous Magmatism in the Kootenay Arc

The Canadian Cordillera is most easily explained as a collisional orogeny that resulted from the docking of at least 2 allochthonous terranes (Intermontane and Insular terranes) with the western margin of the North American continent (Monger et al., 1972). These two allochthonous terranes are interpreted to have collided with North America over a time span ranging from the Middle Jurassic to Middle Cretaceous, and Early Cretaceous to Early Cenozoic (Price et al., 1981). The Omineca crystalline belt, in which MAX is situated, is thought to have formed as a result of these collisions. Armstrong (1988) summarized the magmatic evolution of the Canadian Cordillera and identified several magmatic epochs. These magmatic epochs relate in space and time to the accretion of allochthonous terranes. Systematic changes in granitoid lithogeochemistry through time reflects the evolution of the continental lithosphere during the formation of the Cordillera.

Ghosh (1995) related igneous pluton chemistry to tectonic models south of Trout Lake. Three magmatic epochs are represented by granitic batholiths in and around Trout Lake (within a 100 km radius of MAX). The Middle Jurassic (173 ± 5 Ma) Kuskanax batholith is located approximately 5 km south of the Trout Lake stock (Parrish and Wheeler, 1983). The age and syntectonic nature of the Kuskanax batholith places important constraints on Mesozoic deformation. Most of the Kuskanax batholith can be classified as a clinopyroxene- and amphibole-bearing alkaline quartz monzonite. Parrish and Wheeler (1983) interpreted the Kuskanax to have been derived from an upper mantle source based on the alkaline nature of the intrusion and a range of $^{87}Sr/^{86}Sr$ ratios from 0.7045 to 0.7050. A $^{87}Sr/^{86}Sr$ ratio greater than 0.706 typically represents assimilation of continental lithosphere, whereas lower $^{87}Sr/^{86}Sr$ ratios are indicative of a mantle contribution. Lithogeochemical data obtained from the current study indicate that the Kuskanax batholith is typical of volcanic-arc granites (Fig. 38).

A number of smaller stocks are located on the eastern margin of the Kuskanax batholith. Roback (1993) analyzed these smaller satellite stocks using petrography and U–Pb geochronology and interpreted them to be genetically related to the Kuskanax batholith. The Galena Bay stock is situated at the northern end of the Kuskanax batholith and was emplaced at 161.60 ± 5 Ma (Parrish and

Armstrong, 1987). Trace element patterns obtained from this study suggest that the Galena Bay stock is also typical of volcanic arc granites (Fig. 38).

Approximately 30 km north of the Trout Lake stock is a southeast-trending series of Middle Cretaceous batholiths that include the Battle Range, Bugaboo, and Horsethief Creek. All three of these batholiths are dominantly biotite-hornblende granite and are interpreted to be post-kinematic based on map patterns and the lack of a metamorphic fabric. $^{87}Sr/^{86}Sr$ ratios from the Bugaboo and Horsethief Creek biotite granites range from 0.7072 to 0.7115 (Brandon and Lambert, 1993).

The Fry Creek batholith is another Middle Cretaceous batholith located approximately 90 km southeast of MAX. Biotite granite and a two-mica granite are the dominant lithologies at this locality. $^{87}Sr/^{86}Sr$ ratios are some of the highest of any pluton in the Kootenay Arc and reach 0.7428. Two-mica granites from the Fry Creek batholith are strongly peraluminous and can be distinguished from the Bugaboo and Horsethief Creek biotite granite using trace element lithogeochemistry and petrography.

Trace element chemistry indicates that Middle Cretaceous batholiths are typical of within-plate or syn-collisional granites (Fig. 38). Sr and Nd isotopic evidence from these plutons led Brandon and Lambert (1984) to suggest that the Bugaboo, Horsethief Creek, and Fry Creek batholiths are the result of crustal anatexis and crustal thickening. Armstrong (1988) came to a similar conclusion using Sr data from a large number of Middle Cretaceous plutonic rocks throughout the Cordillera. $^{87}Sr/^{86}Sr$ ratios from Middle Cretaceous batholiths commonly exceed 0.710 and are interpreted to reflect a different thermal state of the crust as a consequence of crustal thickening (Armstrong, 1988). Middle Cretaceous plutons are interpreted to be post-kinematic (Brandon and Lambert, 1993) and were emplaced into a tectonically dormant suprastructure (Archibald et al., 1984).

The Trout Lake stock (~80 Ma) and the Whatshan Batholith (79 ± 2 Ma; Parrish, 1992) are the only known Late Cretaceous intrusions within 100 km of Trout Lake. Major and trace element patterns indicate that the Trout Lake stock is typical of volcanic arc granitoids (Fig. 38). The presence of Late Cretaceous volcanic arc granitoids in the Kootenay arc suggests that arc magmatism persisted until the Cenozoic and departs from magma chemistry of Middle Cretaceous plutonism. Arc magmatism was likely related to continued convergence between Quesnelia and the North American continent (Ghosh, 1995).

3.8 Mineral Exploration Implications

i. Post-kinematic igneous intrusions in and around MAX should be rigorously tested for Mo mineralization by diamond drilling. Major element chemistry of MAX phases indicates that siliceous intrusive rocks are ideal host rocks for this style of mineralization. Middle Cretaceous batholiths such as Battle Range, Horsethief Creek, and Fry Creek are also associated with Mo mineralization, although no economic deposits have been discovered to date.

ii. REE patterns of MAX intrusive phases are distinct from nearby unrelated older igneous batholiths and stocks. This chemical fingerprint could be used to distinguish igneous phases related to MAX from superficially similar and barren Jurassic granitoids.

iii. Re–Os and U–Pb geochronology confirm the Late Cretaceous age of the MAX deposit. Porphyry Mo deposits rarely occur in isolation. Alice Arm, Idaho–Montana, and Colorado are examples of porphyry Mo districts that define distinct metallogenic epochs. Undiscovered MAX analogs should be expected in the area and Late Cretaceous intrusions should be priority targets.

iv. Many lessons can be learned from exploration at MAX. The Trout Lake stock is poorly exposed at surface and the majority of mineralization is located 1km below the current ground level. Persistent drilling was required before significant mineralization was intersected. Early drilling identified increasing K feldspar / plagioclase ratios that correlated with increasing Mo grade. Small and blind deposits are difficult exploration targets; however, proper identification of alteration mineralogy can be used to vector towards porphyry Mo mineralization.

v. Mo mineralization is genetically related to W and Pb-Zn-Ag mineralization at MAX. This metal association could be used as a vector towards porphyry Mo mineralization. Over a hundred years of exploration for base-metal mineralization has resulted in a comprehensive database of Pb-Zn-Ag deposit locations and characteristics (British Columbia

Geological Survey, 2006). Interest in molybdenum has been sporadic but with a recent resurgence. As a result, less is known about molybdenum prospects in the Kootenay Arc. The beginning stage of any exploration program offers the daunting task of targeting specific areas that require additional attention. Our findings suggest that areas with anomalous concentrations of Pb-Zn-Ag vein deposits warrant further investigation for potential porphyry Mo mineralization (e.g., the Middle Cretaceous Battle Range Batholith north of MAX is associated with W skarn and Pb-Zn-Ag veins).

vi. North-south trending faults bound the MAX deposit on the east and west sides. These faults locally post-date the Trout Lake stock and Mo mineralization. In other exposures, mineralized quartz veins crosscut similar faults. This suggests that some of these faults were active during mineralization (Fig. 11). The orientation of these faults is unique relative to the dominant northwest fabric of southeastern British Columbia. Archibald et al. (1984) attributed similar north-south faults in the Kootenay Arc to uplift that continued until the Eocene. Late north-south faults may be important magma emplacement mechanisms (Richards, 2003; Tosdal and Richards, 2004) during the Late Cretaceous and could be associated with porphyry Mo mineralization elsewhere in the Kootenay Arc.

vii. The dominant north-west fabric of southeastern BC appears to have impacted the shape of the Trout Lake stock. MAX is an unusual porphyry Mo deposit because of the vertically attenuated nature of mineralization and igneous dikes. High-grade mineralization, hosted by the Trout Lake stock and within sheeted quartz veins, strikes parallel to the regional foliation. The lensoid shape of mineralization is best tested by drilling perpendicular to the regional foliation. This drilling orientation maximizes the chance of intersecting potential mineralizing hosts.

viii. The temporal setting and calc-alkaline affinity of MAX and some porphyry deposits from the Idaho-Montana porphyry belt led Westra and Keith (1981) to group these deposits into the same metallogenic epoch. Trace element chemistry from this study suggests a petrogenetic link between these deposits and implies a continuous metallogenic province that extends from southeastern British Columbia to northwestern USA.

4.0 Conclusions

i. The MAX deposit formed at 80.2 ± 1.0 Ma when the Trout Lake stock was emplaced into meta-sedimentary rocks of the Lardeau Group. Mo-bearing fluids exsolved directly from the Trout Lake stock to form a high-grade core within a much larger and lower grade resource.

ii. MAX is typical of low grade, arc-related deposits associated with fluorine-poor and calc-alkaline magmas (Carten et al., 1997). Most other porphyry Mo deposits in British Columbia also fall into this deposit type.

iii. Re–Os molybdenite geochronology from early and late veins are within analytical error of each other with a weighted average of 80.3 ± 0.2 Ma. These dates are in good agreement with U–Pb zircon crystallization ages of the host Trout Lake stock at 80.9 ± 1.6 Ma and 80.2 ± 1.0 Ma. All 5 dates are within analytical error of each other and suggest the magmatic–hydrothermal system at MAX was short-lived (i.e., ≤1,000,000 yr.).

iv. Biotite granodiorite, biotite tonalite, biotite quartz diorite, and aplite dikes are the main intrusive phases at MAX. All four major phases are coeval with Mo mineralization. Intrusive–country rock contacts suggest that country rock assimilation, magma mixing, and stoping occurred during emplacement of the Trout Lake stock.

v. Hydrothermal alteration evolved from early biotite hornfels and skarn, through potassic and silicic, to phyllic, and late propylitic. Molybdenite is associated with each alteration stage but is most abundant in the potassic–silicic core of the deposit.

vi. Similarities between fluid characteristics of Mo- and Pb-Zn-Ag-bearing veins genetically links porphyry Mo mineralization with peripheral Pb-Zn-Ag veins at MAX.

vii. The approximately 100˚C disparity between the temperatures of Mo- (T_t = 430° to 460°C) and Pb-Zn-Ag-bearing (T_t = 335° to 365°C) veins suggests that cooling was the predominant control on mineral deposition.

viii. Fluid inclusion microthermometry reveal no systematic change in hydrothermal fluid composition (i.e., X_{CO_2} or salinity) during Mo deposition.

ix. Late Cretaceous arc magmatism is indicative of continued convergence between North America and allochthonous terranes until the Cenozoic.

x. Lithogeochemical and temporal similarities between MAX and Laramide-aged deposits in the Idaho-Montana porphyry belt support the presence of a metallogenic province that extends from southeastern British Columbia to northwest USA.

5.0 References

Andrew, A., Godwin, C.I., and Sinclair, A.J., 1984, Mixing line isochrons; a new interpretation of galena lead isotope data from southeastern British Columbia: Economic Geology and the bulletin of the Society of Economic Geologists, v. 79, p. 919–932.

Archibald, D.A., Glover, J.K., Price, R.A., Farrar, E., and Carmichael, D.M., 1983, Geochronology and tectonic implications of magmatism and metamorphism, southern Kootenay Arc and neighboring regions, southeastern British Columbia; Part I, Jurassic to Mid-Cretaceous: Canadian Journal of Earth Sciences, v. 20, p. 1891–1913.

Archibald, D.A., Krogh, T.E., Armstrong, R.L., and Farrar, E., 1984, Chronology and tectonic implications of magmatism and metamorphism, southern Kootenay Arc and neighboring regions, southeastern British Columbia; Part II, Mid-Cretaceous to Eocene: Canadian Journal of Earth Sciences, v. 21, p. 567–583.

Armstrong, R.L., 1988, Mesozoic and early Cenozoic magmatic evolution of the Canadian Cordillera, *in* Clark, S.P.J., Burchfiel, C.B., and Suppe, J., eds., Processes in continental lithospheric deformation, Geological Society of America Special Paper, v. 218: Boulder, Geological Society of America, p. 55–91.

Armstrong, R.L., Taubeneck, W.H., and Hales, P.O., 1977, Rb–Sr and K–Ar geochronometry of Mesozoic granitic rocks and their Sr isotopic composition, Oregon, Washington, and Idaho: Geological Society of America Bulletin, v. 88, p. 397–411.

Bloom, M.S., 1981, Chemistry of inclusion fluids; stockwork molybdenum deposits from Questa, New Mexico, and Hudson Bay Mountain and Endako, British Columbia: Economic Geology and the bulletin of the Society of Economic Geologists, v. 76, p. 1906–1920.

Bodnar, R.J., 1993, Revised equation and table for determining the freezing point depression of H_2O-NaCl solutions: Geochimica et Cosmochimica Acta, v. 57, p. 683–684.

Boyle, C.H., and Leitch, C.H.B., 1983, Geology of the Trout Lake molybdenum deposit, BC: Canadian Institute of Mining and Metallurgy Bulletin, v. 76, p. 115–124.

Boyle, H.C., and Parliament, J.H., 1983, Final report; Trout Lake molybdenum project: Unpublished Report, Newmont Exploration Canada Ltd., 48 p.

Bozzo, A.T., Chen, H.S., Kass, J.R., and Barduhn, A.J., 1975, The properties of the hydrates of chlorine and carbon dioxide: Desalination, v. 16, p. 303–320.

Brandon, A.D., and Lambert, R.S.J., 1993, Geochemical characterization of mid-Cretaceous granitoids of the Kootenay Arc in the southern Canadian Cordillera: Canadian Journal of Earth Sciences, v. 30, p. 1076–1090.

British Columbia Geological Survey, 2006, MapPlace GIS internet mapping system, British Columbia Ministry of Energy, Mines and Petroleum Resources, (http://www.mapplace.ca).

Brock, R.W., 1904, Sketch map showing Lardeau and Trout Lake mineral belts, west Kootenay District, British Columbia: Geological Survey of Canada, Multicoloured Geological Map 853.

Brown, P.E., and Lamb, W.M., 1989, P-V-T properties of fluids in the system H2O-CO2-NaCl; new graphical presentations and implications for fluid inclusions studies: Geochimica et Cosmochimica Acta, v. 53, p. 1209–1221.

Brown, G.C., Thorpe, R.S., and Webb, P.C., 1984, The geochemical characteristics of granitoids in contrasting arcs and comments on magma sources: Journal of the Geological Society of London, v. 141, p. 413–426.

Burrows, D.R., and Spooner, E.T.C., 1987, Generation of a magmatic H_2O-CO_2 fluid enriched in Mo, Au, and W within an Archean sodic granodiorite stock, Mink Lake, northwestern Ontario: Economic Geology and the bulletin of the Society of Economic Geologists, v. 82, p. 1931–1957.

Candela, P.A., and Holland, H.D., 1984, The partitioning of copper and molybdenum between silicate melts and aqueous fluids: Geochimica et Cosmochimica Acta, v. 48, p. 373–380.

Carten, R.B., Walker, B.M., Geraghty, E.P., and Gunow, A.J., 1988, Comparison of field-based studies of the Henderson porphyry molybdenum deposit, Colorado, with experimental and theoretical models of porphyry systems, *in* Taylor, R.P., and Strong, D.F., eds., Recent advances in the geology of granite-related deposits, Canadian Institute of Mining and Metallurgy Special Volume 39: Montreal, Canadian Institute of Mining and Metallurgy, p. 351–366.

Carten, R.B., White, W.H., and Stein, H.J., 1997, High-grade granite-related molybdenum systems; classification and origin, *in* Kirkham, R.V., Sinclair, W.D., Thorpe, R.I., and Duke, J.M., eds., Mineral deposit modeling, Geologic Association of Canada Special Paper v. 40: St. John's, Geologic Association of Canada, p. 521–554.

Carter, N.C., 1981, Porphyry copper and molybdenum deposits west-central British Columbia: British Columbia Ministry of Energy, Mines, and Petroleum Resources Bulletin, v. 64, 150 p.

Christiansen, E.H., and Keith, J.D. 1996. Trace element systematics in silicic magmas; a metallogenic perspective, *in* Wayne, D.A., ed., Trace element geochemistry of volcanic rocks; applications for massive sulphide exploration, Geological Association of Canada, Short Course Notes 12: St. John's, Geologic Association of Canada, p. 115–151.

Clark, K.F., 1972, Stockwork molybdenum deposits in the western Cordillera of North America: Economic Geology and the bulletin of the Society of Economic Geologists, v. 67, p. 731–758.

Cline, J.S., and Bodnar, R.J., 1994, Direct evolution of brine from a crystallizing silicic melt at the Questa, New Mexico, molybdenum deposit: Economic Geology and the bulletin of the Society of Economic Geologists, v. 89, p. 1780–1802.

Cocherie, A., and Robert, M., 2008, Laser ablation coupled with ICP-MS applied to U–Pb zircon geochronology: a review of recent advances: Gondwana Research, v. 14, p. 597–608.

Collins, P.L.F., 1979, Gas hydrates in CO_2-bearing fluid inclusions and the use of freezing data for estimation of salinity: Economic Geology and the bulletin of the Society of Economic Geologists, v. 74, p. 1435–1444.

Colpron, M., and Price, R.A., 1995, Tectonic significance of the Kootenay Terrane, southeastern Canadian Cordillera; an alternative model: Geology (Boulder), v. 23, p. 25–28.

Cox, K.G., Bell, J.D., and Pankhurst, R.J., 1979, The interpretation of igneous rocks: London, George Allen and Unwin., 496 p.

Creaser, R.A., Papanastassiou, D.A., and Wasserburg, G.J., 1991, Negative thermal ion mass spectrometry of osmium, rhenium, and iridium: Geochimica et Cosmochimica Acta, v. 55, p. 397–401.

Darling, R.S., 1994, Fluid inclusion and phase equilibrium studies at the Cannivan Gulch molybdenum deposit, Montana, USA, effect of CO_2 on molybdenite-powellite stability: Geochimica et Cosmochimica Acta, v. 58, p. 749–760.

Deckart, K., Clark, A.H., Aguilar, C., Vargas, R., Bertens, A., Mortensen, J.K., and Fanning, C.M., 2005, Magmatic and hydrothermal chronology of the giant Rio Blanco porphyry copper deposit, central Chile; implications of an integrated U-Pb and $^{40}Ar/^{39}Ar$ database, *in* Hedenquist, J.W., Thompson, J.F.H., Goldfarb, R.J., and Richards, J.P., eds., Economic Geology, 100th Anniversary Volume: Littleton, Society of Economic Geologists, p. 905–934.

deMille, G., 1976, K-Ar age determination for the Trout Lake stock: Unpublished report, Krueger Enterprises Inc., Geochron Laboratories Division, 1 p.

Emmens, N.W., 1914, The mineral resources of the Lardeau and Trout Lake mining divisions, British Columbia: British Columbia Bureau of Mines Bulletin, v. 2, 65 p.

Faure, G., 1986, Principles of isotope geology: New York, John Wiley & Sons, 589 p.

Fyles, J.T., 1966, Lead-zinc deposits in British Columbia, *in* Gunning, H.C., White, W.H., Little, H.W., Armstrong, J.E., Yates, R.G., Ney, C.S., and Holland, S.S., eds., A symposium on the tectonic history and mineral deposits of the western Cordillera in British Columbia and neighboring parts of the United States, Canadian Institute of Mining and Metallurgy Special Volume 8: Montreal, Canadian Institute of Mining and Metallurgy, p. 231–237.

Fyles, J.T., and Eastwood, G.E.P., 1962, Geology of the Ferguson area Lardeau District British Columbia: British Columbia Ministry of Energy, Mines, and Petroleum Resources Bulletin, v. 45, 92 p.

Ghosh, D.K., 1995, Nd-Sr isotopic constraints on the interactions of the Intermontane Superterrane with the western edge of North America in the southern Canadian Cordillera: Canadian Journal of Earth Sciences, v. 32, p. 1740–1758.

Griffiths, J.R., and Godwin, C.I., 1983, Metallogeny and tectonics of porphyry copper molybdenum deposits in British-Columbia: Canadian Journal of Earth Sciences, v. 20, p. 1000–1018.

Gunow, A.J., 1983, Trace element mineralogy in the porphyry molybdenum environment: Unpublished PhD thesis, Boulder, Colorado, University of

Colorado at Boulder.

Hall, W.E., Friedman, I., and Nash, T.J., 1974, Fluid Inclusion and light stable isotope study of the Climax molybdenum deposits, Colorado: Economic Geology and the bulletin of the Society of Economic Geologists, v. 69, p. 884–901.

Harris, A.C., Dunla, J.W., Reiners, P.W., Allen, C.M., Cooke, D.R., White, N.C., Campbell, I.H., and Golding, S.D., 2008, Multimillion year thermal history of a porphyry copper deposit; application of U-Pb, ^{40}Ar/ ^{39}Ar, and (U–Th)/He chronometers, Bajo de la Alumbrera copper-gold deposit, Argentina: Mineralium Deposita, v. 43, p. 295–314.

Haskin, L.A., Frey, F.A., Schmidt, R.A., and Smith, R.H., 1966, Meteoritic, solar and terrestrial rare-earth distributions: Physics and Chemistry of the Earth, v. 7, p. 167–321.

Haynes, F.M., 1985, Determination of fluid inclusion compositions by sequential freezing: Economic Geology and the bulletin of the Society of Economic Geologists, v. 80, p. 1436–1439.

Hedenquist, J.W., Arribas, A.J., and Reynolds, J.T., 1998, Evolution of an intrusion-centered hydrothermal system; far southeast-Lepanto porphyry and epithermal Cu-Au deposits, Philippines: Economic Geology and the bulletin of the Society of Economic Geologists, v. 93, p. 373–404.

Hedenquist, J.W., and Richards, J.P., 1998, The influence of geochemical techniques on the development of genetic models for porphyry copper deposits, *in* Richards, J.P., and Larson, P.B., eds., Techniques in Hydrothermal Ore Deposits Geology, Reviews in Economic Geology, v. 10: Littleton, Society of Economic Geologists, p. 235–256.

Hudson, T., Smith J.G., and Elliot, R.L., 1979, Petrology, composition, and age of intrusive rocks associated with the Quartz Hill molybdenite deposit, southeastern Alaska: Canadian Journal of Earth Science, v. 16, p. 1805–1822.

Heinrich, C.A., Driesner, T., Stefansson, A., and Seward, T.M., 2004, Magmatic vapour contraction and the transport of gold for the porphyry environment to epithermal ore deposits: Geology (Boulder), v. 32, p. 761–764.

Jaffey, A.H., Flynn, K.F., Glendenin, L.E., Bentley, W.C., and Essling, A.M., 1971, Precision measurement of half-lives and specific activities of ^{235}U and ^{238}U: Physical Review C, v. 4, p. 1889–1906.

Kamilli, R.J., 1978, The genesis of stockwork molybdenite deposits; implication from fluid inclusion studies at the Henderson Mine: The Geological Society of America (91st annual meeting), Abstracts with Programs, v. 10, p. 431.

Keith, J.D., and Shanks, W.C., 1988, Chemical evolution and volatile fugacities of the Pine Grove porphyry molybdenum and ash-flow tuff system, southwestern Utah, *in* Taylor, R.P., and Strong, D.F., eds., Recent advances in the geology of granite-related mineral deposits, Canadian Institute of Mining and Metallurgy Special Volume 39: Montreal, Canadian Institute of Mining and Metallurgy, p. 402–423.

Keith, S.B., 1978, Paleosubduction geometries inferred from Cretaceous and Tertiary magmatic patterns in southwestern North America: Geology (Boulder), v. 6, p. 516–521.

Kirkham, R.V., and Sinclair, W.D., 1984, Porphyry copper, molybdenum, tungsten, *in* Eckstrand, O.R., ed., Canadian mineral deposit types; a geological synopsis, Economic Geology Report v. 36: Ottawa, Geological Survey of Canada, p. 50–52.

Kirkham, R.V., and Sinclair, W.D., 1988, Comb quartz layers in felsic intrusions and their relationship to porphyry deposits, *in* Taylor, R.P., and Strong, D.F., eds., Recent advances in the geology of granite-related mineral deposits, Canadian Institute of Mining and Metallurgy Special Volume 39: Montreal, Canadian Institute of Mining and Metallurgy, p. 50–71.

Klemm, L.M., Pettke, T., and Heinrich, C.A., 2008, Fluid and source magma evolution of the Questa porphyry Mo deposit, New Mexico, USA: Mineralium Deposita, v. 43, p. 533-552.

Lattanzi, P., 1994, Fluids in ore deposits, *in* de Vivo, B., and Frezzotti, M.L., eds., Fluid inclusions in minerals; methods and applications: Blacksburg, Virginia Polytechnic Institute and State University, p. 297–307.

Le Maitre, R.W., 2002, Igneous rocks a classification and glossary of terms: Cambridge, Cambridge University Press, 236 p.

Linnen, R.L., and Williams-Jones, A.E., 1987, Tectonic control of quartz vein orientations at the Trout Lake stockwork molybdenum deposit, southeastern British Columbia; implications for metallogeny in the Kootenay Arc: Economic Geology and the bulletin of the Society of Economic Geologists, v. 82, p. 1283–1293.

—, 1990, Evolution of aqueous-carbonic fluids during contact metamorphism, wall-rock alteration, and molybdenite deposition at Trout Lake, British Columbia: Economic Geology and the bulletin of the Society of Economic Geologists, v. 85, p. 1840–1856.

Linnen, R.L., Williams-Jones, A.E., Leitch, C.H.B., and Macauley, T.N., 1995, Molybdenum mineralization in a fluorine-poor system; the Trout Lake stockwork deposit, southeastern British Columbia, *in* Schroeter, T.G., ed., Porphyry deposits of the northwestern Cordillera, Canadian Institute of Mining, Metallurgy, and Petroleum Special Volume 46, Part D, p. 509–523

Lowell, D.J., and Guilbert, J.M., 1970, Lateral and vertical alteration-mineralization zoning in porphyry ore deposits: Economic Geology and the bulletin of the Society of Economic Geologists, v. 65, p. 373–408.

Lowenstern, J.B., and Sinclair, D.W., 1996, Exsolved magmatic fluid and its role in the formation of comb-layered quartz at the Cretaceous Logtung W-Mo deposit, Yukon Territory, Canada, *in* Brown, M., Candela, P.A., Peck, D.L., Stephens, W.E., Walker, R.J., and Zen, E., eds., The third Hutton symposium on the origin of granites and related rocks, Geological Society of America Special Paper, v. 315: College Park, Geological Society of America, p. 291–303.

Ludwig, K.R., 1991, ISOPLOT; a plotting and regression program for radiogenic-isotope data; version 2.53: U.S. Geological Survey Open File Report, OF 91-0445, p. 39.

Macauley, T.N., 2004, Technical Report on the Trout Lake Molybdenum Project Revelstoke Mining Division British Columbia Canada: Unpublished report, Roca Mines Inc., 16 p.

Maksaev, V., Munizaga, R., McWilliams, M.O., Fanning, C.M., Mathur, R.D., Ruiz, J., and Zentilli, M., 2004, New chronology for El Teniente, Chilean Andes, from U-Pb, ^{40}Ar/^{39}Ar, Re-Os, and fission track dating; Implications for the evolution of a super giant porphyry Cu-Mo deposit, *in* Sillitoe, R.H., Perello, J., and Vidal C.E., eds., Andean metallogeny; new discoveries, concepts, and updates, Society of Economic Geologists, Special Publication, v. 11: Littleton, the Society of Economic Geologists, p. 15–54.

Massey, N.W.D., MacIntyre, D.G., Desjardins, P.J., Cooney, R.T., 2005, Digital geology map of British Columbia; whole province: British Columbia Ministry of Energy, Mines and Petroleum Resources, Open-File 2005-02.

Matthews, W.H., 1983, Early Tertiary resetting of potassium-argon dates in the

Kootenay Arc, southeastern British Columbia: Canadian Journal of Earth Sciences, v. 20, p. 867–872.

Marsh, T.M., Einaudi, M.T., and McWilliams, M., 1997, $^{40}Ar/^{39}Ar$ Geochronology of Cu-Au and Au-Ag mineralization in the Potrerillos district, Chile. Economic Geology and the bulletin of the Society of Economic Geologists, v. 92, p. 784–806.

Miller, F.K., and Engels, J.C., 1975, Distribution and trends of discordant ages of the plutonic rocks of northeastern Washington and northern Idaho: Geological Society of America Bulletin, v. 86, p. 517–528.

McDonough, W.F., and Sun, S.S., 1995, The composition of the earth: Chemical Geology, v. 120, p. 223–253.

McDougall, I., and Harrison, T.M., 1988, Geochronology and thermochronology by the $^{40}Ar/^{39}Ar$ Method: Oxford, Oxford University Press, 212 p.

Monger, J.W.H., Souther, J.G., and Gabrielse, H., 1972, Evolution of the Canadian Cordillera; a plate-tectonic model: American Journal of Science, v. 272, p. 577–602.

Muraro, T.W., 1966, Metamorphism of zinc-lead deposits in southeastern British Columbia, *in* Gunning, H.C., White, W.H., Little, H.W., Armstrong, J.E., Yates, R.G., Ney, C.S., and Holland, S.S., eds., A symposium on the tectonic history and mineral deposits of the western Cordillera in British Columbia and neighboring parts of the United States, Canadian Institute of Mining and Metallurgy Special Volume 8: Montreal, Canadian Institute of Mining and Metallurgy, p. 249–262.

Mutschler, F., R, Wright, E., G, Ludington, S., and Abbott, J., T, 1981, Granite molybdenite systems: Economic Geology and the bulletin of the Society of Economic Geologists, v. 76, p. 874–897.

O'Brien, S., Irvine, G.J., and McCallum, S.I., 1991, Eocene potassic magmatism in the Highwood Mountains, Montana: petrology, geochemistry, and tectonic implications: Journal of Geophysical Research, v. 96, p. 13237–13260.

Padilla-Garza, R.A., Titley, S.R., and Eastoe, C., 2004, Hypogene evolution of the Escondida porphyry copper deposit, Chile, *in* Sillitoe, R.H., Perello, J., and Vidal C.E., eds., Andean metallogeny; new discoveries, concepts, and updates, Society of Economic Geologists, Special Publication v. 11: Littleton, the Society of Economic Geologists, p. 141–165.

Parent, M., 2001, Circle of Silver v. 4: Nakusp, Arrow Lakes Historical Society, 375 p.

Parrish, R.R., and Armstrong, R.L., 1987, The ca. 162 Ma Galena Bay Stock and its relationship to the Columbia River fault zone, southeast British Columbia: Geological Survey of Canada Radiogenic age and Isotopic Studies, v. 87-2, p. 25–32.

Parrish, R.R., and Wheeler, J.O., 1983, A U-Pb zircon age from the Kuskanax batholith, southeastern British Columbia: Canadian Journal of Earth Sciences, v. 20, p. 1751–1756.

Parrish, R.R., 1992, U-Pb ages of Jurassic-Eocene plutonic rocks in the vicinity of Valhalla complex, southeast British Columbia: Radiogenic Age and Isotopic Studies, report 5, Geological Survey of Canada Paper 91-2, p. 115–134.

Parry, W.T., 1986, Estimation of X_{CO_2}, P, and fluid inclusion volume from fluid inclusion temperature measurements in the system NaCl-CO_2-H_2O: Economic Geology and the bulletin of the Society of Economic Geologists, v. 81, p. 1009–1013.

Peacock, M.A., 1931, Classification of igneous rock series: Geology, v. 39, p. 54–67.

Pearce, J.A., Harris, N.B.W., and Tindle, A.G., 1984, Trace element discrimination diagrams for the tectonic interpretation of granitic rocks: Journal of Petrology, v. 25, p. 956–983.

Petrelli, M., Poli, G., Perugini, D., Peccerillo, A., 2005, PetroGraph; a new software to visualize, model, and present geochemical data in igneous petrology: Geochemistry, Geophysics, Geosystems - G^3, v. 6, p. 26.

Potter, R.W.I., 1977, Pressure corrections for fluid-inclusion homogenization temperatures based on the volumetric properties of the system NaCl-H_2O: Journal of Research of the U.S. Geological Survey, v. 5, p. 603–607.

Price, R.A., Monger, J.W.H., and Muller, J.E., 1981, Cordilleran Cross-Section Calgary to Victoria, *in* Thompson, R.I., and Cook, D.G., eds., Field Guides to Geology and Mineral Deposits, Calgary ‘81 Annual Meeting: Calgary, Geological Association of Canada, p. 261–334.

Psutka, J.F., Read, P.B., and Fyles, J.T., 1982, Stratigraphy, structure, and metamorphism; Trout Lake molybdenum deposit and vicinity: Unpublished Report, Geotex Consultants Ltd., 24 p.

Ray, G.E., Webster, I.C.L., and Ettlinger, A.D., 1995, The distribution of skarns in British Columbia and the chemistry and ages of their related plutonic rocks: Economic Geology and the bulletin of the Society of Economic Geologists, v. 90, p. 920–937.

Read, P.B., and Wheeler, J.O., 1975, Geology of Lardeau (West Half), British Columbia: Geological Survey of Canada, Open-File Report 288.

Richards, J.P., Noble, S.R., and Pringle, M.S., 1999, A revised late Eocene age for porphyry Cu magmatism in the Escondida area, northern Chile: Economic Geology and the bulletin of the Society of Economic Geologists, v. 94, p. 1231–1247.

Richards, J.P., 2003, Tectono-magmatic precursors for porphyry Cu-(Mo-Au) deposit formation: Economic Geology and the bulletin of the Society of Economic Geologists, v. 98, p. 1515–1533.

Richards, J.P., and Kerrich R., 2007, Adakite-like rocks; their diverse origins and questionable role in metallogenesis: Economic Geology and the bulletin of the Society of Economic Geologists, v. 102, p. 537–576.

Roback, R.C., 1993, Late Paleozoic to Middle Mesozoic Tectonic Evolution of the Kootenay Arc, Northeastern Washington and Southeastern British Columbia: Unpublished PhD thesis, Austin, The University of Texas at Austin.

Roedder, E., 1984, Fluid Inclusions: Reviews in Mineralogy, v. 12: Washington D.C., Mineralogical Society of America, 644 p.

Roedder, E., and Bodnar, R.J., 1980, Geologic pressure determinations from inclusion studies: Annual Review of Earth and Planetary Sciences, v. 8, p. 263–301.

Samson, I.M., 1985, Some applications of Raman spectroscopy to the study of fluid and solid inclusions in minerals: Montreal Mineral Exploration Research Institute Research Paper 85-03, 35 p.

Scott, J.E., Richards, J.P., Heaman, L.M., Creaser, R.A., and Salazar, G.S., 2008, The Schaft Creek Porphyry Cu-Mo-(Au) Deposit, Northwestern British Columbia: Exploration and Mining Geology, v. 17, p. 163–196.

Seedorff, E., 1988, Cyclic development of hydrothermal mineral assemblages related to multiple intrusions at the Henderson porphyry molybdenum deposit, Colorado, *in* Taylor, R.P., and Strong, D.F., eds., Recent Advances in the Granite-related Mineral Deposits, Canadian Institute of Mining and Metallurgy Special Volume 39: Montreal, Canadian Institute of Mining and Metallurgy, p. 367–393.

Seedorff, E., Dilles, J.H., Proffett, J.M., Einaudi, M.T., Zurcher, L., Stavast, W.J.A., Johnson, D.A., and Barton, M.D., 2005, Porphyry deposits: characteristics and origin of hypogene features, *in* Hedenquist, J.W., Thompson, J.F.H., Goldfarb, R.J., and Richards, J.P., eds., Economic Geology, 100th Anniversary Volume: Littleton, Society of Economic Geologists, p. 251–298.

Selby, D., and Creaser, R.A., 2001, Re-Os geochronology and systematics in molybdenite from the Endako porphyry molybdenum deposit, British Columbia, Canada: Economic Geology and the bulletin of the Society of Economic Geologists, v. 96, p. 197–204.

—, 2004, Macroscale NTIMS and microscale LA-MC-ICP-MS Re-Os isotopic analysis of molybdenite; testing spatial restrictions for reliable Re-Os age determinations, and implications for the decoupling of Re and Os within molybdenite: Geochimica et Cosmochimica Acta, v. 68, p. 3897–3908.

Selby, D., Nesbitt, B.E., Muehlenbachs, K., and Prochaska, W., 2000, Hydrothermal alteration and fluid chemistry of the Endako porphyry molybdenum deposit, British Columbia: Economic Geology and the bulletin of the Society of Economic Geologists, v. 95, p. 183–201.

Shannon, J.R., Walker, B.M., Carten, R.B., and Geraghty, E.P., 1982, Unidirectional solidification textures and their significance in determining relative ages of intrusions at the Henderson Mine, Colorado: Geology (Boulder), v. 10, p. 293–297.

Shaver, S.A., 1984, Origin of differences between Climax-type and quartz monzonite-type porphyry moly deposits: The Geological Society of America, Rocky Mountain Section, 37th annual meeting, Abstracts with Programs, v. 16: Colorado, Geological Society of America, p. 254.

Sidorov, A.A., 2006, Relation between porphyry deposits and their vein satellites: Doklady Earth Sciences, v. 409, p. 859–863.

Simmons, S.F., and Brown, K.L., 2007, The flux of gold and related metals through a volcanic arc, Taupo Volcanic Zone, New Zealand: Geology (Boulder), v. 35, p. 1099–1102.

Sillitoe, R.H., 1980, Types of porphyry molybdenum deposits: Mining Magazine, v. 142, p. 550–553.

Simonetti, A., Heaman, L.M., Hartlaub, R.P., Creaser, R.A., MacHattie, T.G., and Bohm, C., 2005, U-Pb zircon dating by laser ablation-MC-ICP-MS using a new multiple ion counting Faraday collector array: Journal of Analytical Atomic Spectrometry, v. 20, p. 677–686.

Sinclair, A.J., 1966, Anomalous leads from the Kootenay Arc, *in* Gunning, H.C., White, W.H., Little, H.W., Armstrong, J.E., Yates, R.G., Ney, C.S., and Holland, S.S., eds., A symposium on the tectonic history and mineral deposits of the western Cordillera in British Columbia and neighboring parts of the United States, Canadian Institute of Mining and Metallurgy Special Volume 8: Montreal, Canadian Institute of Mining and Metallurgy, p. 249–262.

Smith, M.T., and Gehrels, G.E., 1992, Structural geology of the Lardeau Group near Trout Lake, British Columbia: implications for the structural evolution of the Kootenay Arc: Canadian Journal of Earth Sciences, v. 29, p. 1305–1319.

Smoliar, M.I., Walker, R.J., and Morgan, J.W., 1996, Re-Os ages of group IIA, IIIA, IVA, and IVB iron meteorites: Science, v. 271, p. 1099–1102.

Soregaroli, A.E., 1975, Geology and genesis of the Boss Mountain molybdenum deposit, British Columbia: Economic Geology and the bulletin of the Society of Economic Geologists, v. 70, p. 4–14.

Soregaroli, A.E., and Sutherland Brown, A., 1976, Characteristics of Canadian Cordilleran molybdenum deposits, *in* Sutherland Brown, A., ed., Porphyry Deposits of the Canadian Cordillera, Canadian Institute of Mining and Metallurgy Special Volume 15: Montreal, Canadian Institute of Mining and Metallurgy, p. 417–431.

Spooner, E.T.C., 1981, Fluid Inclusion studies of hydrothermal ore deposits, *in* Hollister, L.S., and Crawford, M.L., eds., Fluid Inclusions: Applications to Petrology, Volume 6: Toronto, Mineralogical Association of Canada, p. 209–240.

Stacey, J.S., and Kramers, J.D., 1975, Approximation of terrestrial lead isotope evolution by a two-stage model: Earth and Planetary Science Letters, v. 26, p. 207–221.

Stein, H.J., 1988, Genetic traits of Climax-type granites and molybdenum mineralization, Colorado mineral belt, *in* Taylor, R.P., and Strong, D.F., eds., Recent advances in the geology of granite-related mineral deposits, Canadian Institute of Mining and Metallurgy Special Volume 39:

Montreal, Canadian Institute of Mining and Metallurgy, p. 394–401.

Stein, H., Markey, R., Morgan, J., Hannah, J.L., and Schersten, A., 2001, The remarkable Re–Os chronometer in molybdenite; how and why it works: Terra Nova, v. 13, p. 479–486.

Stein, H.J., and Crock, J.G., 1990, Late-Cretaceous-Tertiary magmatism in the Colorado Mineral Belt; Rare earth element and samarium-neodymium isotopic studies, *in* Anderson, J.L., ed., The nature and origin of Cordilleran magmatism, Geological Society of America Memoir, v. 174: Boulder, Colorado, Geological Society of America, p. 195–223.

Steininger, R.C., 1985, Geology of the Kitsault molybdenum deposit, British Columbia: Economic Geology and the bulletin of the Society of Economic Geologists, v. 80, p. 57–71.

Sun, S.S., McDonough, W.F., 1989, Chemical and isotopic systematics of ocean basalts; implications for mantle composition and processes, *in* Saunders A.D., and Norry M.J., eds., Magmatism in ocean basin, Geologic Society of London, special publication, v. 42, 313–345.

Sutherland Brown, A., 1969, Mineralization in British Columbia and the copper and molybdenum deposits: Canadian Mining Metallurgical Bulletin, v. 61, p. 26–40.

Taylor, C.D., Winick, J.A., Unruh, D.M., and Kunk, M.J., 2007, Earth science studies in support of public policy development and land stewardship - Headwaters Province Idaho and Montana: U.S. Department of the Interior U.S. Geological Survey, Circular 1305, 102 p.

Titley, S.R., and Hicks, C.L., 1966, Geology of the porphyry copper deposits southwestern North America: Tucson, The University of Arizona Press, 287 p.

Tosdal, R.M., and Richards, J.P., 2004, Magmatic and structural controls on the development of porphyry Cu ± Mo ± Au deposits, *in* Richards J.P., Tosdal R.M., eds., Structural controls on ore genesis, Reviews in Economic Geology, v. 14: Littleton, Society of Economic Geologists, p. 157–181.

Touret, J., 1977, The significance of fluid inclusions in metamorphic rocks, *in* Fraser, D.G., eds., Thermodynamics in geology, Proceedings of the NATO Advanced Study Institute: Dordrecht, Reidel, p. 203–227.

Villeneuve, M.E., Whalen, J.B., Anderson, R.G., and Struik, L.C., 2001, The Endako Batholith; episodic plutonism culminating in formation of the

Endako molybdenite deposit, north-central British Columbia: Economic Geology and the bulletin of the Society of Economic Geologists, v. 96, p. 171–196.

Walker, J.F., Bancroft, M.F., and Gunning, H.C., 1929, Lardeau map-area, British Columbia: Geological Survey of Canada Memoir, v. 161, 142 p.

Wallace, S.R., 1995, The Climax-type molybdenite deposits: What they are, where they are, and why they are: Economic Geology and the bulletin of the Society of Economic Geologists, v. 90, p. 1359–1380.

Westra, G., and Keith, S.B., 1981, Classification and genesis of stockwork molybdenum deposits: Economic Geology and the bulletin of the Society of Economic Geologists, v. 76, p. 844–873.

Whalen, J.B., Anderson R.G., Struik, L.C., and Villeneuvem M.E., 2001, Geochemistry and Nd isotopes of the Francois Lake plutonic suite, Endako Batholith, host and progenitor to the Endako molybdenum camp, central British Columbia: Canadian Journal of Earth Science, v. 38, p. 603–618.

Wheeler, J.O., and McFeely P., 1991, Tectonic assemblage map of the Canadian Cordillera and adjacent parts of the United States: Geological Survey of Canada, “A” Series Map, Report 1712A, 1 sheet.

White, A.J.R., and Chappell, B.W., 1977, Ultrametamorphism and granitoid genesis: Tectonophysics, v. 43, p. 7–22.

—, 1983, Granitoid types and their distribution in the Lachlan fold belt, southeastern Australia: Geological Survey of Canada Memoir, v. 159, p. 21–34.

White, W.H., Bookstrom, A.A., Kamilli, R.J., Ganster, M.W., Smith, R.P., Ranta, D.E., and Steininger, R.C., 1981, Character and origin of Climax-type molybdenum deposits, *in* Skinner, B.J., ed., Economic Geology, 75th Anniversary Volume: Littleton, Economic Geologic Publishing Company, p. 270–316.

Wilkinson, J.J., 2001, Fluid inclusions in hydrothermal ore deposits: Lithos, v. 55, p. 229–272.

Winter, J.D., 2001, An introduction to igneous and metamorphic petrology: New York, Prentice Hall, 699 p.

Worthington, J.E., 2007, Porphyry and other molybdenum deposits of Idaho and Montana: Idaho Geological Survey Technical Report 07-3, 22 p.

Yardley, B.W.D., 2005, Metal concentrations in crustal fluids and their relationship to ore formation, *in* Hedenquist, J.W., Thompson, J.F.H., Goldfarb, R.J., and Richards, J.P., eds., Economic Geology, 100th Anniversary Volume: Littleton, Society of Economic Geologists, p. 613–632.

Zartman, R.E., and Stacey, J.S., 1971, Lead isotopes and Mineralization ages in belt Supergroup rocks, northwestern Montana and northern Idaho: Economic Geology and the bulletin of the Society of Economic Geologists, v. 66, p. 849–860.

Appendix A: Sample Location

Sample ID	Type	Location Description	Collar Coordinate Northing[6]	Collar Coordinate Easting[6]	Used for:	Brief Sample Description
CL100	Grab	920L	-	-	Re-Os[3]	Molybdenite stringers within granodiorite from high-grade zone on 920L. Molybdenite stringers are crosscut by stockwork quartz veins. Molybdenite dated using Re-Os to determine the timing of the high-grade zone. Granodiorite is strongly silicified.
CL200	Core	DDH-05-12 318 feet Azimuth = 256° Dip = -61°	2743	2983	Re-Os	Quartz + feldspar vein with coarse Mo on selvages. Sample taken for Re-Os dating.
CL300	Grab	920L	-	-	Re-Os	Molybdenite and muscovite intergrown. From high-grade zone on 920L. Molybdenite–muscovite intergrowths are within stockwork quartz vein crosscutting high-grade zone. Re-Os molybdenite date will be compared with Ar-Ar date of muscovite (sample TL303).
TL11	Core	DDH-05-05 127 feet Azimuth = 238° Dip = -20°	2722	2983	FI[1]	Mo-bearing quartz vein crosscutting Mo-bearing quartz vein
TL120	Core	MX07-03 1349 meters Azimuth = 220° Dip = -74°	2859	3101	FI	Pb-Zn-Ag vein crosscuts granodiorite. Propylitic alteration halo.
TL121	Core	MX07-03 656 meters Azimuth = 220° Dip = -74°	2859	3101	FI	Pb-Zn-Ag vein crosscuts granodiorite. Propylitic alteration halo.
TL122	Core	MX07-03 668 meters Azimuth = 220° Dip = -74°	2859	3101	FI	Pb-Zn-Ag vein crosscuts granodiorite. Propylitic alteration halo.

Appendix A: Sample Location cont'd.

Sample ID	Type	Location Description	Collar Coordinate Northing[6]	Collar Coordinate Easting[6]	Used for:	Brief Sample Description
TL123	Core	MX07-03 723 meters Azimuth = 220° Dip = -74°	2859	3101	FI	Pb-Zn-Ag vein crosscuts granodiorite. Propylitic alteration halo.
TL85	Core	MX07-03 85 meters Azimuth = 220° Dip = -74°	2859	3101	GC[2]	Granodiorite. Taken from east side of the Z-fault. Barren. Equigranular. Rare coarse muscovite. Minor phyllic alteration. Slight reaction with HCl. Plagioclase rich. <10% biotite. Light grey. Massive.
TL95	Core	MX07-04 401 meters Azimuth = 238° Dip = -57°	2859	3101	GC	Aplite. Massive. Narrow dike. Crosscuts granodiorite. Sugary texture. Cream color. No biotite. Abundant fine grained K feldspar. Graphic texture.
TL126	Core	MX07-04 730 meters Azimuth = 238° Dip = -57°	2859	3101	FI	Pb-Zn-Ag vein crosscuts granodiorite. Propylitic alteration halo.
TL98	Core	MX07-04-399 meters Azimuth = 238° Dip = -57°	2859	3101	GC	Trondhjemite. Distinct light grey color and 5 mm plag phenocrysts. No quartz phenocrysts. Massive. Crosscut by Mo mineralized quartz veins. Crosscuts tonalite dike. No feldspar. May not be a new phase... may be altered granodiorite?
TL128	Core	MX07-05 709 meters Azimuth = 204° Dip = -70°	2722	2983	FI	Pb-Zn-Ag vein crosscuts granodiorite. Propylitic alt halo.
TL129	Core	MX07-05 709 meters Azimuth = 204° Dip = -70°	2722	2983	FI	Pb-Zn-Ag vein crosscuts granodiorite. Propylitic alt halo.

Appendix A: Sample Location cont'd.

Sample ID	Type	Location Description	Collar Coordinate Northing[6]	Collar Coordinate Easting[6]	Used for:	Brief Sample Description
TL201	Grab	960L	-	-	U-Pb[4]	Intermineral dike (same as TL300, TL88). Granodiorite. Taken near mechanic shop on 960L. Crosscut by mineralized quartz veins and is crosscut by mineralized quartz veins. <10% partly chloritized biotite. Light grey. Porphyritic with 5 mm quartz phenocrysts. Slightly silicified. Minor potassic alteration. Plagioclase rich matrix.
TL202	Core	MAX07-03 1323 meters Azimuth = 220° Dip = -74°	2859	3101	U-Pb	Granodiorite (same as TL302). Equigranular to porphyritic with rare quartz phenocrysts. Light grey. <10% partly chloritized biotite. Rare K feldspar. Plagioclase rich matrix. Massive.
TL26	Core	MM04-02 1226 feet Azimuth = 210° Dip = -60°	3098	2962	FI	Distant Mo-bearing vein. Compare chemistry to high-grade zone.
TL300	Grab	960L	-	-	Ar-Ar[5]	Intermineral dike. Granodiorite. Biotite mineral separate. Taken near mechanic shop on 960L. Crosscut by mineralized quartz veins and is crosscut by mineralized quartz veins. <10% partly chloritized biotite. Light grey. Porphyritic with 5 mm quartz phenocrysts. Slightly silicified. Minor potassic alteration. Plagioclase rich matrix.
TL301	Core	MX07-02 543.4 meters Azimuth = 227° Dip = -62°	2859	3101	Ar-Ar	Biotite-molybdenite intergrowths potassic alteration in quartz vein. Biotite mineral separate.

Appendix A: Sample Location cont'd.

Sample ID	Type	Location Description	Collar Coordinate Northing[6]	Collar Coordinate Easting[6]	Used for:	Brief Sample Description
TL302	Core	MAX07-03 1323 meters Azimuth = 220° Dip = -74°	2859	3101	Ar-Ar	Granodiorite (same as TL202). Biotite mineral separate. Equigranular to porphyritic with rare quartz phenocrysts. Light grey. <10% partly chloritized biotite. Rare K feldspar. Plagioclase rich matrix. Massive. Average grain size <1mm.
TL303	Grab	920L	-	-	Ar-Ar	Muscovite-molybdenite intergrowths from high-grade zone. Muscovite mineral separate will be dated using Ar-Ar. Compare against Re-Os in molybdenite (TL300). Quartz vein crosscuts Mo stringers in high-grade zone.
TL304	Core	MX07-03 723 meters Azimuth = 220° Dip = -74°	2859	3101	Ar-Ar	Sphalerite and galena vein. Crosscutting granodiorite. Associated with propylitic alteration halo. Muscovite separate.
TL4	Core	DDH-05-15 406 feet Azimuth = 252° Dip = -59°	2742	2983	FI	Mo-bearing quartz vein crosscutting Mo-bearing quartz vein
TL57	Grab	950L	-	-	FI	Sheeted quartz veins from high-grade zone on 950L. Hundreds of quartz veins with Mo selvages. Sheeted quartz veins crosscut Mo stringers and are in turn crosscut by stockwork veins.
TL58	Grab	950L	-	-	FI	High-grade Mo veins. Quartz vein stockwork in high-grade zone. Hosted by granodiorite. Taken from exposure on 950L ore drift.
TL6	Core	DDH05-10 141 feet Azimuth = 247° Dip = -60°	2781	2983	FI	Mo-bearing quartz vein. Crosscutting barren quartz vein.

Appendix A: Sample Location cont'd.

Sample ID	Type	Location Description	Collar Coordinate Northing[6]	Collar Coordinate Easting[6]	Used for:	Brief Sample Description
TL80	Grab	Galena Bay stock	-	-	GC	438067, 5606986 (UTM, NAD27, ZONE 11) Biotite hornblende granite.
TL81	Grab	Galena Bay stock	-	-	GC	438002, 5604736 (UTM, NAD27, ZONE 11) Biotite hornblende granite.
TL82	Grab	Kuskanax batholith	-	-	GC	435895, 5604736 (UTM, NAD27, ZONE 11) Biotite hornblende granite.
TL83	Grab	Kuskanax batholith	-	-	GC	435895, 559341 (UTM, NAD27, ZONE 11) Biotite hornblende granite.
TL84	Grab	950L	-	-	GC	Narrow granodiorite dyke that crosscuts mineralized quartz veins in ore drift at 950L. Porphyritic with quartz phenocrysts. ~10% biotite, partly chloritized. Light grey. Minor K feldspar. Plag rich groundmass.
TL86	Core	MX07-01 641 meters Azimuth = 231° Dip = -45°	2859	3100	GC	Biotite quartz diorite. Extremely biotite rich >30%. Black and white. Color is very distinct. Narrow dyke crosscut by tonalite. Virtually no K feldspar. Porphyritic with 5 mm plag phenocrysts.
TL87	Grab	950L	-	-	GC	Granodiorite. Host of high grade mineralization. Taken from ore drift ore-drift on 950L. Crosscut by mineralized quartz veins. Porphyritic. Intense silicification and potassic alteration. Silicic post overprints potassic. <10% partly chloritized biotite.

Appendix A: Sample Location cont'd.

Sample ID	Type	Location Description	Collar Coordinate Northing[6]	Collar Coordinate Easting[6]	Used for:	Brief Sample Description
TL88	Grab	960L	-	-	GC	Intermineral dike. Granodiorite. Taken near mechanic shop on 960L. Crosscut by mineralized quartz veins and is crosscut by mineralized quartz veins. <10% partly chloritized biotite. Light grey. Porphyritic with 5 mm quartz phenocrysts. Slightly silicified, minor potassic alteration. Plagioclase rich matrix.
TL89	Core	MM04-01 14 feet Azimuth = 215° Dip = -70°	3061	2908	GC	Altered granodiorite. Muscovite rich. Intense and pervasive phyllic alteration. Strong reaction with acid. Light grey. Porphyritic with 5-10 mm quartz phenocrysts.
TL90	Grab	960L	-	-	GC	Granodiorite. Sampled from 960L east of Z-fault. Equigranular. Muscovite throughout. 10% chloritized biotite. White and black. Crosscut by aplite and mineralized quartz veins. Plagioclase rich matrix.
TL91	Core	MM04-01 780 feet Azimuth = 215° Dip = -70°	3061	2908	GC	Aplite. White. Mostly K feldspar and quartz. Coarse muscovite throughout. Corse pyrite throughout. Massive. Sugary texture.
TL92	Grab	MM04-01 0 feet Azimuth = 215° Dip = -70°	3061	2908	GC	Granodiorite. Thick weathering rind. Equigranular to porphyritic. Massive. Black/white. <10% partly chloritized biotite. Plagioclase rich matrix. Minor K feldspar. Rare molybdenite disseminated.
TL93	Core	MX07-03 1313 meters Azimuth = 220° Dip = -74°	2859	3101	GC	Granodiorite (same as TL202 and TL302). Equigranular to porphyritic with rare quartz phenocrysts. Light grey. <10% partly chloritized biotite. Rare K feldspar. Plagioclase rich matrix. Massive. Average grain size <1mm.

Appendix A: Sample Location cont'd.

Sample ID	Type	Location Description	Collar Coordinate Northing[6]	Collar Coordinate Easting[6]	Used for:	Brief Sample Description
TL94	Core	MM04-02 329 meters Azimuth = 210° Dip = -60°	3098	2962	GC	Biotite Tonalite. Dark grey. Crosscut granodiorite and is crosscut by mineralized quartz veins. 10% biotite, looks fresh. Porphyritic with 10 mm quartz phenocrysts. Massive. Color is distinct.
TL96	Grab	960L	-	-	GC	Biotite tonalite. Taken from from 960L at mechanic shop. Crosscuts granodiorite. Intermineral. Dark grey. 10% biotite. Very little alteration.
TL97	Core	MM04-01 336 meters Azimuth = 215° Dip = -70°	3061	2908	GC	Biotite quartz diorite. Black and white. Extremely biotite rich...>30%. Coarse 1-5 mm plagioclase phenocrysts. Crosscut by mineralized quartz feldspar veins. Rare K-feldspar. Very distinct unit. Narrow dyke.
TL99	Grab	960L	-	-	GC	Aplite dike. Taken from 2nd crosscut on 960L. Crosscuts granodiorite. Intermineral. Cream colored. No biotite. Coarse muscovite. Graphic texture. Massive. Sugary texture. Essentially composed of K feldspar and quartz.

[1] FI = fluid inclusion sample

[2] GC = lithogeochemical sample

[3] Re-Os = Re–Os geochronology sample

[4] U-Pb = U–Pb geochronology sample

[5] Ar-Ar = Ar–Ar geochronology sample

[6] Collar coordinates are relative to mine grid

Appendix A: Sample Location cont'd.

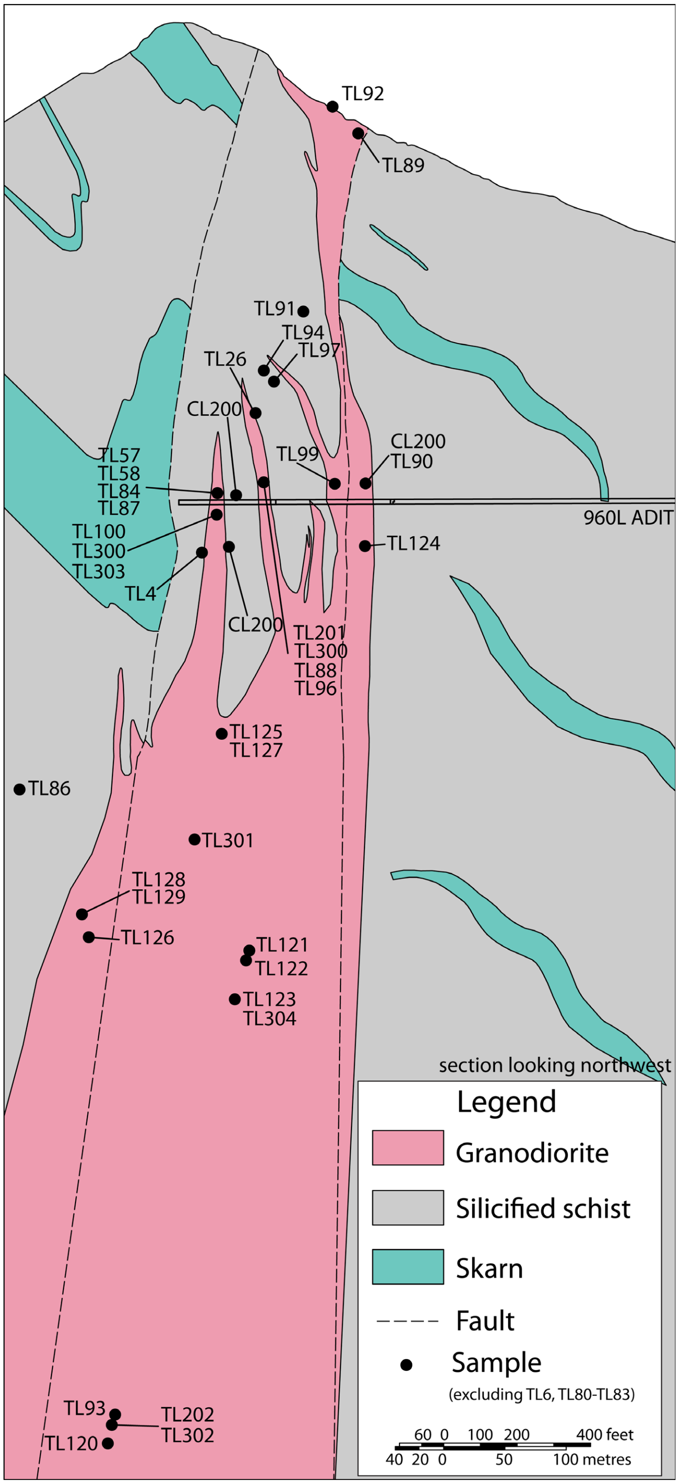

Figure 43. Geologic cross section of MAX showing approximate location of fluid inclusion geochronology, and geochemistry samples (modified from Boyle and Leitch, 1983).

Appendix B: U-Pb data for sample TL201

Grain ID	^{206}Pb (cps)	^{204}Pb (cps)	^{206}Pb/^{238}U	2σ error	^{207}Pb/^{235}U	2σ error	^{207}pb/^{206}pb	2σ error	rho	^{206}Pb/^{238}U AGE (Ma)	2σ error (Ma)	^{207}Pb/^{235}U AGE (Ma)	2σ error (Ma)
TL201-1	112112	0	0.01236	0.00198	0.08426	0.01372	0.04945	0.00149	0.983	79	13	82	13
TL201-2	243046	163	0.03703	0.00300	0.31552	0.02896	0.06180	0.00268	0.881	234	19	278	22
TL201-3	204188	149	0.05156	0.00303	0.84385	0.06607	0.11871	0.00615	0.750	324	19	621	36
TL201-4	34197	0	0.01257	0.00198	0.08836	0.01600	0.05098	0.00455	0.870	81	13	86	15
TL201-5	219742	117	0.03755	0.00265	0.29324	0.02850	0.05665	0.00379	0.725	238	16	261	22
TL201-6	27438	0	0.01257	0.00198	0.09099	0.08030	0.05251	0.04559	0.179	81	13	88	72
TL201-7	90527	0	0.01215	0.00198	0.08618	0.02164	0.05144	0.00984	0.648	78	13	84	20
TL201-8	75495	0	0.01234	0.00198	0.09342	0.04870	0.05489	0.02723	0.307	79	13	91	44
TL201-9	136652	0	0.01259	0.00198	0.09166	0.01465	0.05279	0.00150	0.984	81	13	89	14
TL201-10	90158	143	0.01945	0.00219	0.14354	0.02188	0.05351	0.00550	0.738	124	14	136	19
TL201-11	67445	0	0.01223	0.00198	0.08271	0.01680	0.04905	0.00603	0.796	78	13	81	16
TL201-12	156655	0	0.01195	0.00198	0.08087	0.01385	0.04910	0.00219	0.966	77	13	79	13
TL201-13	135996	0	0.01236	0.00198	0.09186	0.01676	0.05391	0.00472	0.877	79	13	89	15
TL201-14	318901	206	0.04628	0.00285	0.60648	0.05488	0.09505	0.00629	0.681	292	18	481	34
TL201-15	152763	0	0.01231	0.00198	0.08660	0.03292	0.05103	0.01758	0.423	79	13	84	30
TL201-16	106467	135	0.03573	0.00272	0.24188	0.02281	0.04910	0.00272	0.809	226	17	220	18
TL201-17	44890	0	0.01209	0.00198	0.08652	0.04236	0.05192	0.02396	0.334	77	13	84	39
TL201-18	64284	0	0.01865	0.00213	0.13840	0.26467	0.05383	0.10277	0.060	119	13	132	212
TL201-19	40111	0	0.01314	0.00198	0.08971	0.01365	0.04951	0.00097	0.992	84	13	87	13
TL201-20	219569	139	0.05203	0.00263	0.53386	0.03083	0.07442	0.00207	0.876	327	16	434	20
TL201-21	67818	0	0.01172	0.00197	0.07951	0.01348	0.04921	0.00092	0.994	75	13	78	13
TL201-22	63037	0	0.01212	0.00198	0.08240	0.01356	0.04930	0.00110	0.991	78	13	80	13
TL201-23	25187	0	0.01296	0.00198	0.10270	0.02359	0.05745	0.00986	0.665	83	13	99	21
TL201-24	21487	0	0.01221	0.00198	0.08613	0.04384	0.05118	0.02470	0.318	78	13	84	40
TL201-25	175625	95	0.02916	0.00236	0.46418	0.05338	0.11547	0.00945	0.703	185	15	387	36
TL201-26	33154	0	0.01348	0.00199	0.11213	0.02595	0.06032	0.01074	0.639	86	13	108	23

Appendix B: U-Pb data for sample TL201 cont'd.

Grain ID	^{206}Pb (cps)	^{204}Pb (cps)	^{206}Pb/^{238}U	2σ error	^{207}Pb/^{235}U	2σ error	^{207}pb/^{206}pb	2σ error	rho	^{206}Pb/^{238}U AGE (Ma)	2σ error (Ma)	^{207}Pb/^{235}U AGE (Ma)	2σ error (Ma)
TL201-27	175609	128	0.11554	0.00704	1.48549	0.09690	0.09325	0.00217	0.934	705	41	924	39
TL201-28	229176	125	0.02323	0.00221	0.22091	0.02536	0.06896	0.00443	0.828	148	14	203	21
TL201-29	48122	0	0.01185	0.00198	0.07923	0.01390	0.04848	0.00265	0.950	76	13	77	13
TL201-30	131172	0	0.01219	0.00198	0.08203	0.01352	0.04879	0.00144	0.984	78	13	80	13
TL201-31	186560	0	0.01226	0.00198	0.09913	0.01679	0.05865	0.00303	0.952	79	13	96	15
TL201-32	87979	0	0.01186	0.00198	0.08003	0.02092	0.04894	0.00986	0.637	76	13	78	19
TL201-33	75318	0	0.01223	0.00198	0.08235	0.02781	0.04883	0.01447	0.479	78	13	80	26
TL201-34	134326	0	0.01159	0.00197	0.07864	0.01353	0.04923	0.00117	0.990	74	13	77	13
TL201-35	106725	0	0.01201	0.00198	0.08207	0.01370	0.04957	0.00141	0.985	77	13	80	13
TL201-36	48137	0	0.01340	0.00199	0.09677	0.02630	0.05240	0.01193	0.546	86	13	94	24
TL201-37	230491	0	0.01215	0.00198	0.08451	0.01398	0.05043	0.00153	0.983	78	13	82	13
TL201-38	50813	0	0.01233	0.00198	0.08427	0.01437	0.04957	0.00286	0.941	79	13	82	13
TL201-39	258357	167	0.08686	0.00582	1.09090	0.09760	0.09109	0.00541	0.748	537	34	749	46
TL201-40	250150	169	0.02955	0.00224	0.27907	0.02229	0.06849	0.00171	0.950	188	14	250	18
TL201-41	26622	0	0.01254	0.00198	0.09074	0.05562	0.05246	0.03108	0.257	80	13	88	51
TL201-40-1	298070	0	0.01178	0.00197	0.07913	0.01453	0.04873	0.00365	0.913	75	13	77	14
TL201-42	125608	130	0.05495	0.00275	0.48097	0.02983	0.06348	0.00233	0.806	345	17	399	20
TL201-43	19758	0	0.01478	0.00205	0.16272	0.06779	0.07986	0.03137	0.333	95	13	153	58
TL201-44	14717	0	0.01263	0.00198	0.08323	0.02256	0.04781	0.01057	0.578	81	13	81	21
TL201-45	13422	0	0.01243	0.00198	0.08802	0.06924	0.05137	0.03957	0.202	80	13	86	63
TL201-46	10525	0	0.01279	0.00198	0.08883	0.05247	0.05036	0.02870	0.262	82	13	86	48
TL201-47	75662	0	0.01251	0.00198	0.08602	0.02169	0.04987	0.00979	0.627	80	13	84	20
TL201-48	77857	0	0.01276	0.00198	0.09131	0.09987	0.05190	0.05619	0.142	82	13	89	89
TL201-49	54948	0	0.01211	0.00198	0.08208	0.01362	0.04915	0.00147	0.984	78	13	80	13
TL201-50	13943	0	0.01252	0.00198	0.08793	0.06470	0.05095	0.03661	0.215	80	13	86	59
TL201-51	7836	0	0.01310	0.00198	0.08819	0.02417	0.04882	0.01116	0.552	84	13	86	22

Appendix B: U-Pb data for sample TL201 cont'd.

Grain ID	^{206}Pb (cps)	^{204}Pb (cps)	^{206}Pb/^{238}U	2σ error	^{207}Pb/^{235}U	2σ error	^{207}pb/^{206}pb	2σ error	rho	^{206}Pb/^{238}U AGE (Ma)	2σ error (Ma)	^{207}Pb/^{235}U AGE (Ma)	2σ error (Ma)
TL201-52	18321	0	0.01281	0.00198	0.08704	0.03979	0.04929	0.02121	0.338	82	13	85	37
TL201-53	16670	0	0.01227	0.00198	0.08163	0.02028	0.04826	0.00912	0.649	79	13	80	19
TL201-54	68226	0	0.01272	0.00198	0.08728	0.01372	0.04976	0.00111	0.990	81	13	85	13
TL201-55	27950	0	0.01485	0.00202	0.11149	0.09493	0.05447	0.04578	0.160	95	13	107	83
TL201-56	68875	0	0.02624	0.00235	0.21694	0.97947	0.05997	0.27070	0.020	167	15	199	600
TL201-57	80723	0	0.01294	0.00198	0.08847	0.01574	0.04960	0.00448	0.861	83	13	86	15
TL201-58	57103	0	0.01277	0.00198	0.08637	0.01365	0.04906	0.00149	0.981	82	13	84	13
TL201-59	21943	0	0.01397	0.00199	0.13175	0.19684	0.06839	0.10171	0.095	89	13	126	163
TL201-60	19434	0	0.01305	0.00198	0.09400	0.05636	0.05222	0.03030	0.253	84	13	91	51
TL201-61	31546	0	0.01376	0.00199	0.08923	0.03208	0.04702	0.01548	0.402	88	13	87	29
TL201-62	16119	0	0.01245	0.00198	0.08477	0.01845	0.04938	0.00735	0.730	80	13	83	17
TL201-63	23076	0	0.01316	0.00198	0.09607	0.05013	0.05296	0.02646	0.289	84	13	93	45
TL201-64	136048	147	0.07722	0.00356	0.84300	0.04786	0.07917	0.00263	0.812	480	21	621	26
TL201-65	93700	0	0.01210	0.00198	0.08189	0.01348	0.04910	0.00100	0.992	78	13	80	13
TL201-66	20714	0	0.01280	0.00198	0.08785	0.03025	0.04979	0.01532	0.450	82	13	85	28
TL201-67	28456	0	0.01305	0.00198	0.11206	0.09252	0.06229	0.05056	0.184	84	13	108	81
TL201-68	27814	0	0.01723	0.00228	0.14713	0.99815	0.06195	0.42017	0.019	110	14	139	636
TL201-69	124705	158	0.03784	0.00279	0.33634	0.04328	0.06447	0.00680	0.573	239	17	294	32
TL201-70	123458	163	0.04476	0.00248	0.38342	0.02410	0.06213	0.00185	0.880	282	15	330	18
TL201-71	124778	0	0.01264	0.00198	0.08562	0.01372	0.04913	0.00165	0.978	81	13	83	13
TL201-72	20201	0	0.01260	0.00198	0.08205	0.02650	0.04723	0.01332	0.487	81	13	80	25
TL201-73	68383	0	0.01254	0.00198	0.08576	0.05065	0.04959	0.02822	0.267	80	13	84	46
TL201-74	74306	0	0.01244	0.00198	0.08871	0.01491	0.05171	0.00281	0.946	80	13	86	14
TL201-75	22206	0	0.01480	0.00199	0.27600	0.30555	0.13525	0.14861	0.122	95	13	247	218
TL201-76	13270	0	0.01259	0.00198	0.09368	0.05406	0.05396	0.02996	0.272	81	13	91	49
TL201-77	68001	139	0.03827	0.00343	0.24430	0.02908	0.04629	0.00363	0.752	242	21	222	23

Appendix B: U-Pb data for sample TL201 cont'd

Grain ID	^{206}Pb (cps)	^{204}Pb (cps)	^{206}Pb/^{238}U	2σ error	^{207}Pb/^{235}U	2σ error	^{207}pb/^{206}pb	2σ error	rho	^{206}Pb/^{238}U AGE (Ma)	2σ error (Ma)	^{207}Pb/^{235}U AGE (Ma)	2σ error (Ma)
TL201-80	162078	195	0.09363	0.00463	0.76514	0.05707	0.05927	0.00331	0.663	577	27	577	32
TL201-79	14636	0	0.01238	0.00198	0.10025	0.10786	0.05874	0.06250	0.149	79	13	97	95
TL201-80	47083	0	0.02503	0.00224	0.22983	0.03820	0.06660	0.00933	0.539	159	14	210	31
TL201-81	13190	0	0.01309	0.00198	0.08675	0.05832	0.04808	0.03149	0.225	84	13	84	53
TL201-82	12010	0	0.01307	0.00198	0.09127	0.09019	0.05064	0.04945	0.153	84	13	89	81
TL201-83	91403	0	0.01503	0.00204	0.11475	0.66207	0.05538	0.31942	0.024	96	13	110	473
TL201-84	54443	0	0.01230	0.00198	0.08319	0.01390	0.04904	0.00223	0.962	79	13	81	13
TL201-85	133316	163	0.04392	0.00238	0.28272	0.01967	0.04668	0.00203	0.780	277	15	253	15
TL201-86	117722	201	0.05394	0.00356	0.48009	0.04362	0.06455	0.00403	0.726	339	22	398	29
TL201-87	15259	0	0.01258	0.00198	0.09124	0.03531	0.05260	0.01860	0.407	81	13	89	32
TL201-88	58122	212	0.03547	0.00286	0.32065	0.06393	0.06557	0.01196	0.404	225	18	282	48
TL201-89	41574	0	0.01678	0.00203	0.17593	0.08523	0.07606	0.03568	0.250	107	13	165	71
TL201-90	37295	0	0.02021	0.00218	0.14658	0.70424	0.05260	0.25265	0.022	129	14	139	486
TL201-91	135269	0	0.01616	0.00202	0.13829	0.03738	0.06208	0.01489	0.462	103	13	132	33
TL201-92	27178	0	0.01535	0.00202	0.12583	0.09887	0.05943	0.04604	0.167	98	13	120	85
TL201-93	44440	0	0.09303	0.00555	1.24236	0.67511	0.09686	0.05232	0.110	573	33	820	267
TL201-94	152239	218	0.07732	0.00325	1.95463	0.09297	0.18335	0.00406	0.885	480	19	1100	31
TL201-96	62364	0	0.02109	0.00204	0.14702	0.01518	0.05056	0.00179	0.939	135	13	139	13
TL201-97	129604	208	0.14967	0.00722	1.28018	0.07345	0.06203	0.00193	0.841	899	40	837	32
TL201-98	56241	0	0.01251	0.00198	0.08431	0.01367	0.04889	0.00173	0.976	80	13	82	13
TL201-99	101265	0	0.01958	0.00204	0.13883	0.02089	0.05143	0.00557	0.694	125	13	132	18
TL201-100	57258	0	0.01241	0.00198	0.08960	0.02225	0.05236	0.00997	0.642	80	13	87	21
TL201-101	35831	0	0.01252	0.00198	0.08463	0.01469	0.04904	0.00352	0.911	80	13	82	14

Appendix B: U-Pb data for sample TL202

Grain ID	^{206}Pb (cps)	^{204}Pb (cps)	^{206}Pb/^{238}U	2σ error	^{207}Pb/^{235}U	2σ error	^{207}Pb/^{206}Pb	2σ error	rho	^{206}Pb/^{238}U AGE (Ma)	2σ error (Ma)	^{207}Pb/^{235}U AGE (Ma)	2σ error (Ma)
TL202-1	324795	38	0.01234	0.00130	0.07875	0.00839	0.04628	0.00065	0.991	79	8	77	8
TL202-2	153924	16	0.01231	0.00130	0.07783	0.00832	0.04587	0.00067	0.991	79	8	76	8
TL202-3	11409	0	0.01281	0.00131	0.08356	0.14093	0.04733	0.07967	0.061	82	8	81	124
TL202-4	74509	0	0.01273	0.00131	0.08195	0.00853	0.04670	0.00080	0.987	82	8	80	8
TL202-5	32976	0	0.01257	0.00131	0.07733	0.00813	0.04463	0.00072	0.988	81	8	76	8
TL202-6	328371	0	0.12407	0.00513	1.22865	0.05570	0.07182	0.00134	0.911	754	29	814	25
TL202-7	47266	0	0.01229	0.00130	0.08697	0.00966	0.05133	0.00168	0.956	79	8	85	9
TL202-8	45564	24	0.01207	0.00131	0.09097	0.01297	0.05466	0.00508	0.759	77	8	88	12
TL202-9	72082	0	0.01200	0.00130	0.07699	0.00844	0.04652	0.00074	0.989	77	8	75	8
TL202-10	122640	0	0.01240	0.00131	0.07961	0.01207	0.04657	0.00508	0.695	79	8	78	11
TL202-11	308314	0	0.01945	0.00157	0.27403	0.03901	0.10219	0.01200	0.566	124	10	246	31
TL202-12	0	0	0.01222	0.00130	0.06809	0.00739	0.04040	0.00081	0.983	78	8	67	7
TL202-13	116261	0	0.01185	0.00130	0.07565	0.00837	0.04630	0.00066	0.992	76	8	74	8
TL202-14	142000	0	0.02141	0.00145	0.19992	0.01446	0.06771	0.00175	0.934	137	9	185	12
TL202-15	196567	10	0.03216	0.00237	0.37695	0.03913	0.08501	0.00621	0.710	204	15	325	28
TL202-16	180280	0	0.01167	0.00130	0.07478	0.00838	0.04646	0.00063	0.993	75	8	73	8
TL202-17	63117	0	0.01157	0.00130	0.07082	0.00806	0.04438	0.00085	0.986	74	8	69	8
TL202-18	566193	102	0.01151	0.00130	0.07774	0.00885	0.04897	0.00081	0.989	74	8	76	8
TL202-19	73375	0	0.01762	0.00162	0.16452	0.01907	0.06772	0.00477	0.794	113	10	155	16
TL202-20	482771	0	0.01366	0.00132	0.08996	0.00876	0.04777	0.00066	0.990	87	8	87	8
TL202-21	307895	0	0.01151	0.00130	0.07437	0.00844	0.04688	0.00063	0.993	74	8	73	8
TL202-22	122904	0	0.01193	0.00130	0.07554	0.00983	0.04590	0.00326	0.837	76	8	74	9
TL202-23	184171	0	0.01204	0.00130	0.07703	0.00839	0.04639	0.00064	0.992	77	8	75	8
TL202-24	0	0	0.01737	0.00137	0.11465	0.01147	0.04788	0.00293	0.791	111	9	110	10
TL202-25	193748	0	0.07011	0.00403	0.64023	0.10361	0.06623	0.01002	0.355	437	24	502	62
TL202-26	238966	0	0.08785	0.00809	1.19702	0.44019	0.09883	0.03518	0.250	543	48	799	185

Appendix B: U-Pb data for sample TL202 cont'd.

Grain ID	^{206}Pb (cps)	^{204}Pb (cps)	^{206}Pb/^{238}U	2σ error	^{207}Pb/^{235}U	2σ error	^{207}Pb/^{206}Pb	2σ error	rho	^{206}Pb/^{238}U AGE (Ma)	2σ error (Ma)	^{207}Pb/^{235}U AGE (Ma)	2σ error (Ma)
TL202-27	83056	0	0.01204	0.00130	0.07496	0.00819	0.04515	0.00070	0.990	77	8	73	8
TL202-28	95644	0	0.01243	0.00131	0.07819	0.00833	0.04564	0.00083	0.985	80	8	76	8
TL202-29	489769	26	0.28615	0.01625	7.40886	0.61697	0.18779	0.01144	0.682	1622	81	2162	72
TL202-30	100648	0	0.01226	0.00130	0.07631	0.00824	0.04514	0.00082	0.986	79	8	75	8
TL202-31	280231	0	0.01789	0.00151	0.16308	0.01933	0.06609	0.00549	0.714	114	10	153	17
TL202-32	68647	0	0.01213	0.00130	0.07776	0.01027	0.04650	0.00357	0.814	78	8	76	10
TL202-33	327959	11	0.03549	0.00198	0.38936	0.02542	0.07956	0.00269	0.855	225	12	334	18
TL202-34	146153	0	0.01194	0.00130	0.07861	0.00990	0.04775	0.00302	0.865	77	8	77	9
TL202-35	137311	0	0.01206	0.00130	0.07617	0.01316	0.04580	0.00618	0.625	77	8	75	12
TL202-36	0	0	0.01202	0.00130	0.07487	0.02189	0.04519	0.01227	0.371	77	8	73	20
TL202-37	42473	0	0.01228	0.00130	0.06944	0.01199	0.04102	0.00558	0.615	79	8	68	11
TL202-38	142499	10	0.01416	0.00138	0.12327	0.01404	0.06315	0.00370	0.857	91	9	118	13
TL202-39	155280	0	0.01232	0.00130	0.07958	0.02716	0.04683	0.01519	0.310	79	8	78	25
TL202-40	417679	36	0.06165	0.00283	0.76205	0.04202	0.08965	0.00273	0.833	386	17	575	24
TL202-41	129689	0	0.01271	0.00131	0.08078	0.04642	0.04611	0.02607	0.179	81	8	79	43
TL202-42	102206	0	0.01221	0.00130	0.07990	0.02728	0.04746	0.01540	0.313	78	8	78	25
TL202-43	216785	0	0.01229	0.00130	0.07910	0.00858	0.04670	0.00104	0.979	79	8	77	8
TL202-44	153513	0	0.01204	0.00130	0.07594	0.01298	0.04576	0.00606	0.633	77	8	74	12
TL202-45	55686	0	0.01342	0.00131	0.07349	0.16933	0.03971	0.09140	0.043	86	8	72	149
TL202-46	880092	74	0.08894	0.00510	1.19858	0.07740	0.09774	0.00291	0.888	549	30	800	35
TL202-47	34868	0	0.01218	0.00130	0.08437	0.19838	0.05023	0.11798	0.045	78	8	82	171
TL202-48	0	0	0.01282	0.00131	0.09257	0.12720	0.05237	0.07175	0.074	82	8	90	112
TL202-49	195192	98	0.03948	0.00257	0.44811	0.03658	0.08233	0.00404	0.799	250	16	376	25
TL202-50	151973	0	0.01500	0.00133	0.10666	0.04601	0.05157	0.02177	0.206	96	8	103	41
TL202-51	1086144	170	0.18897	0.00780	3.76594	0.18556	0.14454	0.00389	0.838	1116	42	1586	39
TL202-52	87904	0	0.01448	0.00133	0.09654	0.01044	0.04835	0.00276	0.850	93	8	94	10

Appendix B: U-Pb data for sample TL202 cont'd.

Grain ID	^{206}Pb (cps)	^{204}Pb (cps)	^{206}Pb/^{238}U	2σ error	^{207}Pb/^{235}U	2σ error	^{207}Pb/^{206}Pb	2σ error	rho	^{206}Pb/^{238}U AGE (Ma)	2σ error (Ma)	^{207}Pb/^{235}U AGE (Ma)	2σ error (Ma)
TL202-53	50897	0	0.01383	0.00132	0.09360	0.02691	0.04909	0.01332	0.332	89	8	91	25
TL202-54	74334	0	0.01352	0.00132	0.08999	0.00887	0.04826	0.00071	0.989	87	8	87	8
TL202-55	80294	0	0.01285	0.00131	0.09301	0.01082	0.05250	0.00294	0.876	82	8	90	10
TL202-56	420772	0	0.01947	0.00138	0.13097	0.00948	0.04879	0.00065	0.983	124	9	125	8
TL202-57	313403	0	0.01907	0.00138	0.12905	0.01007	0.04907	0.00141	0.930	122	9	123	9
TL202-58	36594	0	0.18313	0.00568	1.92640	1.06961	0.07629	0.04229	0.056	1084	31	1090	316
TL202-59	86529	0	0.01426	0.00132	0.09379	0.01324	0.04770	0.00508	0.656	91	8	91	12
TL202-60	0	0	0.01215	0.00130	0.07967	0.00953	0.04754	0.00253	0.895	78	8	78	9
TL202-61	181370	0	0.01214	0.00130	0.07999	0.02091	0.04777	0.01139	0.410	78	8	78	19
TL202-62	303627	105	0.03246	0.00209	0.38195	0.04042	0.08534	0.00718	0.607	206	13	328	29
TL202-63	141307	0	0.01482	0.00134	0.11375	0.02320	0.05566	0.01017	0.444	95	9	109	21
TL202-64	277036	134	0.03528	0.00194	0.32323	0.02334	0.06644	0.00312	0.760	224	12	284	18
TL202-65	45479	0	0.01293	0.00131	0.08338	0.01735	0.04675	0.00850	0.487	83	8	81	16
TL202-66	40182	0	0.01286	0.00131	0.08220	0.00957	0.04635	0.00262	0.874	82	8	80	9
TL202-67	120539	0	0.01246	0.00131	0.08165	0.00882	0.04752	0.00125	0.970	80	8	80	8
TL202-68	159551	0	0.01226	0.00130	0.08011	0.00987	0.04739	0.00295	0.863	79	8	78	9
TL202-69	194908	0	0.01218	0.00130	0.07999	0.00883	0.04765	0.00129	0.969	78	8	78	8
TL202-70	87893	0	0.01230	0.00130	0.08079	0.01401	0.04764	0.00654	0.611	79	8	79	13
TL202-71	165591	0	0.01237	0.00130	0.08146	0.00876	0.04776	0.00099	0.981	79	8	80	8
TL202-72	0	0	0.01269	0.00131	0.08334	0.02148	0.04764	0.01125	0.400	81	8	81	20
TL202-73	187929	109	0.01809	0.00142	0.15751	0.01840	0.06314	0.00546	0.673	116	9	149	16
TL202-74	475060	204	0.08005	0.00293	1.69972	0.07214	0.15399	0.00331	0.862	496	17	1008	27
TL202-75	102144	0	0.01200	0.00130	0.07887	0.01207	0.04765	0.00515	0.708	77	8	77	11
TL202-76	189953	0	0.01351	0.00132	0.09252	0.02583	0.04968	0.01299	0.351	86	8	90	24
TL202-77	144036	0	0.02243	0.00154	0.19342	0.03294	0.06254	0.00974	0.404	143	10	180	28
TL202-78	263279	186	0.02515	0.00161	0.22805	0.01825	0.06577	0.00317	0.798	160	10	209	15

Appendix B: U-Pb data for sample TL202 cont'd.

Grain ID	^{206}Pb (cps)	^{204}Pb (cps)	$^{206}Pb/^{238}U$	2σ error	$^{207}Pb/^{235}U$	2σ error	$^{207}Pb/^{206}Pb$	2σ error	rho	$^{206}Pb/^{238}U$ AGE (Ma)	2σ error (Ma)	$^{207}Pb/^{235}U$ AGE (Ma)	2σ error (Ma)
TL202-79	406038	173	0.04987	0.00228	0.39071	0.02112	0.05683	0.00163	0.847	314	14	335	15
TL202-80	327406	0	0.01954	0.00139	0.13594	0.08976	0.05045	0.03312	0.107	125	9	129	77
TL202-81	357981	0	0.01186	0.00130	0.07832	0.00880	0.04789	0.00120	0.975	76	8	77	8
TL202-82	178844	0	0.01205	0.00130	0.08001	0.00905	0.04814	0.00162	0.954	77	8	78	8
TL202-83	100440	0	0.01372	0.00132	0.09117	0.00962	0.04821	0.00206	0.915	88	8	89	9
TL202-84	0	0	0.02079	0.00165	0.19922	0.02129	0.06950	0.00498	0.742	133	10	184	18
TL202-85	136807	0	0.01592	0.00138	0.10900	0.24918	0.04964	0.11341	0.038	102	9	105	206
TL202-86	288934	0	0.01259	0.00131	0.08300	0.00943	0.04782	0.00221	0.914	81	8	81	9
TL202-87	158766	0	0.01265	0.00131	0.08479	0.05219	0.04862	0.02950	0.168	81	8	83	48
TL202-88	283936	0	0.01278	0.00131	0.08526	0.01940	0.04837	0.00983	0.450	82	8	83	18
TL202-89	144001	172	0.21059	0.00705	1.95093	0.07788	0.06719	0.00146	0.839	1232	37	1099	26
TL202-90	215764	181	0.07707	0.00497	0.63816	0.04671	0.06006	0.00208	0.881	479	30	501	29
TL202-91	131625	0	0.01250	0.00131	0.08345	0.03875	0.04841	0.02190	0.225	80	8	81	36
TL202-92	131249	0	0.01274	0.00131	0.08392	0.00880	0.04776	0.00103	0.979	82	8	82	8
TL202-93	86606	0	0.01227	0.00130	0.08125	0.04736	0.04801	0.02751	0.182	79	8	79	44
TL202-94	173745	0	0.01270	0.00131	0.09507	0.05364	0.05431	0.03013	0.182	81	8	92	49
TL202-95	53487	0	0.02238	0.00144	0.16628	0.03647	0.05388	0.01130	0.293	143	9	156	31
TL202-96	0	0	0.01265	0.00131	0.08498	0.00927	0.04871	0.00171	0.947	81	8	83	9
TL202-97	153337	0	0.01228	0.00130	0.08080	0.01539	0.04773	0.00755	0.558	79	8	79	14
TL202-98	162365	199	0.03695	0.00220	0.24738	0.02315	0.04855	0.00350	0.638	234	14	224	19
TL202-99	297692	0	0.01282	0.00131	0.08641	0.16356	0.04888	0.09238	0.054	82	8	84	142
TL202-100	192327	0	0.01189	0.00130	0.07923	0.00960	0.04834	0.00252	0.903	76	8	77	9
TL202-101	131900	0	0.01762	0.00144	0.14036	0.09356	0.05778	0.03822	0.122	113	9	133	80
TL202-102	105922	0	0.01263	0.00131	0.09315	0.11133	0.05348	0.06368	0.087	81	8	90	98
TL202-103	250240	0	0.01226	0.00130	0.08193	0.00888	0.04847	0.00102	0.981	79	8	80	8
TL202-104	53196	0	0.01268	0.00131	0.08707	0.03043	0.04980	0.01663	0.295	81	8	85	28

Appendix C: Fluid Inclusion Data

Ref #	Sample	Fill[1] %	Visible Contents[2] at 20°C	Tm_{CO_2} °C	Tm_{ice} °C	Salinity[3] wt.% NaCl eq. (Bodnar, 1993)	Tm_{Clath} °C	Salinity[3] wt.% NaCl eq. (Bozzo et al., 1975)	$Th_{CO_2\ L\text{-}V(L)}$ °C	$Th_{L\text{-}V(L)}$ °C	Class
MAX F252	07-03 1349	95	L + V	-	-4.3	8.5	-	-	-	169	Secondary?
MAX F253	07-03 1349	70	L + V	-	-4.2	8.3	-	-	-	224	Primary
MAX F254	07-03 1349	90	L + V	-	-	-	8.2	3.6	-	228	Primary
MAX F255	07-03 1349	50	CO_2 + L + V	-55.7	-	-	8.4	3.2	17.9	234	Primary
MAX F256	07-03 1349	95	L + V	-	-2.7	5.1	-	-	-	237	Secondary?
MAX F257	07-03 1349	70	L + V	-	-4.9	9.8	-	-	-	241	Primary
MAX F258	07-03 1349	70	L + V	-	-4.0	7.9	-	-	-	224	Primary
MAX F259	07-03 1349	90	L + V	-	-3.6	7.0	-	-	-	246	Primary
MAX F260	07-03 1349	95	L + V	-	-5.0	10.1	-	-	-	242	Primary
MAX F261	07-03 1349	50	CO_2 + L + V	-56.7	-	-	7.5	4.9	13.7	251	Primary
MAX F262	07-03 1349	95	L + V	-	-5.1	10.3	-	-	-	224	Primary
MAX F263	07-03 1349	70	CO_2 + L + V	-57.0	-	-	8.4	3.2	14.2	262	Primary
MAX F264	07-03 1349	80	L + V	-	-4.0	7.9	-	-	-	246	Primary
MAX F265	07-03 1349	70	CO_2 + L + V	-57.5	-	-	9.2	1.6	19.7	249	Primary
MAX F266	07-03 1349	50	CO_2 + L + V	-58.1	-	-	8.9	2.2	20.1	252	Primary
MAX F283	07-03-657	95	L + V	-	-1.7	3.2	-	-	-	243	Primary
MAX F284	07-03-657	95	L + V	-	-1.3	2.4	-	-	-	252	Pseudosecondary
MAX F285	07-03-657	95	L + V	-	-4.7	9.4	-	-	-	214	Pseudosecondary
MAX F286	07-03-657	95	L + V	-	-1.1	2.0	-	-	-	228	Primary
MAX F287	07-03-657	50	CO_2 + L + V	-62.4	-	-	8.0	4.0	27.1	246	Primary
MAX F288	07-03-657	70	CO_2 + L + V	-61.3	-	-	9.1	1.8	16.8	223	Primary

Appendix C: Fluid Inclusion Data cont'd

Ref #	Sample	Fill[1] %	Visible Contents[2] at 20°C	Tm_{CO_2} °C	Tm_{ice} °C	Salinity[3] wt.% NaCl eq. (Bodnar, 1993)	Tm_{Clath} °C	Salinity[3] wt.% NaCl eq. (Bozzo et al., 1975)	$Th_{CO_2\ L\text{-}V(L)}$ °C	$Th_{L\text{-}V(L)}$ °C	Class
MAX F289	07-03-657	70	CO_2 + L + V	-59.8	-	-	6.9	5.9	26.8	226	Pseudosecondary
MAX F290	07-03-657	70	CO_2 + L + V	-61.2	-	-	7.6	4.7	17.0	235	Pseudosecondary
MAX F291	07-03-657	80	CO_2 + L + V	-57.1	-	-	9.2	1.6	-	240	Pseudosecondary
MAX F292	07-03-657	70	CO_2 + L + V	-56.9	-	-	8.7	2.6	23.5	252	Pseudosecondary
MAX F293	07-03-657	60	CO_2 + L + V	-58.7	-	-	9.3	1.4	20.2	247	Primary
MAX F294	07-03-657	70	CO_2 + L + V	-57.3	-	-	8.9	2.2	18.2	220	Primary
MAX F267	07-03-668	70	CO_2 + L + V	-56.7	-	-	8.4	3.2	-	250	Primary
MAX F268	07-03-668	70	CO_2 + L + V	-56.9	-	-	8.6	2.8	24.5	252	Primary
MAX F269	07-03-668	70	CO_2 + L + V	-56.7	-	-	8.1	3.8	23.2	250	Primary
MAX F270	07-03-668	70	CO_2 + L + V	-56.7	-	-	7.9	4.1	26.2	291	Primary
MAX F271	07-03-668	70	CO_2 + L + V	-64.3	-	-	8.6	2.8	21.7	218	Primary
MAX F272	07-03-668	70	CO_2 + L + V	-56.7	-	-	8.0	4.0	12.0	223	Pseudosecondary
MAX F273	07-03-668	70	CO_2 + L + V	-56.9	-	-	8.6	2.8	13.0	232	Pseudosecondary
MAX F274	07-03-668	70	CO_2 + L + V	-58.4	-	-	6.7	6.3	16.5	246	Primary
MAX F275	07-03-668	70	CO_2 + L + V	-56.3	-	-	7.9	4.1	25.1	222	Primary
MAX F276	07-03-668	80	CO_2 + L + V	-	-	-	8.4	3.2	25.7	298	Primary
MAX F277	07-03-668	70	CO_2 + L + V	-57.5	-	-	7.7	4.5	18.7	260	Primary
MAX F278	07-03-668	70	CO_2 + L + V	-56.0	-	-	7.9	4.1	25.2	238	Primary
MAX F279	07-03-668	70	CO_2 + L + V	-57.2	-	-	8.6	2.8	16.3	213	Primary
MAX F280	07-03-668	50	CO_2 + L + V	-56.9	-	-	8.9	2.2	18.9	244	Primary
MAX F281	07-03-668	70	CO_2 + L + V	-56.8	-	-	8.2	3.6	24.5	220	Primary

Appendix C: Fluid Inclusion Data cont'd

Ref #	Sample	Fill[1] %	Visible Contents[2] at 20°C	Tm_{CO_2} °C	Tm_{ice} °C	Salinity[3] wt.% NaCl eq. (Bodnar, 1993)	Tm_{Clath} °C	Salinity[3] wt.% NaCl eq. (Bozzo et al., 1975)	$Th_{CO_2\ L\text{-}V(L)}$ °C	$Th_{L\text{-}V(L)}$ °C	Class
MAX F282	07-03-668	70	CO_2 + L + V	-56.3	-	-	8.4	3.2	28.0	251	Primary
MAX F295	07-03-723	70	CO_2 + L + V	-56.9	-	-	8.1	3.8	25.8	240	Pseudosecondary
MAX F296	07-03-723	70	CO_2 + L + V	-56.3	-	-	-	-	24.8	319	Primary
MAX F297	07-03-723	80	CO_2 + L + V	-56.8	-	-	6.1	7.3	9.2	268	Primary
MAX F298	07-03-723	80	CO_2 + L + V	-56.4	-	-	7.7	4.5	10.1	307	Primary
MAX F299	07-03-723	95	CO_2 + L + V	-56.9	-	-	8.1	3.8	17.3	253	Primary
MAX F300	07-03-723	95	CO_2 + L + V	-56.6	-	-	8.4	3.2	28.6	278	Primary
MAX F301	07-03-723	70	CO_2 + L + V	-56.4	-	-	7.5	4.9	20.4	265	Primary
MAX F302	07-03-723	70	CO_2 + L + V	-56.4	-	-	6.2	7.1	26.2	252	Primary
MAX F303	07-03-723	70	CO_2 + L + V	-56.6	-	-	8.3	3.4	20.1	241	Primary
MAX F304	07-03-723	90	L + V	-	-2.7	5.1	-	-	-	236	Primary
MAX F305	07-03-723	70	CO_2 + L + V	-56.7	-	-	8.7	2.6	19.8	222	Primary
MAX F306	07-03-723	70	CO_2 + L + V	-56.5	-	-	8.2	3.6	17.3	247	Primary
MAX F100	07-04-730	70	CO_2 + L + V	-56.3	-	-	7.7	4.5	20.4	213	Primary
MAX F101	07-04-730	90	L + V	-	-	-	7.1	5.6	-	204	Primary
MAX F102	07-04-730	90	L + V	-	-	-	9.1	1.8	-	241	Primary
MAX F103	07-04-730	90	L + V	-	-	-	8.7	2.6	-	254	Primary
MAX F104	07-04-730	90	L + V	-	-1.9	3.5	-	-	-	236	Pseudosecondary
MAX F105	07-04-730	90	L + V	-	-2.4	4.5	-	-	-	183	Pseudosecondary
MAX F106	07-04-730	90	L + V	-	-3.4	6.6	-	-	-	207	Primary
MAX F107	07-04-730	90	L + V	-	-2.9	5.5	-	-	-	210	Primary

Appendix C: Fluid Inclusion Data cont'd

Ref #	Sample	Fill[1] %	Visible Contents[2] at 20°C	Tm_{CO_2} °C	Tm_{ice} °C	Salinity[3] wt.% NaCl eq. (Bodnar, 1993)	Tm_{Clath} °C	Salinity[3] wt.% NaCl eq. (Bozzo et al., 1975)	$Th_{CO_2\ L\text{-}V(L)}$ °C	$Th_{L\text{-}V(L)}$ °C	Class
MAX F108	07-04-730	90	L + V	-	-3.3	6.4	-	-	-	202	Primary
MAX F109	07-04-730	90	L + V	-	-2.3	4.3	-	-	-	217	Primary
MAX F110	07-04-730	90	L + V	-	-4.5	9.0	-	-	-	176	Primary
MAX F111	07-04-730	90	L + V	-	-2.9	5.5	-	-	-	221	Primary
MAX F112	07-04-730	70	CO_2 + L + V	-56.5	-	-	7.6	4.7	26.7	297	Pseudosecondary
MAX F113	07-04-730	90	L + V	-	-4.5	9.0	-	-	-	223	Primary
MAX F114	07-04-730	70	CO_2 + L + V	-56.7	-	-	8.3	3.4	25.0	242	Primary
MAX F115	07-04-730	70	CO_2 + L + V	-57.9	-	-	8.1	3.8	26.7	244	Primary
MAX F116	07-04-730	90	L + V	-	-1.6	3.0	-	-	-	226	Pseudosecondary
MAX F117	07-04-730	90	L + V	-	-	-	8.2	3.6	-	259	Pseudosecondary
MAX F118	07-04-730	90	L + V	-	-2.1	3.9	-	-	-	302	Pseudosecondary
MAX F119	07-04-730	90	L + V	-	-1.3	2.4	-	-	-	248	Pseudosecondary
MAX F120	07-04-730	90	L + V	-	-2.0	3.7	-	-	-	200	Primary
MAX F121	07-04-730	90	L + V	-	-1.5	2.8	-	-	-	234	Primary
MAX F122	07-04-730	90	L + V	-	-2.9	5.5	-	-	-	192	Primary
MAX F123	07-04-730	90	L + V	-	-2.2	-	-	-	-	211	Primary
MAX F124	07-04-730	90	L + V	-	-	-	8.1	3.8	-	224	Primary
MAX F125	07-04-730	90	L + V	-	-	-	8.4	3.2	-	223	Primary
MAX F126	07-04-730	70	CO_2 + L + V	-56.6	-	-	7.8	4.3	22.0	302	Primary
MAX F127	07-04-730	90	L + V	-	-	-	7.6	4.7	-	330	Primary
MAX F128	07-04-730	90	CO_2 + L + V	-55.6	-	-	8.9	2.2	24.6	264	Primary

Appendix C: Fluid Inclusion Data cont'd

Ref #	Sample	Fill[1] %	Visible Contents[2] at 20°C	Tm_{CO_2} °C	Tm_{ice} °C	Salinity[3] wt.% NaCl eq. (Bodnar, 1993)	Tm_{Clath} °C	Salinity[3] wt.% NaCl eq. (Bozzo et al., 1975)	$Th_{CO_2\ L\text{-}V(L)}$ °C	$Th_{L\text{-}V(L)}$ °C	Class
MAX F129	07-04-730	90	L + V	-	-	-	8.9	2.2	-	307	Primary
MAX F130	07-04-730	90	L + V	-	-	-	9.5	1.0	-	314	Primary
MAX F131	07-04-730	90	L + V	-	-	-	8.5	3.0	-	226	Primary
MAX F132	07-04-730	90	CO_2 + L + V	-56.5	-	-	8.5	3.0	22.8	264	Primary
MAX F85	07-04-730	90	L + V	-	-4.6	9.2	-	-	-	226	Primary
MAX F86	07-04-730	70	CO_2 + L + V	-58.3	-	-	9.2	1.6	20.2	281	Primary
MAX F87	07-04-730	90	L + V	-	-3.6	7.0	-	-	-	193	Primary
MAX F88	07-04-730	90	L + V	-	-3.8	7.4	-	-	-	196	Primary
MAX F89	07-04-730	70	L + V	-	-3.9	7.6	-	-	-	231	Primary
MAX F90	07-04-730	90	L + V	-	-	-	9.3	1.4	-	233	Primary
MAX F91	07-04-730	90	L + V	-	-0.7	1.3	-	-	-	234	Pseudosecondary
MAX F92	07-04-730	90	L + V	-	-2.9	5.5	-	-	-	236	Pseudosecondary
MAX F93	07-04-730	90	L + V	-	-	-	10.3	-	-	245	Primary
MAX F94	07-04-730	90	L + V	-	-	-	8.4	3.2	-	178	Primary
MAX F95	07-04-730	70	CO_2 + L + V	-56.7	-	-	6.9	5.9	29.0	259	Primary
MAX F96	07-04-730	70	CO_2 + L + V	-56.5	-	-	7.6	4.7	20.1	227	Primary
MAX F97	07-04-730	70	CO_2 + L + V	-56.8	-	-	8.0	4.0	24.0	244	Pseudosecondary
MAX F98	07-04-730	70	CO_2 + L + V	-56.3	-	-	6.3	7.0	16.3	290	Primary
MAX F99	07-04-730	70	CO_2 + L + V	-56.6	-	-	5.9	7.6	28.8	238	Primary
MAX F40	07-05 709A	80	CO_2 + L + V	-55.0	-	-	14.4	-	27.8	232	Primary
MAX F41	07-05 709A	90	L + V	-	-	-	9.1	1.8	-	285	Primary

Appendix C: Fluid Inclusion Data cont'd

Ref #	Sample	Fill[1] %	Visible Contents[2] at 20°C	Tm_{CO_2} °C	Tm_{ice} °C	Salinity[3] wt.% NaCl eq. (Bodnar, 1993)	Tm_{Clath} °C	Salinity[3] wt.% NaCl eq. (Bozzo et al., 1975)	$Th_{CO_2\ L\text{-}V(L)}$ °C	$Th_{L\text{-}V(L)}$ °C	Class
MAX F42	07-05 709A	80	CO_2 + L + V	-56.4	-	-	8.8	2.4	28.0	275	Primary
MAX F43	07-05 709A	90	CO_2 + L + V	-55.7	-	-	8.8	2.4	26.5	235	Primary
MAX F44	07-05 709A	90	CO_2 + L + V	-56.0	-	-	7.7	4.5	22.3	217	Primary
MAX F45	07-05 709A	90	L + V	-	-	-	8.4	3.2	-	275	Primary
MAX F46	07-05 709A	90	L + V	-	-3.8	7.4	-	-	-	250	Primary
MAX F47	07-05 709A	90	L + V	-	-	-	8.6	2.8	-	301	Primary
MAX F48	07-05 709A	80	L + V	-	-2.7	5.1	-	-	-	232	Primary
MAX F49	07-05 709A	80	L + V	-	-	-	8.2	3.6	-	247	Primary
MAX F50	07-05 709A	90	L + V	-	-	-	7.9	4.1	-	249	Primary
MAX F51	07-05 709A	90	CO_2 + L + V	-55.0	-	-	7.0	5.8	17.9	237	Primary
MAX F52	07-05 709A	90	CO_2 + L + V	-54.0	-	-	7.8	4.3	16.5	227	Primary
MAX F53	07-05 709A	90	L + V	-	-	-	5.9	7.6	-	207	Primary
MAX F54	07-05 709A	85	L + V	-	-	-	7.9	4.1	-	209	Primary
MAX F55	07-05 709A	80	CO_2 + L + V	-56.3	-	-	8.5	3.0	25.6	216	Primary
MAX F56	07-05 709A	70	L + V	-	-4.2	8.3	-	-	-	251	Primary
MAX F57	07-05 709A	90	L + V	-	-	-	8.3	3.4	-	217	Pseudosecondary
MAX F58	07-05 709A	70	L + V	-	-	-	8.9	2.2	-	265	Pseudosecondary
MAX F59	07-05 709A	90	L + V	-	-	-	8.6	2.8	-	270	Pseudosecondary
MAX F60	07-05 709A	90	L + V	-	-	-	7.3	5.2	-	277	Pseudosecondary
MAX F61	07-05 709A	80	L + V	-	-	-	7.6	4.7	-	247	Primary
MAX F62	07-05-709	80	L + V	-	-	-	8.7	2.6	-	221	Primary

Appendix C: Fluid Inclusion Data cont'd

Ref #	Sample	Fill[1] %	Visible Contents[2] at 20°C	Tm_{CO_2} °C	Tm_{ice} °C	Salinity[3] wt.% NaCl eq. (Bodnar, 1993)	Tm_{Clath} °C	Salinity[3] wt.% NaCl eq. (Bozzo et al., 1975)	$Th_{CO_2\ L\text{-}V(L)}$ °C	$Th_{L\text{-}V(L)}$ °C	Class
MAX F63	07-05-709	80	CO_2 + L + V	-54.0	-	-	8.9	2.2	22.1	248	Primary
MAX F64	07-05-709	90	L + V	-	-4.5	9.0	-	-	-	243	Primary
MAX F65	07-05-709	80	CO_2 + L + V	-56.3	-	-	7.8	4.3	27.0	302	Primary
MAX F66	07-05-709	90	CO_2 + L + V	-56.7	-	-	8.6	2.8	18.9	273	Primary
MAX F67	07-05-709	80	CO_2 + L + V	-56.3	-	-	8.7	2.6	16.4	228	Primary
MAX F68	07-05-709	90	L + V	-	-4.8	9.6	-	-	-	230	Primary
MAX F69	07-05-709	70	L + V	-	-	-	9.1	1.8	-	263	Primary
MAX F70	07-05-709	90	L + V	-	-	-	8.6	2.8	-	204	Primary
MAX F71	07-05-709	90	L + V	-	-	-	8.0	4.0	-	249	Primary
MAX F72	07-05-709	90	L + V	-	-	-	6.4	6.8	-	229	Primary
MAX F73	07-05-709	90	L + V	-	-	-	9.3	1.4	-	247	Primary
MAX F74	07-05-709	80	L + V	-	-2.5	4.7	-	-	-	253	Primary
MAX F75	07-05-709	90	L + V	-	-	-	7.5	4.9	-	220	Primary
MAX F76	07-05-709	90	L + V	-	-2.7	5.1	-	-	-	226	Primary
MAX F77	07-05-709	90	L + V	-	-3.6	7.0	-	-	-	225	Primary
MAX F78	07-05-709	90	L + V	-	-5.7	11.7	-	-	-	207	Primary
MAX F79	07-05-709	90	L + V	-	-	-	11.1	-	-	240	Primary
MAX F80	07-05-709	90	L + V	-	-	-	11.3	-	-	246	Primary
MAX F81	07-05-709	90	L + V	-	-	-	11.6	-	-	256	Primary
MAX F82	07-05-709	90	L + V	-	-	-	10.8	-	-	230	Primary
MAX F83	07-05-709	70	CO_2 + L + V	-56.3	-	-	7.5	4.9	18.7	262	Primary

Appendix C: Fluid Inclusion Data cont’d

Ref #	Sample	Fill[1] %	Visible Contents[2] at 20°C	Tm_{CO_2} °C	Tm_{ice} °C	Salinity[3] wt.% NaCl eq. (Bodnar, 1993)	Tm_{Clath} °C	Salinity[3] wt.% NaCl eq. (Bozzo et al., 1975)	$Th_{CO_2\ L\text{-}V(L)}$ °C	$Th_{L\text{-}V(L)}$ °C	Class
MAX F84	07-05-709	70	CO_2 + L + V	-56.4	-	-	7.6	4.7	22.3	236	Primary
MAX F221	TL11	70	CO_2 + L + V	-56.6	-	-	8.7	2.6	18.3	331	Primary
MAX F222	TL11	70	CO_2 + L + V	-	-	-	7.9	4.1	23.2	306	Primary
MAX F223	TL11	50	CO_2 + L + V	-56.9	-	-	6.9	5.9	24.5	292	Primary
MAX F224	TL11	95	L + V	-	-1.3	2.4	-	-	-	248	Pseudosecondary
MAX F225	TL11	80	L + V	-	-	-	10.7	-	-	243	Primary
MAX F226	TL11	80	CO_2 + L + V	-57.4	-	-	10.6	-	-	333	Primary
MAX F227	TL11	80	CO_2 + L + V	-54.7	-	-	8.6	2.8	23.1	314	Primary
MAX F228	TL11	90	CO_2 + L + V	-57.0	-	-	8.9	2.2	22.4	287	Primary
MAX F229	TL11	70	CO_2 + L + V	-56.1	-	-	5.9	7.6	18.2	238	Primary
MAX F230	TL11	70	CO_2 + L + V	-56.7	-	-	8.3	3.4	17.5	216	Primary
MAX F231	TL11	70	CO_2 + L + V	-55.8	-	-	8.0	4.0	16.3	230	Primary
MAX F232	TL11	70	CO_2 + L + V	-56.4	-	-	8.7	2.6	28.1	251	Primary
MAX F233	TL11	50	CO_2 + L + V	-56.2	-	-	8.2	3.6	23.4	323	Primary
MAX F234	TL11	95	L + V	-	-4.6	9.2	-	-	-	266	Primary
MAX F235	TL11	70	CO_2 + L + V	-	-	-	8.4	3.2	20.0	281	Primary
MAX F236	TL11	70	L + V	-	-3.0	5.8	-	-	-	270	Primary
MAX F237	TL11	90	L + V	-	-	-	-	-	-	300	Primary
MAX F238	TL11	70	CO_2 + L + V	-57.9	-	-	8.0	4.0	-	327	Primary
MAX F239	TL11	70	CO_2 + L + V	-59.8	-	-	8.3	3.4	19.5	287	Primary
MAX F240	TL11	70	CO_2 + L + V	-62.4	-	-	7.8	4.3	22.9	323	Primary

Appendix C: Fluid Inclusion Data cont'd

Ref #	Sample	Fill[1] %	Visible Contents[2] at 20°C	Tm_{CO_2} °C	Tm_{ice} °C	Salinity[3] wt.% NaCl eq. (Bodnar, 1993)	Tm_{Clath} °C	Salinity[3] wt.% NaCl eq. (Bozzo et al., 1975)	$Th_{CO_2\ L\text{-}V(L)}$ °C	$Th_{L\text{-}V(L)}$ °C	Class
MAX F241	TL11	50	CO_2 + L + V	-57.2	-	-	9.1	1.8	23.4	325	Primary
MAX F242	TL11	80	L + V	-	-5.1	10.3	-	-	-	275	Primary
MAX F199	TL11 A	70	CO_2 + L + V	-57.8	-	-	7.9	4.1	16.1	282	Primary
MAX F200	TL11 A	95	L + V	-	-	-	8.6	2.8	-	268	Primary
MAX F201	TL11 A	70	CO_2 + L + V	-62.4	-	-	7.5	4.9	16.7	307	Primary
MAX F202	TL11 A	70	CO_2 + L + V	-56.9	-	-	7.7	4.5	22.3	291	Primary
MAX F203	TL11 A	70	CO_2 + L + V	-56.2	-	-	7.3	5.2	18.4	319	Primary
MAX F204	TL11 A	80	CO_2 + L + V	-55.6	-	-	8.1	3.8	20.5	242	Primary
MAX F205	TL11 A	90	L + V	-	-2.9	5.5	-	-	-	243	Primary
MAX F206	TL11 A	90	L + V	-	-	-	6.5	6.6	-	261	Primary
MAX F207	TL11 A	90	L + V	-	-2.7	5.1	-	-	-	249	Primary
MAX F208	TL11 A	70	CO_2 + L + V	-56.3	-	-	9.7	0.6	19.9	318	Primary
MAX F209	TL11 A	70	CO_2 + L + V	-	-	-	8.6	2.8	20.1	294	Primary
MAX F210	TL11 A	70	CO_2 + L + V	-58.1	-	-	8.0	4.0	18.6	322	Primary
MAX F211	TL11 A	70	CO_2 + L + V	-57.3	-	-	9.2	1.6	21.3	313	Primary
MAX F212	TL11 A	95	L + V	-	-4.9	9.8	-	-	-	206	Primary
MAX F213	TL11 A	95	L + V	-	-4.8	9.6	-	-	-	218	Primary
MAX F214	TL11 A	70	L + V	-	-5.1	10.3	-	-	-	217	Primary
MAX F215	TL11 A	70	CO_2 + L + V	-57.5	-	-	8.6	2.8	15.7	305	Primary
MAX F216	TL11 A	80	CO_2 + L + V	-57.1	-	-	8.2	3.6	19.5	316	Primary
MAX F217	TL11 A	70	CO_2 + L + V	-57.4	-	-	8.9	2.2	20.2	311	Primary

Appendix C: Fluid Inclusion Data cont'd

Ref #	Sample	Fill[1] %	Visible Contents[2] at 20°C	Tm_{CO_2} °C	Tm_{ice} °C	Salinity[3] wt.% NaCl eq. (Bodnar, 1993)	Tm_{Clath} °C	Salinity[3] wt.% NaCl eq. (Bozzo et al., 1975)	$Th_{CO_2\ L\text{-}V(L)}$ °C	$Th_{L\text{-}V(L)}$ °C	Class
MAX F218	TL11 A	70	CO_2 + L + V	-57.7	-	-	9.3	1.4	19.7	320	Primary
MAX F219	TL11 A	70	CO_2 + L + V	-58.5	-	-	7.1	5.6	20.9	343	Primary
MAX F220	TL11 A	70	CO_2 + L + V	-58.8	-	-	10.9	-	20.2	342	Primary
MAX F30	TL4	90	CO_2 + L + V	-55.6	-	-	6.9	5.9	20.3	270	Primary
MAX F31	TL4	95	L + V	-	-	-	-	-	-	295	Primary
MAX F32	TL4	80	L + V	-	-	-	8.4	3.2	-	298	Primary
MAX F33	TL4	90	L + V	-	-	-	7.8	4.3	-	329	Primary
MAX F34	TL4	90	CO_2 + L + V	-55.4	-	-	8.6	2.8	18.9	302	Primary
MAX F35	TL4	70	L + V	-	-4.8	9.6	-	-	-	296	Primary
MAX F36	TL4	90	L + V	-	-2.0	3.7	-	-	-	315	Primary
MAX F37	TL4	90	CO_2 + L + V	-56.0	-	-	10.0	-	17.7	287	Primary
MAX F38	TL4	90	L + V	-	-2.7	5.1	-	-	-	274	Primary
MAX F39	TL4	85	L + V	-	-2.4	4.5	-	-	-	343	Primary
MAX F4	TL4	95	L + V	-	-	-	9.8	0.4	-	266	Primary
MAX F5	TL4	70	L + V	-	-3.4	6.6	-	-	-	295	Primary
MAX F6	TL4	95	L + V	-	-1.1	2.0	-	-	-	311	Secondary?
MAX F7	TL4	70	L + V	-	-2.9	5.5	-	-	-	320	Primary
MAX F8	TL4	95	L + V	-	-2.3	4.3	-	-	-	331	Primary
MAX F9	TL4	95	L + V	-	-4.5	9.0	-	-	-	331	Primary
MAX F1	TL4 A	95	L + V	-	-4.9	9.8	-	-	-	224	Primary
MAX F10	TL4 A	95	L + V	-	-	-	-	-	-	296	Primary

Appendix C: Fluid Inclusion Data cont'd

Ref #	Sample	Fill[1] %	Visible Contents[2] at 20°C	Tm_{CO_2} °C	Tm_{ice} °C	Salinity[3] wt.% NaCl eq. (Bodnar, 1993)	Tm_{Clath} °C	Salinity[3] wt.% NaCl eq. (Bozzo et al., 1975)	$Th_{CO_2\ L\text{-}V(L)}$ °C	$Th_{L\text{-}V(L)}$ °C	Class
MAX F11	TL4 A	95	L + V	-	-3.5	6.8	-	-	-	272	Primary
MAX F12	TL4 A	95	L + V	-	-2.2	4.1	-	-	-	245	Pseudosecondary
MAX F13	TL4 A	90	L + V	-	-	-	-	-	-	251	Primary
MAX F14	TL4 A	95	L + V	-	-3.2	6.2	-	-	-	298	Primary
MAX F15	TL4 A	75	L + V	-	-3.0	5.8	-	-	-	240	Primary
MAX F16	TL4 A	95	L + V	-	-2.3	4.3	-	-	-	284	Primary
MAX F17	TL4 A	95	L + V	-	-4.5	9.0	-	-	-	294	Primary
MAX F18	TL4 A	95	L + V	-	-5.1	10.3	-	-	-	277	Primary
MAX F19	TL4 A	95	L + V	-	-2.7	5.1	-	-	-	310	Primary
MAX F2	TL4 A	95	L + V	-	-2.2	4.1	-	-	-	228	Primary
MAX F20	TL4 A	70	L + V	-	-3.1	6.0	-	-	-	318	Primary
MAX F21	TL4 A	70	L + V	-	-2.3	4.3	-	-	-	346	Primary
MAX F22	TL4 A	75	L + V	-	-3.3	6.4	-	-	-	333	Primary
MAX F23	TL4 A	95	L + V	-	-4.8	9.6	-	-	-	268	Primary
MAX F24	TL4 A	80	L + V	-	-2.7	5.1	-	-	-	348	Primary
MAX F25	TL4 A	90	L + V	-	-4.3	8.5	-	-	-	299	Primary
MAX F26	TL4 A	95	L + V	-	-2.2	4.1	-	-	-	276	Primary
MAX F27	TL4 A	90	L + V	-	-5.5	11.2	-	-	-	284	Primary
MAX F28	TL4 A	90	CO_2 + L + V	-59.4	-	-	11.1	-	16.9	302	Primary
MAX F29	TL4 A	90	CO_2 + L + V	-56.5	-	-	8.0	4.0	17.3	301	Primary
MAX F3	TL4 A	95	L + V	-	-	-	9.1	1.8	-	268	Primary

Appendix C: Fluid Inclusion Data cont'd

Ref #	Sample	Fill[1] %	Visible Contents[2] at 20°C	Tm_{CO_2} °C	Tm_{ice} °C	Salinity[3] wt.% NaCl eq. (Bodnar, 1993)	Tm_{Clath} °C	Salinity[3] wt.% NaCl eq. (Bozzo et al., 1975)	$Th_{CO_2\ L\text{-}V(L)}$ °C	$Th_{L\text{-}V(L)}$ °C	Class
MAX F164	TL57	80	L + V	-	-	-	12.3	-	-	314	Primary
MAX F165	TL57	95	L + V	-	-3.4	6.6	-	-	-	264	Pseudosecondary
MAX F166	TL57	95	L + V	-	-4.7	9.4	-	-	-	348	Pseudosecondary
MAX F167	TL57	95	L + V	-	-3.8	7.4	-	-	-	226	Primary
MAX F168	TL57	95	L + V	-	-	-	4.3	10.1	-	314	Primary
MAX F169	TL57	90	L + V	-	-	-	-	-	-	311	Primary
MAX F170	TL57	70	L + V	-	-	-	9.1	1.8	-	284	Primary
MAX F171	TL57	50	L + V	-	-	-	8.7	2.6	-	308	Primary
MAX F172	TL57	70	CO_2 + L + V	-56.8	-	-	9.7	0.6	20.2	284	Primary
MAX F173	TL57	80	L + V	-	-	-	8.9	2.2	-	296	Primary
MAX F174	TL57	90	L + V	-	-4.2	8.3	-	-	-	284	Pseudosecondary
MAX F175	TL57	90	L + V	-	-3.4	6.6	-	-	-	303	Pseudosecondary
MAX F176	TL57	90	L + V	-	-1.7	3.2	-	-	-	308	Pseudosecondary
MAX F177	TL57	90	L + V	-	-2.9	5.5	-	-	-	308	Pseudosecondary
MAX F178	TL57	90	L + V	-	-	-	7.0	5.8	-	294	Primary
MAX F179	TL57	70	L + V	-	-	-	9.6	0.8	-	287	Primary
MAX F180	TL57	70	L + V	-	-	-	7.6	4.7	-	281	Primary
MAX F181	TL57	90	L + V	-	-	-	9.3	1.4	-	325	Primary
MAX F182	TL57	95	L + V	-	-	-	13.0	-	-	309	Primary
MAX F183	TL57	95	L + V	-	-2.4	4.5	-	-	-	299	Primary
MAX F307	TL57	90	L + V	-	-	-	8.2	3.6	-	344	Primary

Appendix C: Fluid Inclusion Data cont'd

Ref #	Sample	Fill[1] %	Visible Contents[2] at 20°C	Tm_{CO_2} °C	Tm_{ice} °C	Salinity[3] wt.% NaCl eq. (Bodnar, 1993)	Tm_{Clath} °C	Salinity[3] wt.% NaCl eq. (Bozzo et al., 1975)	$Th_{CO_2\ L\text{-}V(L)}$ °C	$Th_{L\text{-}V(L)}$ °C	Class
MAX F308	TL57	90	L + V	-	-	-	8.9	2.2	-	336	Primary
MAX F309	TL57	90	L + V	-	-	-	8.0	4.0	-	307	Primary
MAX F310	TL57	90	L + V	-	-2.5	4.7	-	-	-	321	Primary
MAX F311	TL57	90	L + V	-	-	-	8.6	2.8	-	336	Primary
MAX F312	TL57	95	L + V	-	-	-	8.9	2.2	-	331	Primary
MAX F313	TL57	90	L + V	-	-5.0	10.1	-	-	-	315	Primary
MAX F314	TL57	95	L + V	-	-2.6	4.9	-	-	-	311	Primary
MAX F315	TL57	90	L + V	-	-2.3	4.3	-	-	-	322	Primary
MAX F316	TL57	95	L + V	-	-4.7	9.4	-	-	-	331	Primary
MAX F317	TL57	95	L + V	-	-4.5	9.0	-	-	-	326	Primary
MAX F147	TL57 A	90	L + V	-	-	-	8.3	3.4	-	286	Primary
MAX F148	TL57 A	90	L + V	-	-	-	8.6	2.8	-	329	Primary
MAX F149	TL57 A	90	L + V	-	-	-	8.1	3.8	-	274	Primary
MAX F150	TL57 A	90	L + V	-	-	-	7.4	5.1	-	291	Primary
MAX F151	TL57 A	70	L + V	-	-	-	7.6	4.7	-	319	Primary
MAX F152	TL57 A	70	CO_2 + L + V	-56.8	-	-	8.5	3.0	16.8	311	Primary
MAX F153	TL57 A	80	CO_2 + L + V	-57.1	-	-	8.1	3.8	22.3	342	Primary
MAX F154	TL57 A	70	L + V	-	-	-	9.6	0.8	-	309	Primary
MAX F155	TL57 A	70	L + V	-	-	-	8.9	2.2	-	311	Primary
MAX F156	TL57 A	90	L + V	-	-	-	10.4	-	-	307	Pseudosecondary
MAX F157	TL57 A	90	L + V	-	-	-	11.0	-	-	316	Pseudosecondary

Appendix C: Fluid Inclusion Data cont'd

Ref #	Sample	Fill[1] %	Visible Contents[2] at 20°C	Tm_{CO_2} °C	Tm_{ice} °C	Salinity[3] wt.% NaCl eq. (Bodnar, 1993)	Tm_{Clath} °C	Salinity[3] wt.% NaCl eq. (Bozzo et al., 1975)	$Th_{CO_2\ L\text{-}V(L)}$ °C	$Th_{L\text{-}V(L)}$ °C	Class
MAX F158	TL57 A	90	L + V	-	-2.8	5.3	-	-	-	345	Primary
MAX F159	TL57 A	90	L + V	-	-2.6	4.9	-	-	-	294	Primary
MAX F160	TL57 A	90	L + V	-	-4.5	9.0	-	-	-	305	Primary
MAX F161	TL57 A	50	CO_2 + L + V	-56.3	-	-	8.5	3.0	26.1	318	Primary
MAX F162	TL57 A	90	L + V	-	-	-	8.4	3.2	-	278	Primary
MAX F163	TL57 A	90	L + V	-	-2.7	5.1	-	-	-	304	Primary
MAX F243	TL58	95	L + V	-	-4.2	8.3	-	-	-	299	Primary
MAX F244	TL58	95	L + V	-	-3.4	6.6	-	-	-	281	Primary
MAX F245	TL58	95	L + V	-	-4.1	8.1	-	-	-	336	Primary
MAX F246	TL58	60	L + V	-	-2.5	4.7	-	-	-	331	Primary
MAX F247	TL58	50	L + V	-	-2.1	3.9	-	-	-	341	Primary
MAX F248	TL58	95	L + V	-	-4.8	9.6	-	-	-	213	Pseudosecondary
MAX F249	TL58	70	L + V	-	-2.7	5.1	-	-	-	330	Primary
MAX F250	TL58	80	L + V	-	-5.0	10.1	-	-	-	290	Primary
MAX F251	TL58	80	L + V	-	-3.4	6.6	-	-	-	298	Primary
MAX F318	TL58	95	L + V	-	-3.1	6.0	-	-	-	237	Primary
MAX F319	TL58	70	CO_2 + L + V	-56.9	-	-	8.4	3.2	17.4	290	Primary
MAX F320	TL58	90	L + V	-	-2.3	4.3	-	-	-	313	Primary
MAX F321	TL58	90	L + V	-	-2.7	5.1	-	-	-	317	Primary
MAX F142	TL6	90	L + V	-	-3.5	6.8	-	-	-	217	Primary
MAX F143	TL6	90	L + V	-	-2.9	5.5	-	-	-	220	Primary

Appendix C: Fluid Inclusion Data cont'd

Ref #	Sample	Fill[1] %	Visible Contents[2] at 20°C	Tm_{CO_2} °C	Tm_{ice} °C	Salinity[3] wt.% NaCl eq. (Bodnar, 1993)	Tm_{Clath} °C	Salinity[3] wt.% NaCl eq. (Bozzo et al., 1975)	$Th_{CO_2\ L\text{-}V(L)}$ °C	$Th_{L\text{-}V(L)}$ °C	Class
MAX F144	TL6	90	L + V	-	-2.9	5.5	-	-	-	224	Primary
MAX F145	TL6	90	L + V	-	-2.9	5.5	-	-	-	187	Primary
MAX F146	TL6	90	L + V	-	-4.8	9.6	-	-	-	245	Primary
MAX F184	TL6	95	L + V	-	-5.7	11.7	-	-	-	166	Primary
MAX F185	TL6	50	CO_2 + L + V	-59.8	-	-	7.0	5.8	20.2	276	Primary
MAX F186	TL6	95	L + V	-	-2.2	4.1	-	-	-	277	Primary
MAX F187	TL6	90	L + V	-	-	-	8.7	2.6	-	252	Primary
MAX F188	TL6	95	L + V	-	-4.9	9.8	-	-	-	256	Primary
MAX F189	TL6	70	L + V	-	-4.0	7.9	-	-	-	261	Primary
MAX F190	TL6	70	L + V	-	-	-	9.0	2.0	-	272	Primary
MAX F191	TL6	70	CO_2 + L + V	-56.5	-	-	8.4	3.2	24.5	302	Primary
MAX F192	TL6	70	L + V	-	-	-	9.1	1.8	-	293	Pseudosecondary
MAX F193	TL6	70	L + V	-	-	-	8.6	2.8	-	302	Pseudosecondary
MAX F194	TL6	70	L + V	-	-	-	8.0	4.0	-	296	Primary
MAX F195	TL6	90	L + V	-	-2.9	5.5	-	-	-	273	Primary
MAX F196	TL6	90	L + V	-	-2.5	4.7	-	-	-	278	Primary
MAX F197	TL6	70	CO_2 + L + V	-56.3	-	-	8.4	3.2	22.3	307	Primary
MAX F198	TL6	50	CO_2 + L + V	-56.7	-	-	8.3	3.4	20.6	283	Pseudosecondary
MAX F133	TL6 A	95	L + V	-	-3.1	6.0	-	-	-	213	Primary
MAX F134	TL6 A	95	L + V	-	-2.3	4.3	-	-	-	170	Primary
MAX F135	TL6 A	95	L + V	-	-1.9	3.5	-	-	-	200	Primary

Appendix C: Fluid Inclusion Data cont'd

Ref #	Sample	Fill[1] %	Visible Contents[2] at 20°C	Tm_{CO_2} °C	Tm_{ice} °C	Salinity[3] wt.% NaCl eq. (Bodnar, 1993)	Tm_{Clath} °C	Salinity[3] wt.% NaCl eq. (Bozzo et al., 1975)	$Th_{CO_2 L\text{-}V(L)}$ °C	$Th_{L\text{-}V(L)}$ °C	Class
MAX F136	TL6 A	95	L + V	-	-1.9	3.5	-	-	-	220	Primary
MAX F137	TL6 A	95	L + V	-	-	-	8.4	3.2	-	213	Primary
MAX F138	TL6 A	95	L + V	-	-	-	8.1	3.8	-	216	Primary
MAX F139	TL6 A	70	CO_2 + L + V	-56.7	-	-	8.5	3.0	19.9	278	Primary
MAX F140	TL6 A	95	L + V		-2.8	5.3	-	-	-	214	Primary
MAX F141	TL6 A	90	L + V	-	-	-	9.3	1.4	-	214	Primary

[1] Fill % refers to the volume % of liquid relative to other phases

[2] Visible contents abrreviations: L = H_2O liquid, V = H_2O vapour, CO_2 = CO_2 liquid and/or vapour

[3] Salinity measured in weight % NaCl equivalent

Appendix D: Lithogeochemistry

Element (unit)	Method (detec. limit)	TL80	TL81	TL82	TL83	TL84	TL85	TL86	TL87	TL88	TL89	TL90	TL91	TL92	TL93	TL94	TL95	TL96	TL97	TL98	TL99
SiO_2 %	FUS-ICP (0.01)	73.41	72.59	71.38	72.42	77.17	67.35	67.34	80.93	78.4	70.84	70.07	77.14	72.84	70.2	72.26	70.17	68.63	69.42	64.55	72.94
$Al2O_3$ %	FUS-ICP (0.01)	15.91	15.74	15.17	14.49	10.86	14.82	15.02	8.92	11	13.68	15.05	11.85	14.99	14.99	14.34	17.2	15.2	14.08	18.52	13.46
Fe_2O_3(T) %	FUS-ICP (0.01)	1.22	1.43	1.21	0.84	3.23	2.62	4.9	2.44	2.46	2.29	2.71	1.01	2.03	2.81	2.84	0.97	3.26	4.09	0.89	1.65
MnO %	FUS-ICP (0.001)	0.018	0.02	0.045	0.025	0.032	0.062	0.096	0.031	0.043	0.036	0.069	0.012	0.035	0.078	0.041	0.004	0.057	0.069	0.04	0.031
MgO %	FUS-ICP (0.01)	0.39	0.41	0.29	0.15	0.58	0.57	1.65	0.42	0.54	0.49	0.67	0.3	0.51	0.55	0.58	0.05	0.63	1.02	0.26	0.34
CaO %	FUS-ICP (0.01)	2	2.23	1.24	0.71	2.22	2.95	3.91	1.99	2.39	2.45	2.83	0.55	1.49	3.04	2.85	0.19	3.28	2.87	1.57	0.85
Na_2O %	FUS-ICP (0.01)	4.17	4.16	5.21	4.83	2.7	2.98	2.76	2.45	2.77	2.78	3.45	1.56	3.33	3.77	3.46	5.52	3.76	3.12	9.31	2.11
K_2O %	FUS-ICP (0.01)	3.05	3.04	4.67	5.06	2.01	3.36	1.96	1.27	1.78	3.57	3.04	6.09	3.44	2.61	2.93	5.84	2.58	2.66	1.09	6.16
TiO_2 %	FUS-ICP (0.001)	0.199	0.22	0.103	0.074	0.271	0.296	0.568	0.233	0.286	0.251	0.353	0.102	0.288	0.302	0.267	0.043	0.334	0.443	0.463	0.162
$P2O_5$ %	FUS-ICP (0.01)	0.06	0.07	0.03	0.03	0.15	0.16	0.34	0.16	0.2	0.13	0.14	0.08	0.13	0.15	0.19	< 0.01	0.17	0.16	0.33	0.07
LOI %	FUS-ICP	0.34	0.12	0.67	0.14	1.54	4.1	1.3	1.26	0.92	3.44	2.52	1.33	1.19	0.99	0.82	0.9	0.82	0.82	1.74	2.12
Total %	FUS-ICP (0.01)	100.8	100	100	98.75	100.8	99.28	99.84	100.1	100.8	99.96	100.9	100	100.3	99.5	100.6	100.9	98.72	98.74	98.77	99.9
Au ppb	INAA (1)	< 1	< 1	< 1	< 1	4	< 1	< 1	< 1	< 1	3	3	5	6	< 1	< 1	< 1	< 1	< 1	< 1	< 1
Ag ppm	MULT INAA TD-ICP (0.5)	0.9	0.6	1.6	1.4	< 0.5	< 0.5	< 0.5	< 0.5	< 0.5	< 0.5	< 0.5	2	< 0.5	< 0.5	< 0.5	< 0.5	< 0.5	< 0.5	< 0.5	< 0.5
As ppm	INAA (1)	< 1	< 1	< 1	< 1	30	41	< 1	7	4	70	27	60	16	2	< 1	37	4	2	7	32

Appendix D: Lithogeochemistry cont'd.

Element (unit)	Method (detec. limit)	TL80	TL81	TL82	TL83	TL84	TL85	TL86	TL87	TL88	TL89	TL90	TL91	TL92	TL93	TL94	TL95	TL96	TL97	TL98	TL99
Ba ppm	FUS-ICP (1)	1726	1531	1440	2278	977	956	619	813	975	1247	1262	1175	1896	1212	1731	602	1394	1151	258	1288
Be ppm	FUS-ICP (1)	2	2	3	2	3	3	3	2	2	3	3	2	3	3	2	2	2	2	2	3
Bi ppm	FUS-MS (0.1)	< 0.1	0.2	0.2	< 0.1	0.2	0.5	< 0.1	0.9	0.2	0.5	7.5	31.1	7.9	0.7	0.1	0.2	< 0.1	< 0.1	0.1	0.5
Br ppm	INAA (0.5)	< 0.5	1	1.1	< 0.5	< 0.5	< 0.5	< 0.5	< 0.5	0.9	< 0.5	1.3	< 0.5	1.5	< 0.5	< 0.5	< 0.5	< 0.5	< 0.5	< 0.5	< 0.5
Cd ppm	TD-ICP (0.5)	< 0.5	< 0.5	< 0.5	< 0.5	< 0.5	0.6	< 0.5	< 0.5	< 0.5	0.8	< 0.5	0.5	< 0.5	< 0.5	< 0.5	< 0.5	< 0.5	< 0.5	< 0.5	< 0.5
Co ppm	INAA (0.1)	3	4.4	3.2	3.4	7.3	5.4	13	6.2	4.7	6.3	5.3	3.2	4.9	4	4	2	3	6	2	3
Cr ppm	INAA (0.5)	19	12.3	13.9	21.4	22	22.1	24.8	37.4	42.4	14.5	22.7	12.9	18.4	13.9	21	21	11	48	< 0.5	19
Cs ppm	FUS-MS (0.1)	2.8	2.7	1	0.6	5.2	8.3	7.5	2.9	4.3	7.1	9.7	7.2	7.8	7.1	6.6	4.6	5.1	8.1	4.7	7
Cu ppm	TD-ICP (1)	1	1	2	1	47	31	39	28	10	31	10	5	11	2	20	4	16	5	3	13
Ga ppm	FUS-MS (1)	20	20	20	18	18	20	21	14	17	20	20	12	19	19	17	17	18	18	15	15
Ge ppm	FUS-MS (0.5)	0.6	0.5	1.2	0.7	1.2	1.2	1.1	1.2	1.1	1.4	1.4	1.8	1.5	1.5	1.3	1.8	1.1	1.5	2.1	1.8
Hf ppm	FUS-MS (0.1)	3.2	3.1	3.5	1.3	2.7	3.1	4.3	2.5	2.7	3.3	4.4	1.9	4	4.2	3.6	3	3.2	3.9	3.9	2.8
Hg ppm	INAA (1)	< 1	< 1	< 1	< 1	< 1	< 1	< 1	< 1	< 1	< 1	< 1	< 1	< 1	< 1	< 1	< 1	< 1	< 1	< 1	< 1
In ppm	FUS-MS (0.1)	< 0.1	< 0.1	< 0.1	< 0.1	< 0.1	< 0.1	< 0.1	< 0.1	< 0.1	< 0.1	< 0.1	< 0.1	< 0.1	< 0.1	< 0.1	< 0.1	< 0.1	< 0.1	< 0.1	< 0.1
Ir ppb	INAA (1)	< 1	< 1	< 1	< 1	< 1	< 1	< 1	< 1	< 1	< 1	< 1	< 1	< 1	< 1	< 1	< 1	< 1	< 1	< 1	< 1

Appendix D: Lithogeochemistry cont'd.

Element (unit)	Method (detec. limit)	TL80	TL81	TL82	TL83	TL84	TL85	TL86	TL87	TL88	TL89	TL90	TL91	TL92	TL93	TL94	TL95	TL96	TL97	TL98	TL99
Mo ppm	FUS-MS (2)	< 2	< 2	< 2	< 2	> 100	7	> 100	> 100	> 100	> 100	17	> 100	> 100	< 2	> 100	31	43	> 100	7	> 100
Nb ppm	FUS-MS (0.2)	7.8	5.6	24.1	8.4	13.8	14.8	20	12.1	13	14.9	18.3	5.1	12.6	15.7	9	6.2	11.3	13.3	16.1	9.5
Ni ppm	TD-ICP (1)	8	3	4	2	6	2	10	2	2	3	2	4	3	4	10	3	5	10	3	9
Pb ppm	TD-ICP (5)	18	19	20	24	8	18	8	8	7	16	14	59	14	19	9	13	10	8	< 5	27
Rb ppm	FUS-MS (2)	100	101	103	96	75	122	99	46	59	140	123	192	121	102	71	156	72	87	58	186
S %	TD-ICP (0.001)	0.004	0.002	0.002	0.002	0.858	0.618	0.52	0.495	0.2	0.736	0.46	0.386	0.009	0.1	0.273	0.352	0.143	0.057	0.144	0.349
Sb ppm	INAA (0.1)	< 0.1	0.1	< 0.1	0.1	0.4	0.3	0.1	0.3	0.1	0.7	1	0.7	0.5	0.2	0.1	0.1	0.2	0.2	0.2	0.8
Sc ppm	INAA (0.01)	1.81	2.02	2.1	1.61	4.24	3.71	11.7	2.92	3.38	3.21	4.96	2.57	3.66	3.44	2.7	1.8	3.3	6	2.7	3.8
Se ppm	INAA (0.5)	< 0.5	< 0.5	< 0.5	< 0.5	< 0.5	< 0.5	< 0.5	< 0.5	< 0.5	< 0.5	< 0.5	< 0.5	< 0.5	< 0.5	< 0.5	< 0.5	< 0.5	< 0.5	< 0.5	< 0.5
Sn ppm	FUS-MS (1)	2	3	1	< 1	2	1	< 1	< 1	5	< 1	< 1	< 1	< 1	3	2	< 1	< 1	3	< 1	1
Sr ppm	FUS-ICP (2)	794	750	1897	1523	414	495	514	378	491	369	545	156	480	553	603	196	653	551	487	188
Ta ppm	FUS-MS (0.1)	0.6	0.3	1	0.5	0.6	0.7	1.1	0.8	0.8	0.9	1.1	0.7	0.8	1	0.6	1.9	0.9	0.7	1.1	1.2
Th ppm	FUS-MS (0.05)	12.1	12.2	3.01	1.89	5.23	6.09	5.48	5.6	5.15	7.53	7.6	4.54	8.59	8.02	6.94	10.3	6.67	9.35	8.04	7.69
U ppm	FUS-MS (0.05)	2.69	2.38	1.86	0.75	3.31	6.85	4.52	4.22	4.67	5.69	5.14	4.79	6.91	5.86	6.37	22.1	5.71	2.88	5.45	7.28
V ppm	FUS-ICP (5)	15	16	13	5	42	31	81	26	26	24	28	15	36	23	38	6	38	59	19	18
W ppm	INAA (1)	< 1	< 1	< 1	< 1	3	< 1	< 1	3	3	4	4	5	< 1	106	< 1	3	< 1	< 1	22	8

Appendix D: Lithogeochemistry cont'd.

Element (unit)	Method (detec. limit)	TL80	TL81	TL82	TL83	TL84	TL85	TL86	TL87	TL88	TL89	TL90	TL91	TL92	TL93	TL94	TL95	TL96	TL97	TL98	TL99
Y ppm	FUS-ICP (1)	1	2	9	< 1	12	9	22	8	8	10	11	9	10	11	10	24	12	12	16	15
Zn ppm	MULT INAA TD-ICP (1)	46	51	28	18	41	75	86	38	49	51	60	21	46	83	44	8	58	62	6	30
Zr ppm	FUS-MS (1)	116	118	116	46	97	115	160	93	99	119	166	61	141	149	139	59	126	160	151	102
La ppm	FUS-MS (0.05)	31.1	29.4	6.58	6.01	17.9	18.7	19	18.5	18.3	23.2	28.3	9.82	34.2	26.8	24.1	11.5	22.7	28.8	28.1	15.4
Ce ppm	FUS-MS (0.1)	52.2	48.7	11.6	11.3	37.1	39.5	43.3	38.9	38.8	47.4	56.2	20.5	59.5	55.1	49.5	26.2	46.3	57.8	58.3	30.8
Pr ppm	FUS-MS (0.02)	4.53	4.19	1.12	1.07	3.97	4.31	4.82	4.77	4.87	5.56	5.82	2.44	6.23	6.78	6.35	3.74	6	7.01	7.76	3.85
Nd ppm	FUS-MS (0.05)	13.3	12.3	4.31	3.81	15	16.4	20.4	16.3	17.6	19	21.9	8.85	22.5	24	20.9	15.7	20.1	22.3	27.8	13.1
Sm ppm	FUS-MS (0.01)	2.36	2.21	0.96	0.85	3.46	3.75	5.22	3.17	3.6	3.64	4.85	1.98	4.7	4.59	4.12	4.05	3.94	4.25	5.74	2.78
Eu ppm	FUS-MS (0.005)	0.638	0.596	0.272	0.22	0.814	1.15	1.34	0.88	1.05	0.985	1.34	0.593	1.39	1.34	1.18	0.502	1.2	1.13	1.19	0.722
Gd ppm	FUS-MS (0.02)	1.58	1.44	0.9	0.86	2.61	2.68	4.28	2.66	2.87	2.89	3.63	1.72	3.21	3.62	3.11	4.34	3.1	3.23	4.9	2.8
Tb ppm	FUS-MS (0.01)	0.15	0.16	0.17	0.14	0.38	0.35	0.68	0.37	0.38	0.35	0.47	0.29	0.41	0.48	0.43	0.75	0.41	0.44	0.68	0.46
Dy ppm	FUS-MS (0.02)	0.64	0.68	1.13	0.88	2.05	1.75	3.91	1.92	1.95	1.71	2.25	1.72	1.91	2.38	2.21	4.41	2.04	2.29	3.43	2.61
Ho ppm	FUS-MS (0.01)	0.11	0.11	0.26	0.19	0.38	0.32	0.74	0.36	0.34	0.31	0.39	0.33	0.33	0.4	0.39	0.81	0.35	0.41	0.6	0.51
Er ppm	FUS-MS (0.01)	0.3	0.3	0.9	0.6	1.07	0.88	2.04	0.97	0.94	0.88	1.03	0.95	0.9	1.07	1.01	2.25	0.9	1.11	1.59	1.46
Tl ppm	FUS-MS (0.05)	0.7	0.38	0.32	0.56	0.62	1.18	0.82	0.44	0.57	1.44	0.72	2.88	1.62	1.15	0.92	2.2	0.67	1.25	0.84	2.85

Appendix D: Lithogeochemistry cont'd.

Element (unit)	Method (detec. limit)	TL80	TL81	TL82	TL83	TL84	TL85	TL86	TL87	TL88	TL89	TL90	TL91	TL92	TL93	TL94	TL95	TL96	TL97	TL98	TL99
Tm ppm	FUS-MS (0.005)	0.044	0.043	0.163	0.097	0.152	0.128	0.292	0.14	0.136	0.126	0.149	0.137	0.128	0.15	0.145	0.328	0.128	0.164	0.232	0.217
Yb ppm	FUS-MS (0.01)	0.29	0.27	1.26	0.69	0.98	0.83	1.85	0.89	0.85	0.82	0.94	0.89	0.82	0.93	0.91	2.06	0.85	1.07	1.44	1.37
Lu ppm	FUS-MS (0.002)	0.041	0.043	0.216	0.121	0.153	0.124	0.275	0.14	0.121	0.124	0.146	0.124	0.129	0.143	0.134	0.294	0.127	0.159	0.204	0.201
Mass grams		1.087	1.07	1.02	1.057	0.971	0.972	1.078	1.048	1.032	0.972	1.053	1.092	0.986	0.978	1.69	1.87	1.79	1.66	1.81	1.47

Appendix E: Selected Petrographic Descriptions

Sample: TL62
Lithology: Biotite granodiorite
Primary Minerals:
Quartz (15%) Undulatory extinction, equant/blocky habit, embayed crystal margins, granoblastic
Plagioclase (40%) Oscillatory zoning, lath-shaped, pervasive sericite alteration, albite twins
Potassium Feldspar (30%) Perthitic exsolution, fresh appearance, equant grains
Biotite (5-10%) Partly replaced by chlorite, lath-shaped, shredded appearance, red–brown
Apatite (trace) Euhedral crystals, fine grained, prismatic, 1st order birefringence, chadacrysts within quartz and plagioclase
Zircon (trace) Euhedral, prismatic, 2nd order birefringence, extreme relief
Alteration Minerals:
Chlorite (trace) Associated with biotite
Epidote and Clinozoisite (1-2%) Associated with chlorite
Opaques (1-2%) Associated with biotite, secondary?
Muscovite/Sericite (mode included with plagioclase) Fine–coarse, isolated to radiating aggregates
Texture:
Equigranular. Massive. Average grain size = 0.5 mm. Plagioclase is pervasively altered. Fresh K-feldspar may be secondary. Biotite pervasively altered by muscovite + chlorite + epidote. Spatial relationship between biotite and opaques.

Sample: TL60
Lithology: Biotite granodiorite
Primary Minerals:
Quartz (27%) Anhedral, interstial, granoblastic, cuspate/lobate grain boundaries
Plagioclase (47%) Poikiolitic, oscillatory zoning, fresh and pervasively altered by sericite/muscovite, phenocrysts of unaltered zoned plagioclase
K feldspar (15%) Largely unrecognizable due to calcite-muscovite replacement
Biotite (5%) Shredded, red-brown, partly to completely replaced by chlorite
Opaques (2%) Shredded, secondary?
Zircon (trace) Euhedral, prismatic, 2nd order birefringence, included within quartz and biotite
Alteration Minerals:
Chlorite (trace) Slight green, pleochroic, anomalous blue birefringence, replaces biotite along cleavage planes
Muscovite (3%) Fine to coarse, selective replacement of feldspars (twin planes, or zones), locally radiating habit
Epidote/clinozoisite (trace) High relief, slight green-yellow pleochroism, 2nd order birefringence, locally anomalous blue-yellow birefringence...clinozoisite?, associated with partly replaced biotite
Calcite (1%) Associated with muscovite replacement, also partly replacing

plagioclase
Textures:
Porphyritic with quartz and plagioclase phenocrysts (~5%). Clusters of opaques, chlorite, biotite, epidote, and muscovite. Muscovite appears to be replacing chloritized biotite. Pervasive sericite alteration throughout. Plagioclase is also altered by calcite.

Sample: Kuskanax Batholith (TL84)
Lithology: Monzogranite
Primary Minerals:
Quartz (30%) Anhedral, cuspate/lobate margins, fresh, undulatory extinction, granoblastic
Plagioclase (45%) Albite twins, pericline twins, no alteration, euhedral
K feldspar (20%) Tartan twins, no alteration
Amphibole (2%) Pleochroic green, high relief, 60/120 cleavage, low 2nd order birefringence to upper 1st order birefringence, simple twins locally
Titanite (1%) Euhedral, prisms, extreme birefringence, extreme relief
Apatite (trace) Euhedral, high relief, included in quartz
Rutile (trace) Fine grained crystals disseminated
Opaques (trace) Fine grained disseminated
Alteration Minerals
Titanite (trace) Associated with amphibole, anhedral
Chlorite (trace) Minor, associated with amphibole
Epidote (2%) Minor, high relief, associated with amphibole
Textures
Porphyritic with 1 mm phenocrysts of K feldspar. Recrystallized quartz gives granoblastic appearance. Massive. Minor mafic component. Poikiolitic.

Sample: Galena Bay Stock (TL81)
Lithology: Biotite monzogranite
Primary Minerals:
Quartz (25%) Anhedral, cuspate/lobate grain boundaries, granoblastic
Plagioclase (40%) Albite twins, pericline twins, euhedral rectangles, minor replacement by sericite
K feldspar (30%) Tartan twins, perthitic exsolution, minor replacement by sericite, subhedral
Biotite (5%) Brown–red, subhedral, locally replaced by muscovite, minor fine grained rutile needles, define slight foliation
Muscovite (trace) Coarse grained, may be coarse sericite alteration and not primary, aligned with plagioclase twin faces
Secondary Minerals:
Sericite (trace) Associated with plagioclase and K feldspar
Epidote (trace) Isolated crystals
Textures:
Average grain size (0.5–1.0 mm). Weakly developed foliation marked by biotite,

alignment of plagioclase and recrystallized quartz. Equigranular. Feldspar intergrowths (myrmekitic).

Sample: Galena Bay Stock (TL80)
Lithology: Biotite monzogranite
Primary Minerals:
Quartz (25%) Undulatory extinction, coarse, anhedral, embayed grain boundaries, up to 3 mm
Plagioclase (45%) Albite twins, pericline twins, minor sericite alteration, oscillatory zoning, up to 4 mm, contains quartz inclusions
K feldspar (25%) Tartan twinning, locally partially replaced by sericite, up to 3 mm, anhedral, includes quartz
Biotite (5%) Red–brown, shredded, subhedral, trace chlorite alteration,
Opaques (trace) May be secondary, seems to be associated with biotite, titanite growing on margins
Secondary Minerals:
Titanite (trace) Anhedral, high relief, extreme birefringence, associated with biotite
Muscovite (trace) Partial replacement of biotite, coarse grained, shredded
Chlorite (trace) Partial replacement of biotite
Epidote (trace) Partial replacement of biotite
Textures
Massive. Slightly porphyritic with 4 mm wide plagioclase phenocrysts. Very little mafic component. Minor selective sericite alteration. Sericite alteration appears most abundant along twin planes. Partial replacement of biotite by muscovite + chlorite + epidote + titanite. Quartz is clearly recrystallized. Poikiolitic.

Sample: Kuskanax Batholith (TL83)
Lithology: Amphibole monzogranite
Primary Minerals:
Quartz (20%) Anhedral, embayed margins, undulatory extinction
Plagioclase (45%) Albite twinning, pericline twinning, euhedral–subhedral, slightly altered by sericite, contains quartz inclusions
K feldspar (29%) Tartan twinning, minor sericite alteration, contains quartz inclusions
Amphibole (5%) Green, pleochroic, altered by clays/epidote/titanite, poikiolitic with quartz? chadacrysts, high relief, lower 2nd order birefringence/upper 1st order birefringence,
Titanite (1%) Euhedral, prisms, high relief, isolated and associated with amphibole, looks primary locally
Secondary Minerals:
Calcite (trace) Associated with amphibole, and hairline veins
Epidote (trace) Associated with amphibole margins
Sericite (trace) Associated with plagioclase and K-feldspar, minor and selective
Texture:

Equigranular. All <1 mm. Massive. Minor sericite alteration of feldspars. Amphiboles look unhappy pervasively and strongly altered by clay? calcite, epidote, titanite? Hairline calcite veins throughout.

Sample: TL55
Lithology: Biotite hornfels
Minerals:
Biotite (40%) Pleochroic, light brown, randomly oriented
Quartz (30%) Anhedral, granoblastic, annealed
Plagioclase (20%) Albite twins, partly replaced by sericite, poikioblastic
K feldspar (10%) Perthitic exsolution, partially replaced by sericite, poikioblastic,
Opaques (10%) Shredded
Sericite (trace) Fine to coarse grained, isolated and radiating aggregates
Rutile (trace) Associated with opaques
Textures:
Massive. All <1 mm. Most 0.1-0.3 mm. Extremely altered. Mottled appearance. Granoblastic quartz. Extremely poikioblastic (quartz inclusions). Rare epidote and sericite alteration. Red–brown biotite is distinct. Biotite aggregates locally.

Sample: TL41 (100m into adit)
Lithology: Muscovite chlorite phyllite
Minerals:
Quartz (30%) Present in distinct layers and randomly distributed "clasts"
Muscovite (40%) Aggregate into layers, strong foliation, fine grained
Chlorite (15%) Throughout. especially associated with muscovite rich layers, slightly green pleochroic, often more coarse than muscovite, up to 1 mm
Opaques (10%) Throughout, lens habit
Calcite (5%) Throughout
Textures:
Compositional banding with quartz and mica segregations. Distinct foliation. Coarse (2 mm) quartz "clasts" that are randomly distributed and have mica segregations wrapping them. "Clasts" have been recrystallized and possess a granoblastic texture. Quartz-mica segregations are of variable thickness.

Sample: TL17
Lithology: Biotite granodiorite
Primary Minerals:
Quartz (20%) Phenocrysts (0.5 mm), cuspate/lobate margins, anhedral, virtually the only recognizable mineral in this slide
Plagioclase (50%; sericite alteration ignored for mode) Extremely altered by fine-coarse grained muscovite, locally completely replaced, localized albite twins and pericline twins still visible, locally oscillatory zoning present
K feldspar (15%) Extremely altered by fine-coarse grained muscovite, perthitic exsolution locally preserved, mostly completely replaced, difficult to recognize.
Biotite (5%) Partially to completely replaced by muscovite and chlorite, may be

hydrothermal biotite...difficult to determine.
Opaques (2%) Pyrite (square habit) and shredded associated with biotite breakdown
Secondary Minerals:
Muscovite/sericite (ignored in modal but extremely abundant) Ranges from fine-coarse grained, replacing feldspar and biotite
Chlorite (2%) Partially to completely replacing biotite
Calcite (2%) Throughout, associated with feldspar breakdown and randomly distributed throughout the matrix, anhedral
Texture:
Porphyritic with quartz phenocrysts up to 5 mm. Extreme and pervasive sericite/muscovite alteration. Virtually no feldspar remains fresh. Biotite has also undergone partial to complete replacement. Matrix grain size <1 mm–2 mm. Massive.

Sample: TL70
Lithology: Aplite
Minerals:
Quartz (20%) Anhedral, space filling, blocky
Plagioclase (10%)Locally altered by sericite alteration, subhedral, albite twins, pericline twins
K feldspar (70%) Locally altered by sericite, perthitic exsolution and microcline twins, anhedral low relief
Muscovite (1%) Coarse grained, some associated with biotite, others are isolated and look primary, some muscovite is intergrown with micrographic texture
Garnet (trace) Most are euhedral with octahedral shapes and some are anhedral and poikiolitic, high relief, pink in ppl, isotropic
Biotite (trace) Red–brown, spindle habit, <1 mm, partially to completely replaced by chlorite, looks secondary as it is present along fractures and twin planes
Chlorite (trace) Partially to completely replacing biotite, spindle like habit
Epidote (trace) Anomalous blue–yellow interference clinozoisite?, high relief, associated with replaced biotite
Textures:
Spectacular micrographic/graphic texture! it is everywhere and makes modal estimates difficult. Equigranular. 2 mm to <1 mm.

Sample: TL71
Lithology: Marble (960L)
Minerals:
Calcite (90%) Granoblastic, blocky habit
Quartz (10%) Cuspate/lobate, anhedral
Muscovite (trace) Fine grained, rare, euhedral blades
Textures:
Granoblastic. Slightly foliated. Almost mono-mineralic. 1 mm to <1 mm (average 0.1 mm). Equigranular.

Sample: TL92
Lithology: Biotite granodiorite
Primary Minerals:
Quartz (20%) Phenocrysts up to 5 mm, cuspate/lobate margins, granoblastic, undulatory extinction
Plagioclase (58%) Completely replaced by fine grained sericite alteration, albite and pericline twins are locally preserved, oscillatory zoning locally preserved
K feldspar (15%) Minor, completely replaced by sericite alteration, tartan twins locally preserved.
Biotite (5%) Partially to completely replaced by muscovite and chlorite
Apatite (trace) High relief, prismatic, included in quartz and biotite
Zircon (trace) High relief, prismatic, euhedral, included in biotite
Secondary Minerals:
Chlorite (trace) Partially to completely replaces biotite
Muscovite/sericite (included in plagioclase mode) Fine to coarse, replaces feldspars and biotite, coarse muscovite flakes disseminated throughout, pseudomorphs?
Titanite (trace) Fine grained, high relief, extreme birefringence, anhedral, associated with biotite replacement
Opaques (2%) Irregular masses associated with biotite replacement
Textures:
Porphyritic with quartz phenocrysts up to 5 mm. Pervasive alteration. Average grain size 1 mm. Granoblastic. Poikiolitic.

Sample: TL75
Lithology: Biotite granodiorite
Primary Minerals:
Quartz (20%) Phenocrysts up to 3 mm, blocky to anhedral, cuspate/lobate, granoblastic
Plagioclase (60%) Albite twins, pericline twins, oscillatory zoning, weak-strong pervasive sericite alteration, columnar habit, euhedral-subhedral, quartz inclusions
K feldspar (10%) Partially to completely replaced by sericite, tartan twinning preserved locally
Biotite (5%) Partially to completely replaced by coarse muscovite and chlorite, alteration occurs along cleavage planes, rare titanite and epidote are also associated with alteration, red–brown color, biotite may itself be secondary, pleochroic
Opaques (2%) Sieved, shredded
Zircon (trace) Fine grained, high relief, 2nd order birefringence, euhedral, prismatic, present as inclusions
Apatite (trace) High relief, 1st order birefringence, euhedral, prismatic, present as inclusions
Secondary Minerals:
Chlorite (trace) Partially to completely replacing biotite, anomalous blue

interference and weak green pleochroism
Epidote (trace) Epidote locally has anomalous blue-yellow birefringence... clinozoisite? altering biotite and present within plagioclase
Titanite (trace) Anhedral, always associated with biotite alteration, high relief, extreme birefringence
Muscovite/sericite (3%) Coarse replacement of biotite, fine replacement of feldspars
Calcite (trace) Present throughout, altering biotite and plagioclase
Texture:
Porphyritic with quartz phenocrysts. Massive. Epidote-chlorite-muscovite-titanite pseudomorphs of biotite. Weak pervasive sericite alteration.

Sample: TL74
Lithology: Biotite granodiorite
Primary Minerals:
Quartz (15%) Anhedral, phenocrysts, blocky, embayed margins, undulatory extinction
Plagioclase (40%) Subhedral-euhedral, albite twins, pericline twins, partially to completely replaced by sericite, quartz inclusions, oscillatory zoning, plagioclase phenocrysts up to 4 mm
K feldspar (25%) Weak selective sericite alteration, unaltered k feldspar present, tartan twins, perthitic exsolution, blocky, anhedral, poikiolitic
Biotite (5-10%) Red-brown euhedral blades, partially-completely altered by chlorite + muscovite + epidote + calcite
Opaques (trace) Irregular masses often associated with biotite
Zircon (trace) Fine grained prisms included in quartz
Secondary Minerals:
Chlorite (trace) Subtle green pleochroism, anomalous blue birefringence, altering biotite along cleavage faces, includes rutile needles that may have belonged to biotite
Muscovite/sericite (trace) Fine to coarse grained, selective replacement of plagioclase
Epidote (trace) High relief, slight yellow-green pleochroism, associated with chlorite and biotite replacement, locally yellow-blue birefringence indicates presence of clinozoisite?
Calcite (trace) Extreme birefringence, twins, variable relief, associated with plagioclase alteration
Titanite (trace) Extreme relief, extreme birefringence, anhedral
Textures:
Porphyritic with quartz phenocrysts (5 mm). Massive. Moderate and pervasive sericite alteration. Partial to complete replacement of biotite. Granoblastic. Average grain size 0.5-1.0 mm.

Sample: 07-187
Lithology: Garnet clinopyroxene skarn

Minerals:
Garnet (30%) Massive to euhedral, isotropic, pink in plane polarized light
Calcite (10%) Interstitial, anhedral
Quartz (10%) Giant blocky quartz crystals (optically continuous) up to 1.0 cm. Poikiolitic with clinopyroxene chadacrysts
Clinopyroxene (40%) Blocky, equant, high relief, second order birefringence, 2 cleavages at 90 with one more developed, granoblastic, clinopyroxene pseudomorphs of plagioclase (albite twins?)?
Amphibole (trace) 60/120 cleavage, green-brown pleochroic, second order birefringence, altered brown at margins, partly replaced
Rutile (trace) Deep red-brown in plane polarized light, isotropic
Epidote (trace) 2nd order birefringence, high relief, anhedral, some have blue-yellow birefringence...clinozoisite?
Unknown (trace) Green blades, pleochroic, upper 1st to 2nd order birefringence, radiating, occur in clumps
Texture:
Massive. Granoblastic. Mineralogy is very difficult to ID because of partial replacement, and the “dusty” appearance of the slide.

Sample: 06-185.34
Lithology: Garnet clinopyroxene skarn
Minerals:
Clinopyroxene (33%) Blocky, 2 cleavages at 90, high relief, slight pleochroism
Calcite (10%) Interstial, variable relief, granoblastic
Quartz (15%) Anhedral, granoblastic, annealed, cuspate/lobate grain boundaries, fresh
Titanite (trace) High relief, extreme birefringence, mantled by opaque.
Muscovite (40%) Radiating habit, fine to coarse, upper 1st order to 2nd order birefringence, massive
Opaques (2%) Shredded, irregular habit
Amphibole (actinolite?) (trace) 2 cleavages at 60 and 120, slight green pleochroism, euhedral, becoming replaced by clinopryoxene
Texture:
Massive. Granoblastic. Variable grains size.